



Australian Government



AUSTRALIAN INSTITUTE
OF MARINE SCIENCE

TOWNSVILLE

DARWIN

PERTH

Darwin Harbour Sediment Sampling Design

Murray Logan

October 25, 2019

Table of contents

1 Synopsis	1
2 Data processing	2
2.1 GIS data	2
2.2 Munksgaard 2012 chemical sediment data	3
2.3 Offset Outer Harbour sediment monitoring data	4
2.4 Designated sampling sites	4
2.5 Hydrodynamic and wave modelling	5
2.5.1 Masks	8
2.6 Outer Harbour sampling domain	14
2.7 Exclusion zone masks	19
3 Spatial Model fitting	22
4 Sampling	25
4.1 East Arm	27
4.2 Outer Harbour	34
5 Conclusions	41
6 Appendix A	42
7 Appendix B	60
References	74

1. Synopsis

The purpose of this work was to inform the spatial component of the Darwin Harbour Sediment Monitoring sampling design. In particular, to determine the 'best' location for 100 sediment monitoring sites in the East Arm and Outer Harbour sections of Darwin Harbour.

To help inform this process, there were three broad sources of data available:

1. Hydrodynamic modelling of the entire Darwin Harbour. These data (availed via geoTiffs), comprise broadly tidal bed shear and velocity as well as wave driven forces at 10m resolution and will be used to isolate areas likely to experience deposition (rather than erosion) of sediments.
2. Munksgaard sediment chemical survey from 2012 provided by Lynda Radke (as an Excel workbook). These data provided background information that was used to predict the full spatial distribution of a range of sediment chemicals. These spatial distributions then helped tune and evaluate a range of sampling designs.
3. Offset shallow Outer Harbour sediment survey provided by Lynda Radke (as an Excel workbook). Similar to the Munksgaard, data these data provided background information for the Outer Harbour.

The basic procedure involved the following steps:

1. Read in a process the data sources.

Townsville address: PMB No 3,
Townsville MC, Qld 4810
Tel: (07) 4753 4444
Fax: (07) 4772 5852

Darwin address: PO Box No 41775,
Casuarina NT 0811
Tel: (08) 8920 9240
Fax: (08) 8920 9222
www.aims.gov.au

Perth address: The UWA Oceans Institute (M096)
35 Stirling Highway, Crawley WA 6009
Tel: (08) 6369 4000
Fax: (08) 6488 4585

2. Fit a barrier spatial model to each of the Munksgaard sediment chemicals and predict/develop spatial layers for the East Arm section.
3. Fit a barrier spatial model to each of the Offset shallow Outer Harbour sediment chemicals and predict/develop spatial layers for the Outer Harbour.
4. Develop masks out of the hydrodynamic model data and use them to exclude areas of likely erosion from the chemical spatial layers.
5. Use spatial layers representing shipping channels, ports and other exclusion zones to establish additional masks to apply alongside hydrodynamic modelling masks to further restrict the sampling domains and prevent sampling configurations containing sites in the exclusion zones.
6. Explore three different sample generation routines for a range of sample sizes to establish an optimal sampling design. The five routines will be:
 - a) Using the masked chemical spatial layers to inform Conditioned Latent Hypercube Sampling - this will generate samples of nominated sizes that are located in a manner that most represents the underlying patterns in the chemical spatial layers.
 - b) Completely random sampling - this will select the nominated number of samples from within the masked area and is completely naive to any underlying spatial patterns (and hence is only likely to be representative of the underlying patterns when the number of samples is large).
 - c) A regular sampling grid - this will select approximately the nominated number of samples configured in a regular grid within the masked area. Like the completely random sampling, the regular sampling grid is completely naive to the underlying spatial patterns, yet it does guarantee a more even spatial coverage.
 - d) A spatially balanced design - this will yield a spatially balanced design in which sampling sites are spread out throughout the spatial domain.
 - e) A high dimensional spatially balanced design - this will yield a design in which sampling sites are spread in multiple dimensions (spatial and according to patterns in the underlying chemical distributions).

In addition to the 100 long-term monitoring sites, there are 20 designated sites. These sites are to be sampled more regularly and are for the purpose of compliance monitoring specific areas. Although these sites are additional to the long-term samples, they do form part of the overall design and thus need to be considered when considering candidate configurations.

All code for this project is available on github <https://github.com/AIMS/darwin-harbour-sampling.git>

2. Data processing

2.1. GIS data

A shapefile of Darwin Harbour (see Figure 1) was utilized in order to define the initial sampling domain(s). This project focused on the Outer Harbour and East Arm. For the purpose of the sediment monitoring program, East Arm was defined as East Arm, Elizabeth River and a section of the Middle Harbour adjacent the city of Darwin. The Outer Harbour was defined as Outer Harbour and Shoal Bay.

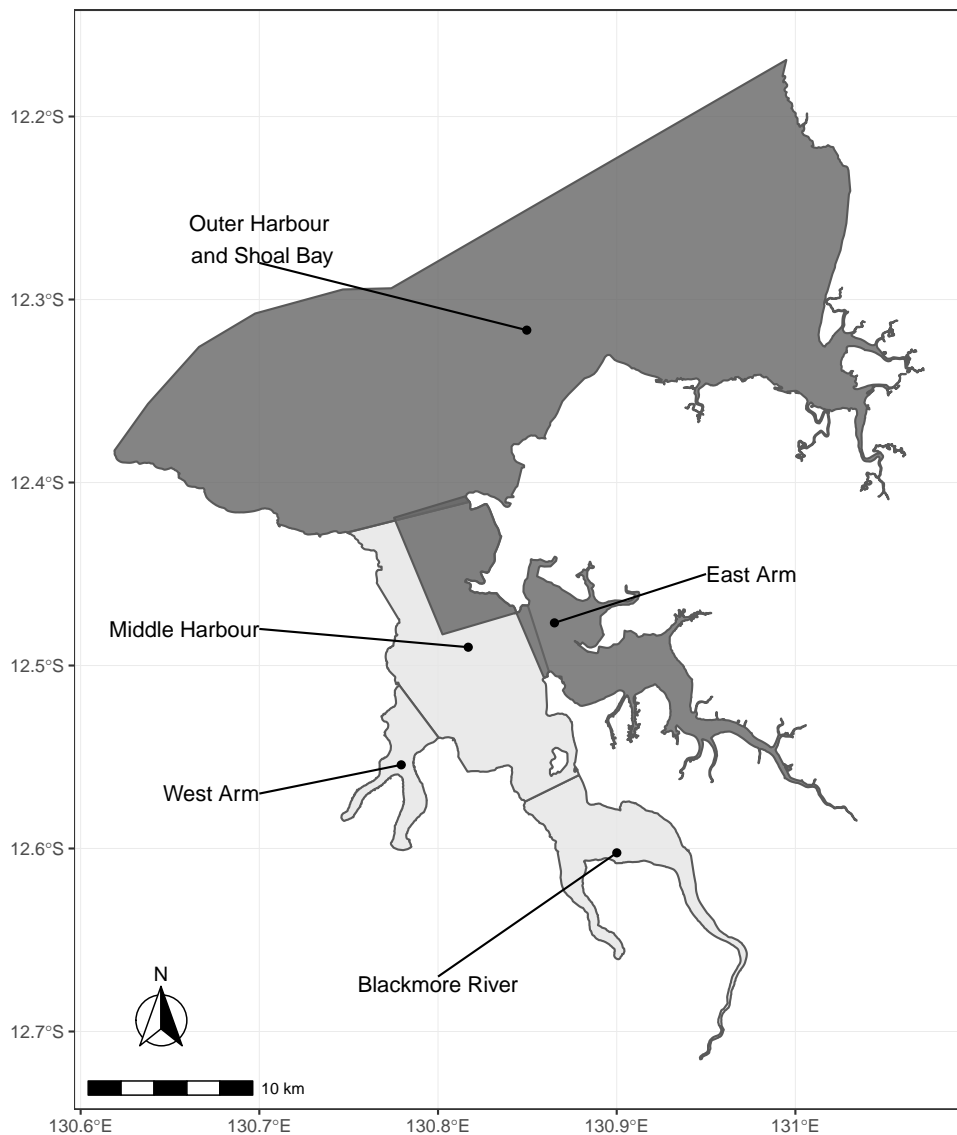


Figure 1: Map of Darwin Harbour highlighting the Outer Harbour and East Arm sections.

2.2. Munksgaard 2012 chemical sediment data

Munksgaard 2012 chemical sediment data were provided by Lynda Radke in the form of an Excel workbook. These data were consolidated together into a single flat csv text file to support analyses. The spatial configuration of the Munksgaard sediment sampling sites are illustrated in Figure 2 (circular points). Primarily only the sites within the Outer Harbour and East Arm will be used to inform the current exploration of future sampling designs.

Note: while the coverage of East Arm sites was extensive, the Outer Harbour sites were clustered together in the south east corner of the Outer Harbour (see Figure 2). The use of these Munksgaard 2012 Outer Harbour sediment data to estimate the underlying patterns throughout the entire Outer Harbour was not appropriate. Any modelling patterns are only reliable within the spatial bounds of the available data. Any attempts to extrapolate to a broader area (e.g. the rest of the Outer Harbour), is not appropriate. Consequently, and unfortunately, the Munksgaard sediment data were of little utility for designing a sampling program for the Outer Harbour.

2.3. Offset Outer Harbour sediment monitoring data

Offset Outer Harbour sediment monitoring data were provided by Lynda Radke in the form of an Excel workbook. These data were consolidated together into a single flat csv text file to support analyses. The spatial configuration of the Offset Outer Harbour sediment sampling sites are illustrated in Figure 2 (square points). These data were used to inform the selection of Outer Harbour sites.

2.4. Designated sampling sites

In addition to the long-term monitoring sites, a number of more regularly sampled designated sites were provided by Lynda Radke in the form of an Excel workbook. These sites formed additional sites, yet they needed to be considered in the formulation on site configurations and are illustrated in Figure 2 as red points. Note: none of the designated sites fall in the defined Outer Harbour and East Arms regions and thus they were not considered further.

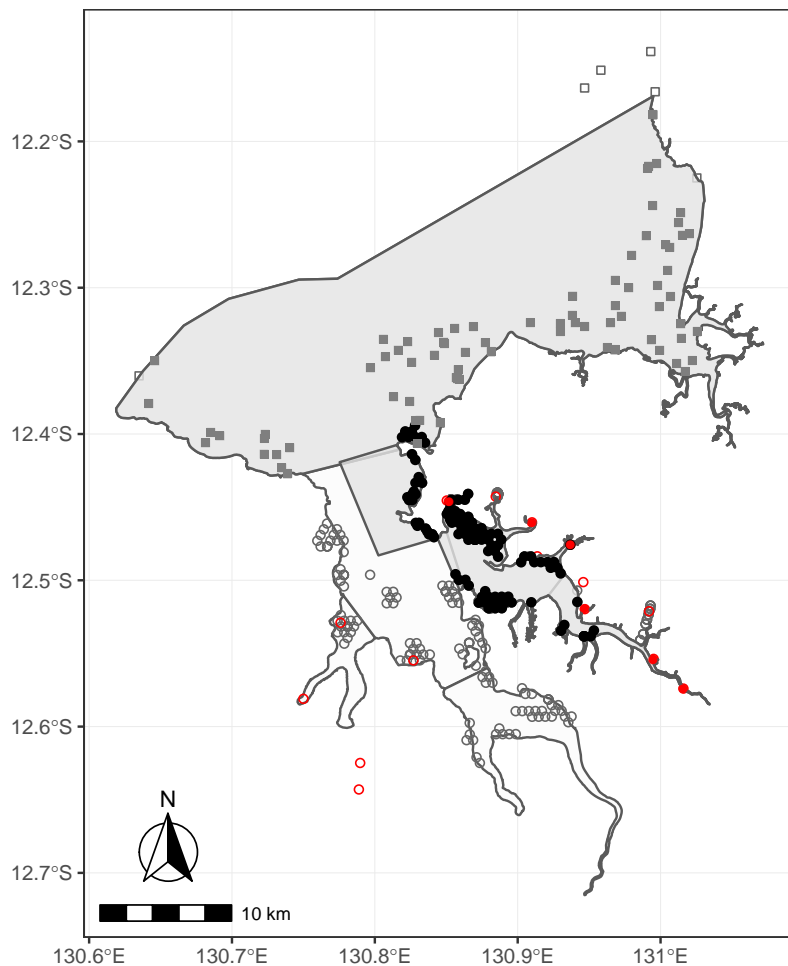


Figure 2: Map of Darwin Harbour indicating the spatial configuration of Munksgaard 2012 sediment monitoring sites (dots). Solid dots signify sites within the Outer Harbour and East Arm focal areas. Black circular points represent Munksgaard 2012 sediment sampling sites, square points represent Offset Outer Harbour sediment sites and red points represent designated sites.

2.5. Hydrodynamic and wave modelling

When designing a sediment monitoring program, it is important to consider the erosive, transportation and deposition forces operating on the seabed. Ideally all, if not most, of the sampling sites should be located in areas that are more likely to experience sediment deposition than erosion or transportation.

Various hydrodynamic and wave modelling products were made available by Dr. Richard Brinkman (AIMS) that provide estimates of erosive, transportation and deposition likelihoods and include:

- current velocity (50th and 75 percentiles - these were calculated from a 30 day characteristic spring-neap tidal cycle. Higher velocity equates to higher likelihood of sediment transport and erosion and thus lower probability of sediment deposition).
- seabed shear stress (50th and 75 percentiles - these were derived from the current velocity and are a measure of the shear forces likely to be experienced on the sea bed due to tidal movement. Higher bed shear stress equates to higher likelihood of sediment transport and erosion and thus lower probability of sediment deposition).
- wave derived orbital velocity magnitude at seabed - a shallow water wave model was applied using a 10 m/s wind forcing from a range of directions (0, 90, 140, 270 and 315 degrees) to simulate the likely orbital velocity experienced by the seabed. Higher orbital velocity equates to a higher likelihood of sediment transport and erosion and thus lower probability of sediment deposition.
- wave derived seabed shear stress - the same shallow water wave model was expressed in terms of wave bed shear stress. Higher shear stress equates to higher likelihood of sediment transport and erosion and thus lower probability of sediment deposition.

Visual representations of each of the above products within the Outer Harbour and East Arm focal areas are depicted in Figures 3 – 6.

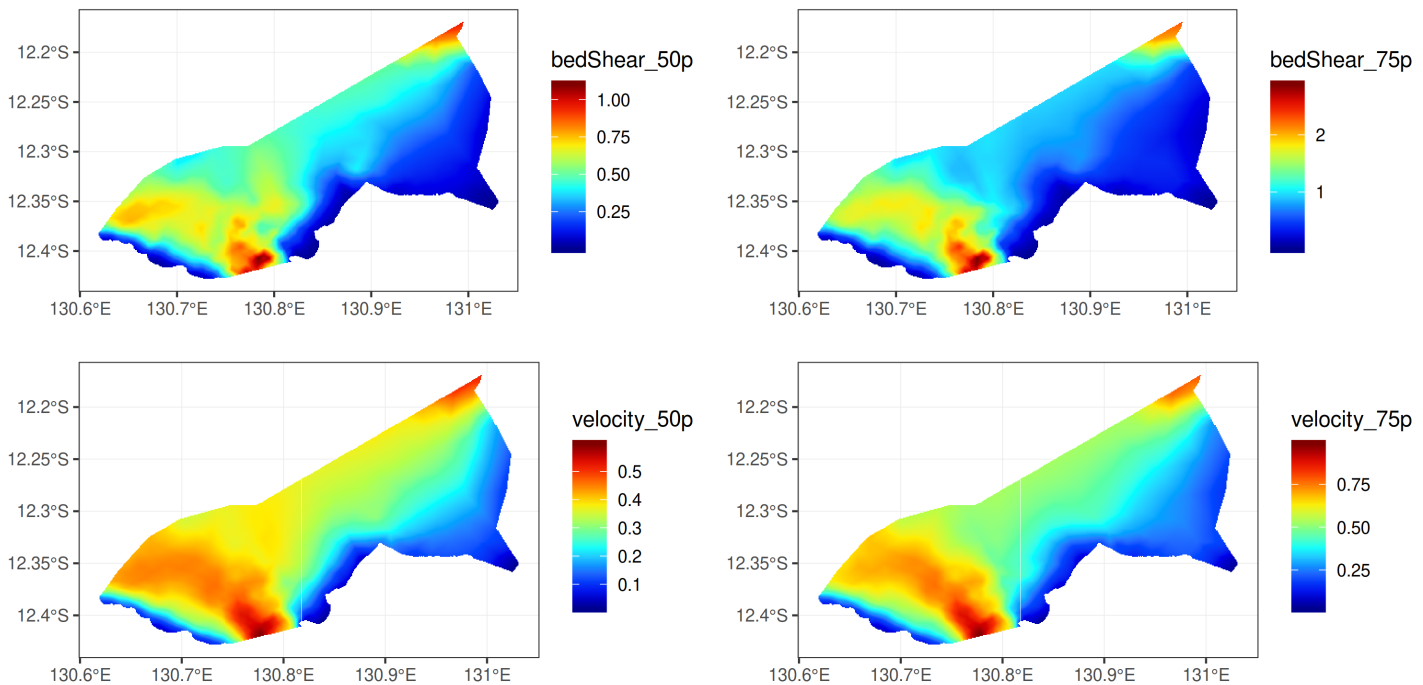


Figure 3: Outer Harbour extract of four hydrodynamic modeling tidal products.

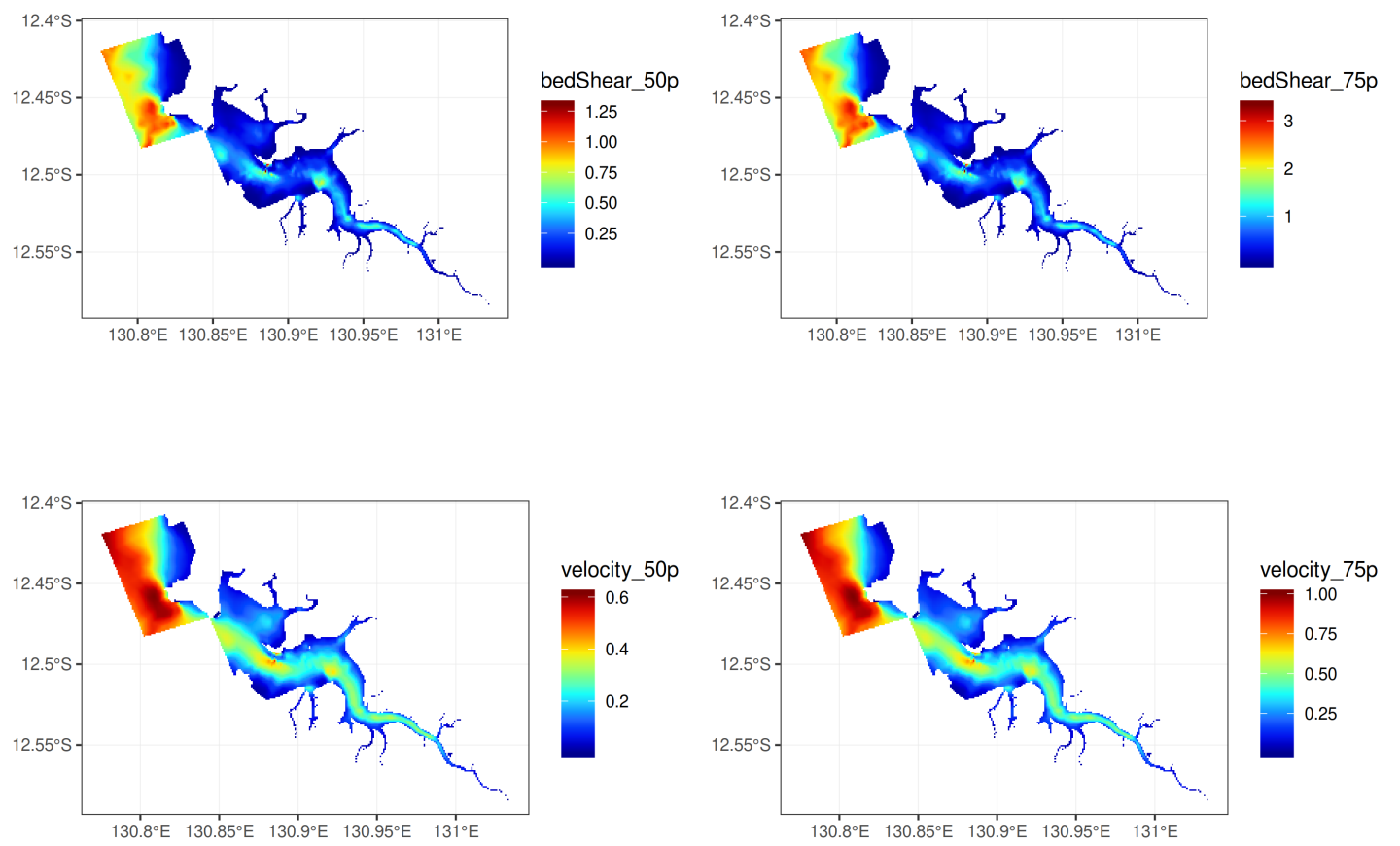


Figure 4: *East Arm extract of four hydrodynamic modeling tidal products.*

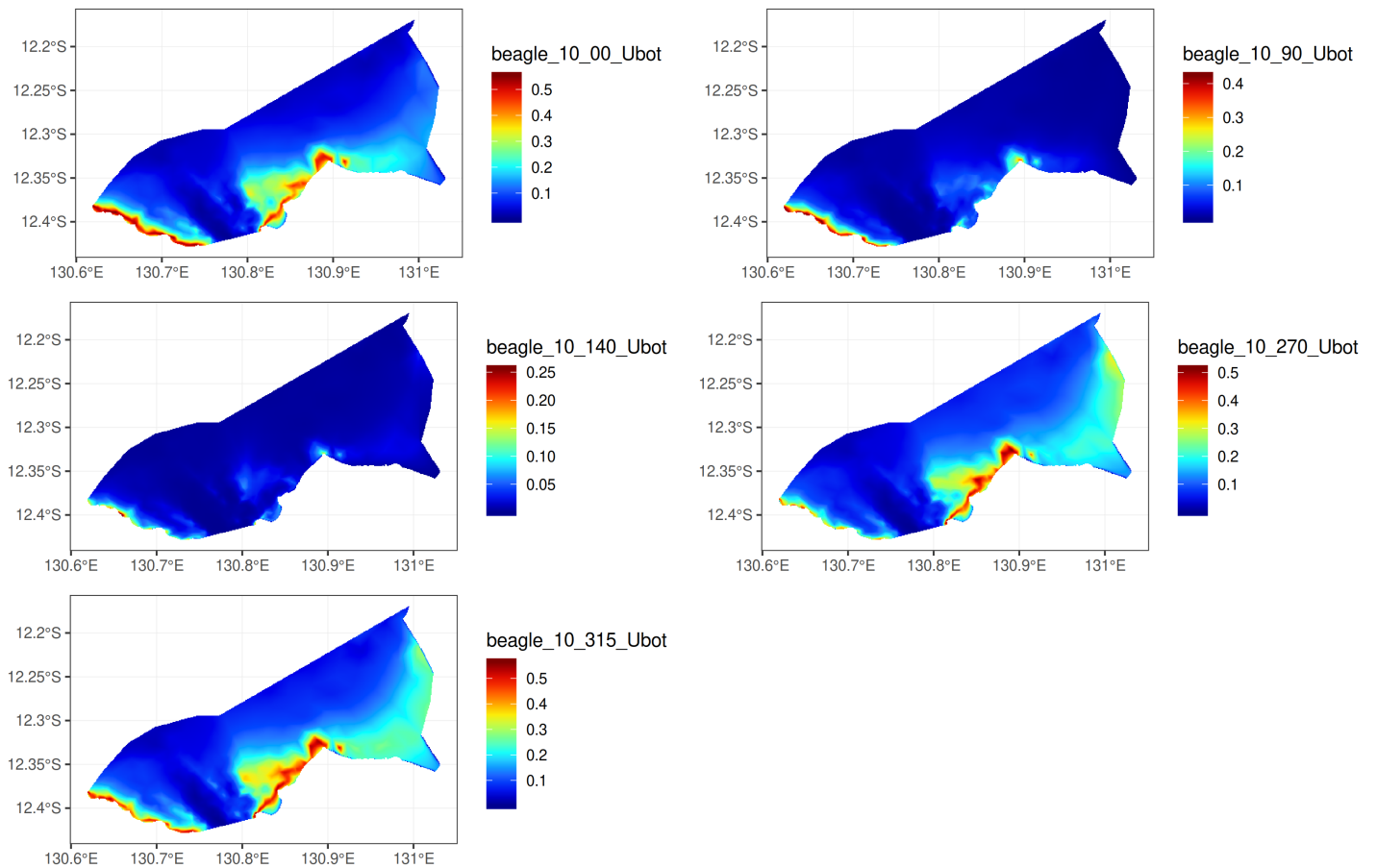


Figure 5: Outer Harbour extract of five hydrodynamic modeling wave products. The different products represent different wind angles (0, 90, 140, 270 and 315 degrees).

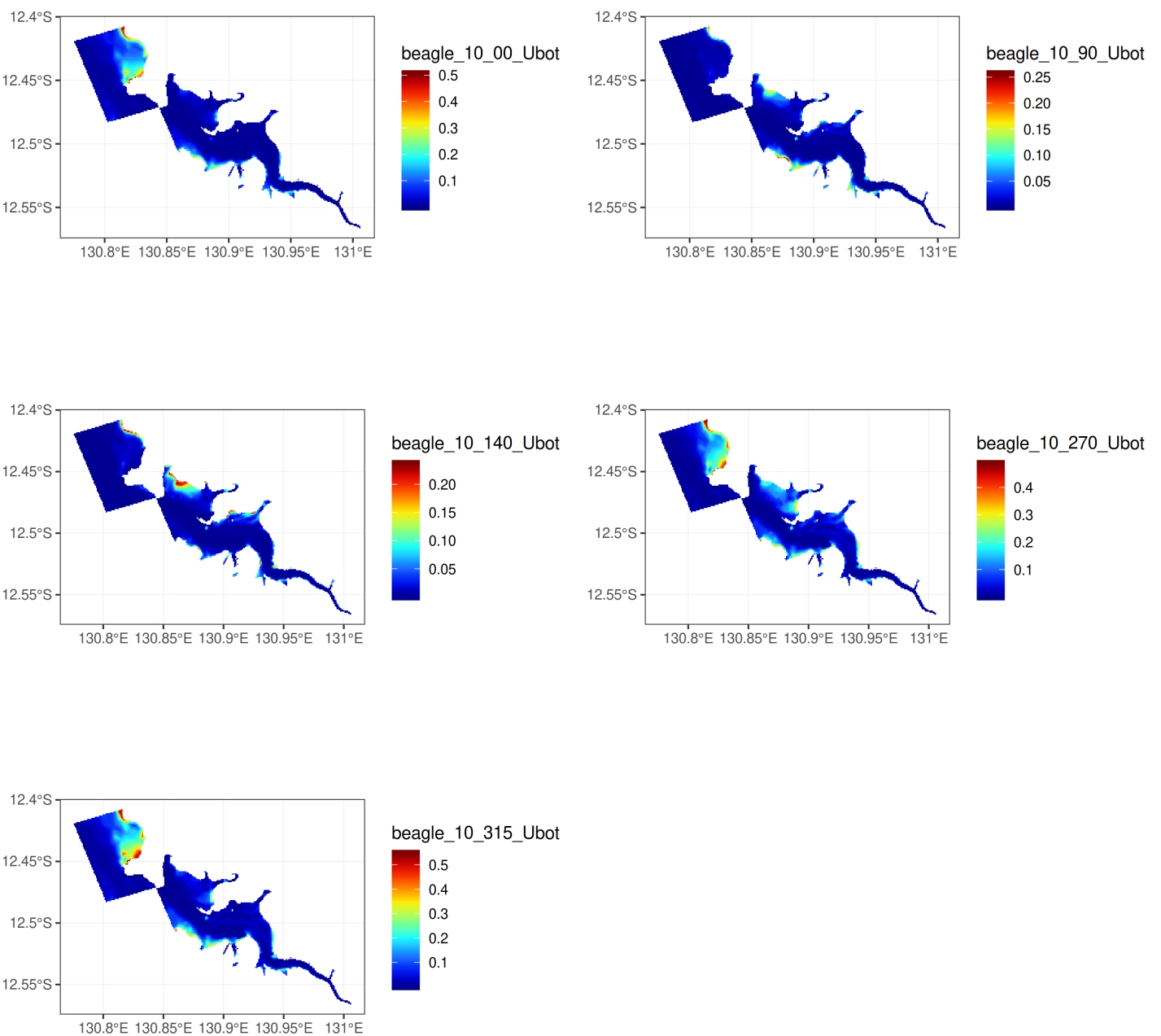


Figure 6: *East Arm extract of five hydrodynamic modeling wave products. The different products represent different wind angles (0, 90, 140, 270 and 315 degrees).*

2.5.1. Masks

The seabed shear stress products provided spatial modelling of the expected forces acting on the sea bed during a typical spring-neap tidal cycle. In so doing, they provided proxies for the likelihood for sediment erosion, transportation and deposition. These products were used to create masks that exclude areas of high erosive or transportation potential.

To establish a mask (to focus only on deposition areas), thresholds need to be established for what represent the critical values below which deposition is likely. Figures 7 and 8 provide these for a range of sediment particle sizes for water velocity and sea bed stress respectively.

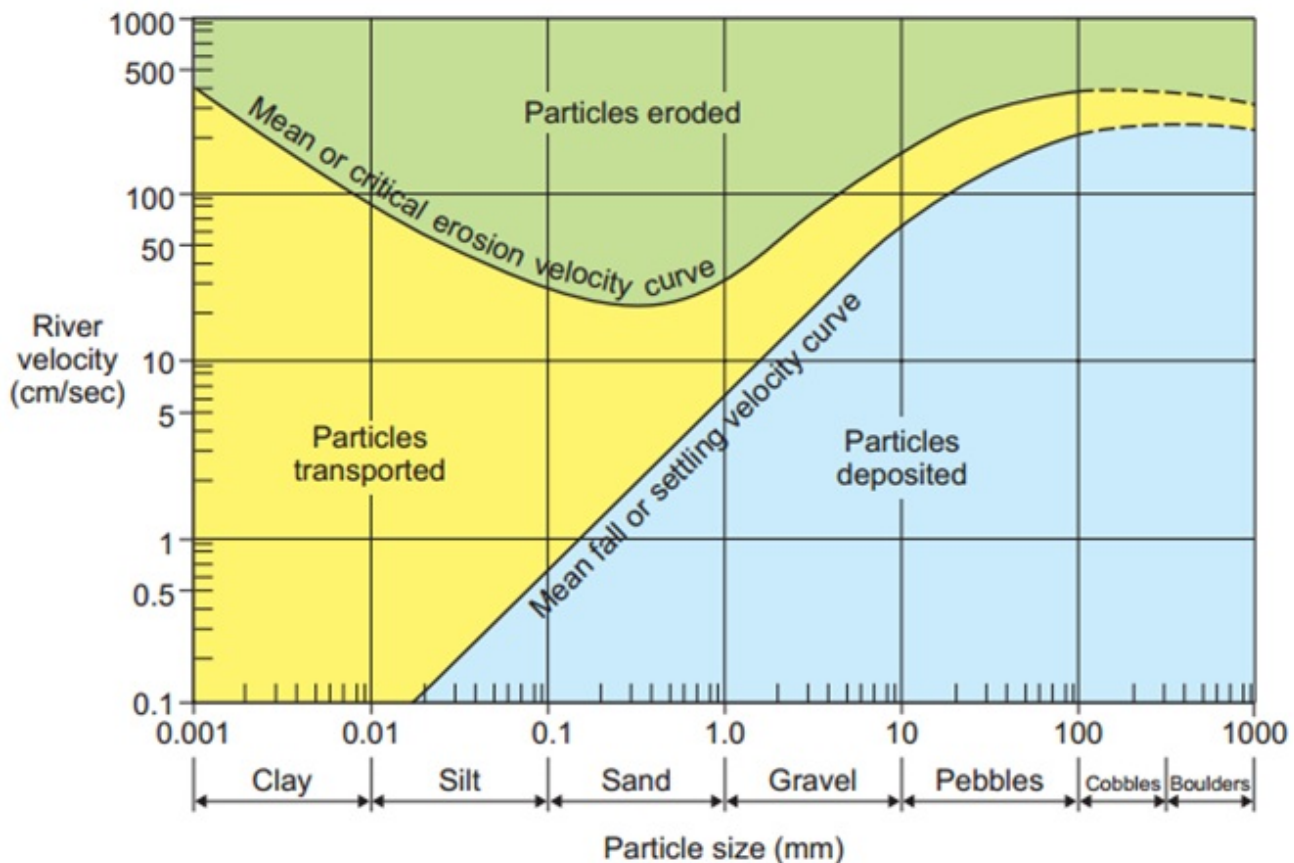


Figure 7: *Hjulstrom Curve linking sediment size and the velocity needed to erode, transport or deposit* (from <https://www.thegeoroom.co.zw/hydrology/hjulstrom-curve.php>).

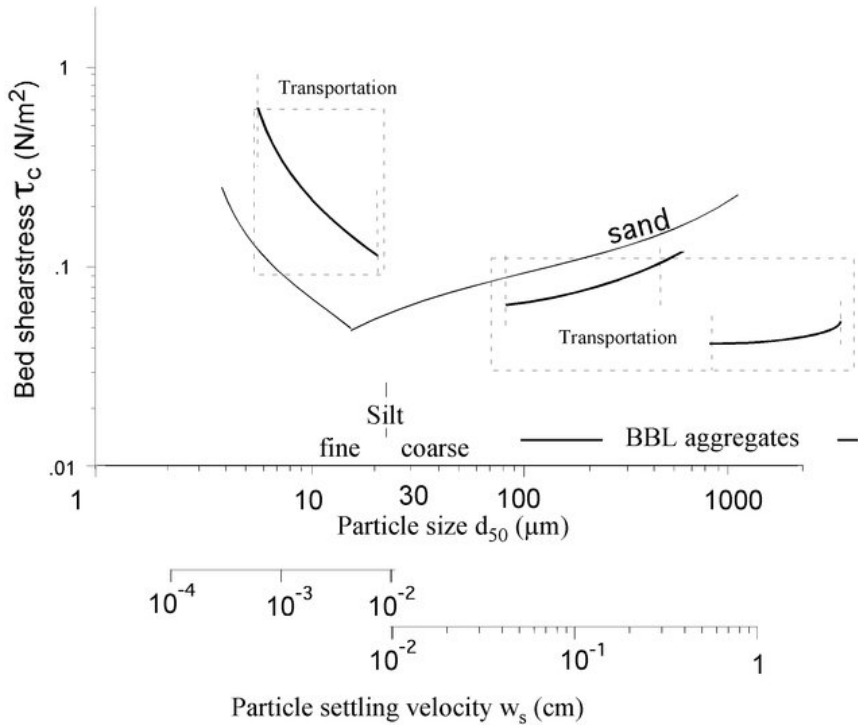


Figure 8: *Critical bed shear stress for erosion and particle settling velocity of a range of particle sizes from Thomsen (2002)*

East Arm sampling domain

Figure 9 illustrates the distribution of percentage abundance of a range of particle sizes class categories from the Munksgaard sampling program. On average, particles in the size classes 4-62 μm (Silt) and 62-250 μm (fine sand) made up 25.4 and 43.4 percent of the sediment samples respectively. Hence, it was important that future East Arm sampling designs focus on sites that will ensure deposition of particles of these sizes. According to Figures 7 and 8, particles at or above 29 μm (middle of the silt range) correspond to critical deposition values of approximately 0.2 m/s velocity and 0.1 seabed shear stress.

The hydrodynamic modeling seabed shear stress products represent the 50th and 75th percentile values. In the case of the 50th percentile, this means that 50 percent of the time, seabed shear stress was estimated to be above this value and 50 percent of values were below. If a mask was based on setting the threshold to correspond to the 50th percentile, then the masked layer represents areas where sediment deposition is likely to occur more regularly than erosion and transport.

Nevertheless, it was important to also establish the distribution of seabed shear stress across the seabed in order to better understand the distribution of values. Figures 10 and 11 illustrate the frequency of seabed shear stresses (and velocity) for the East Arm area. The 50th percentiles for seabed shear stress appear to drop off the peak at around 0.2 m/s, hence this appears to be a sensible threshold value.

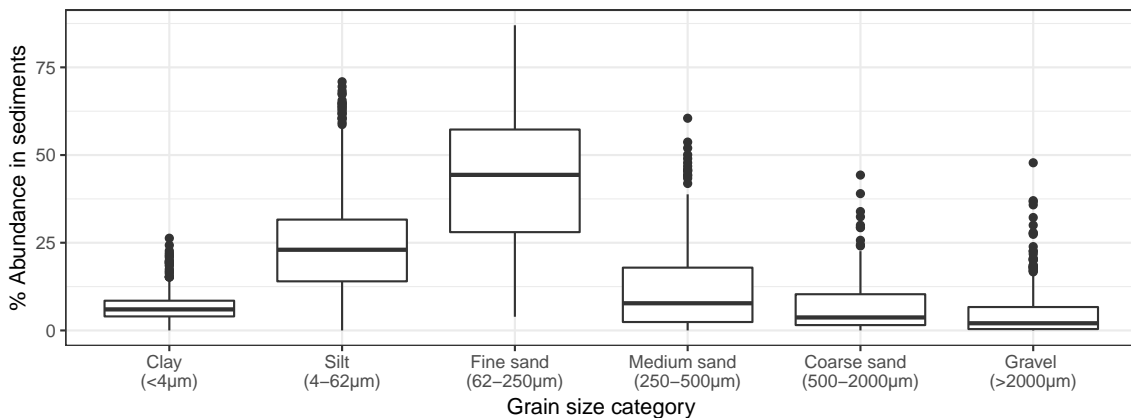


Figure 9: *The percentage abundance of different sediment grain sizes observed across the Munksgaard sediment sampling program.*

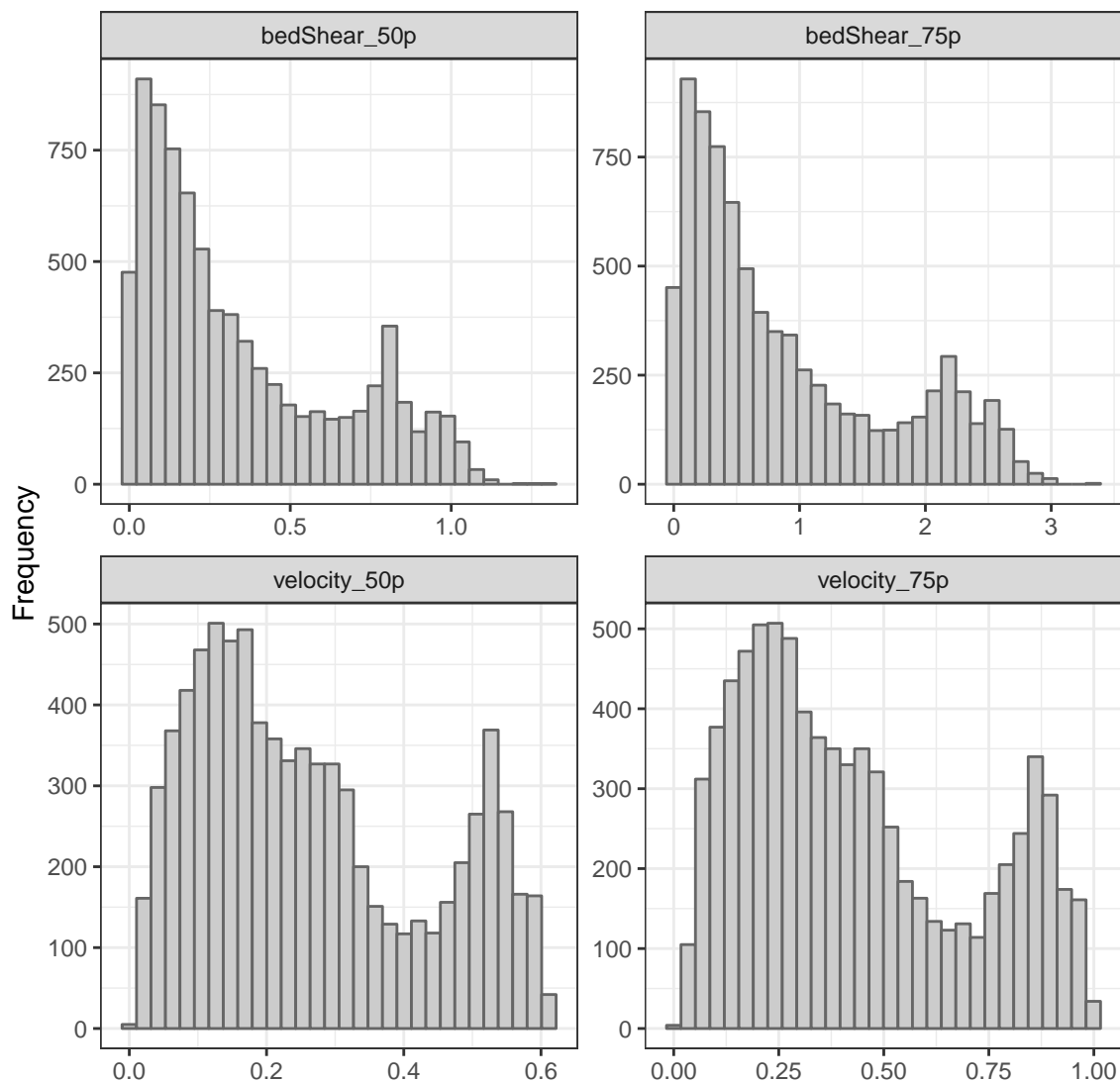


Figure 10: *Frequency distributions of hydrodynamic products in the East Arm area.*

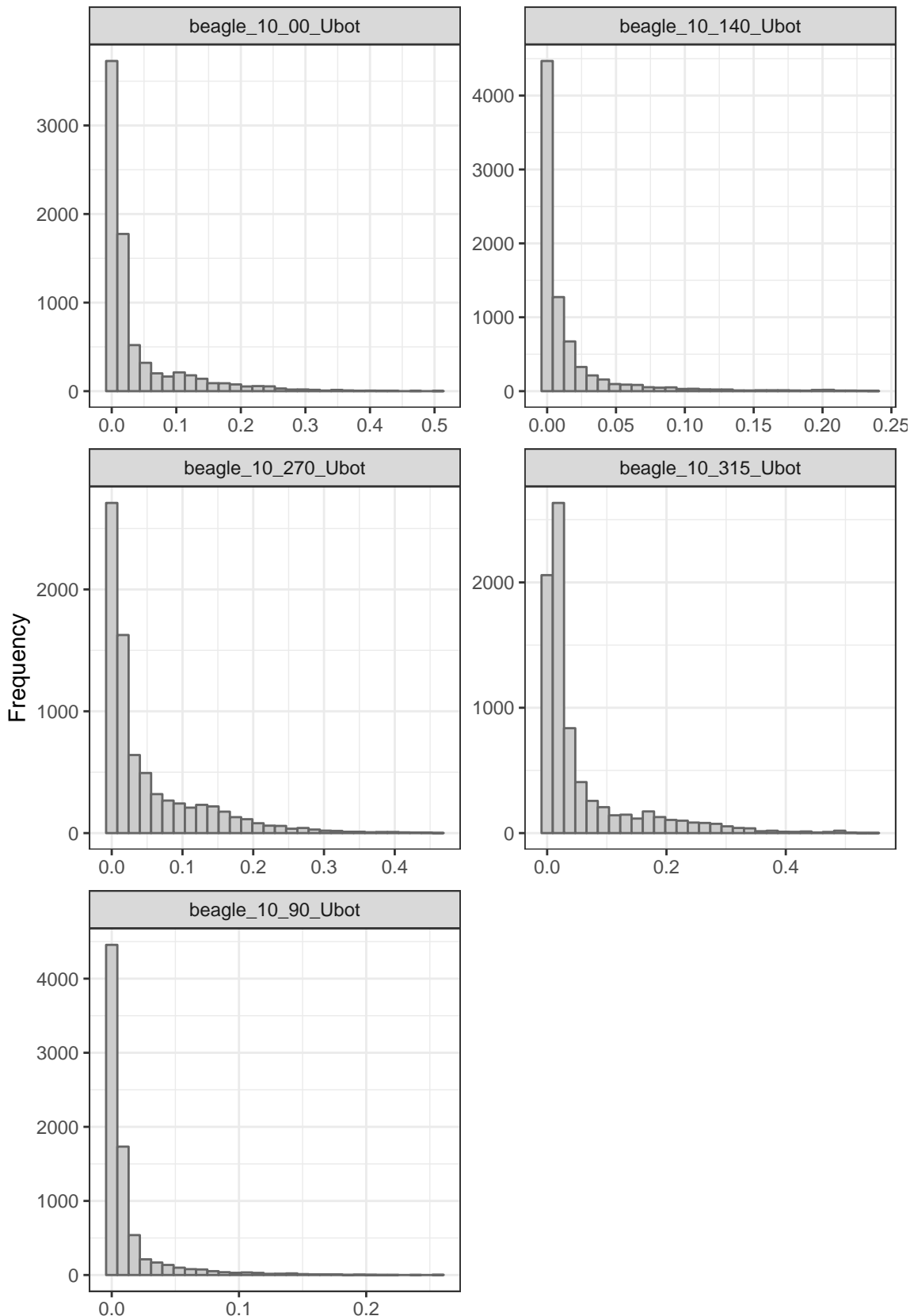


Figure 11: Frequency distributions of wave modelling seabed shear stress products in the East Arm area.

Both current velocity and seabed shear stress were derived from the same model and were thus closely correlated. Similarly, both wave derived orbital velocity and wave derived seabed shear stress were correlated. In each case, the shear stress proxies are intended to be expressions of the forces that are likely to be acting on the seabed (from tides and waves respectively). Hence only the seabed shear stress versions of the hydrodynamic and wave models were used as the proxy estimates of tidal and wave forces.

Figure 12 illustrates the resulting masks for the East Arm area using a threshold of 0.2 m/s (or 0.3 m/s for the 75th percentiles). Each of the wave derived seabed shear masks were added together and then joined with the 50 percentile hydrodynamic seabed shear mask. The resulting mask is illustrated in Figure 13. This mask represents (in blue shading) the areas most likely to experience more deposition than erosion and thus suitable areas for sediment monitoring. When we compared this mask to the spatial extent of the Munksgaard 2012 sediment monitoring site configuration, it was evident that while they broadly overlap, there was substantially less suitable area in the region adjacent to the City and substantially more in the East Arm reaches.

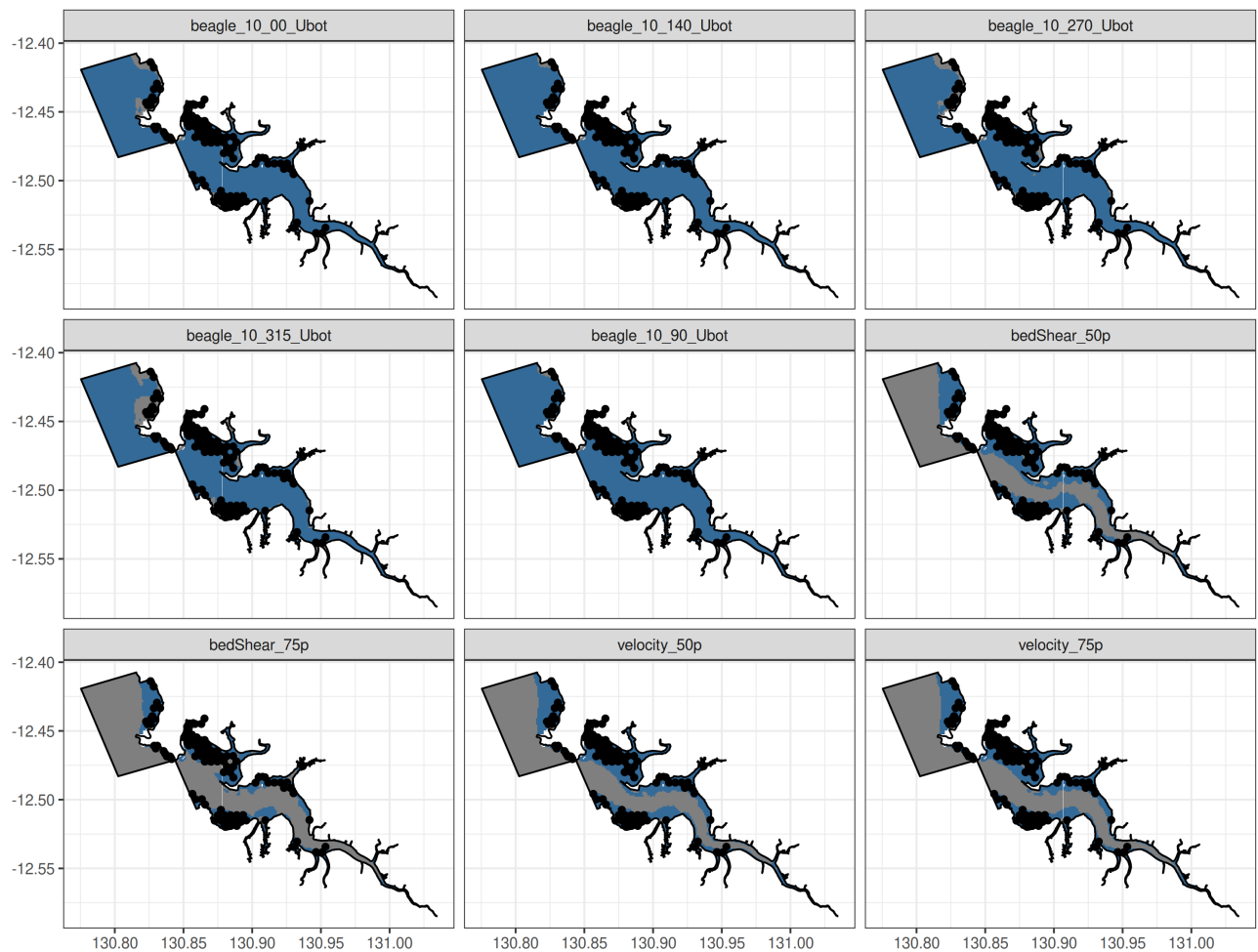


Figure 12: Individual East Arm masks from various hydrodynamic (bedShear_) and wave (beagle_) models categorised using a threshold values of 0.2 for all other than the 75th percentile products with use a threshold of 0.3 m/s. The blue areas indicate areas of predicted relatively low erosion and transport potential and thus good candidate areas for sample site allocation. The black dots illustrate the position of Munksgaard 2012 sediment sampling sites.

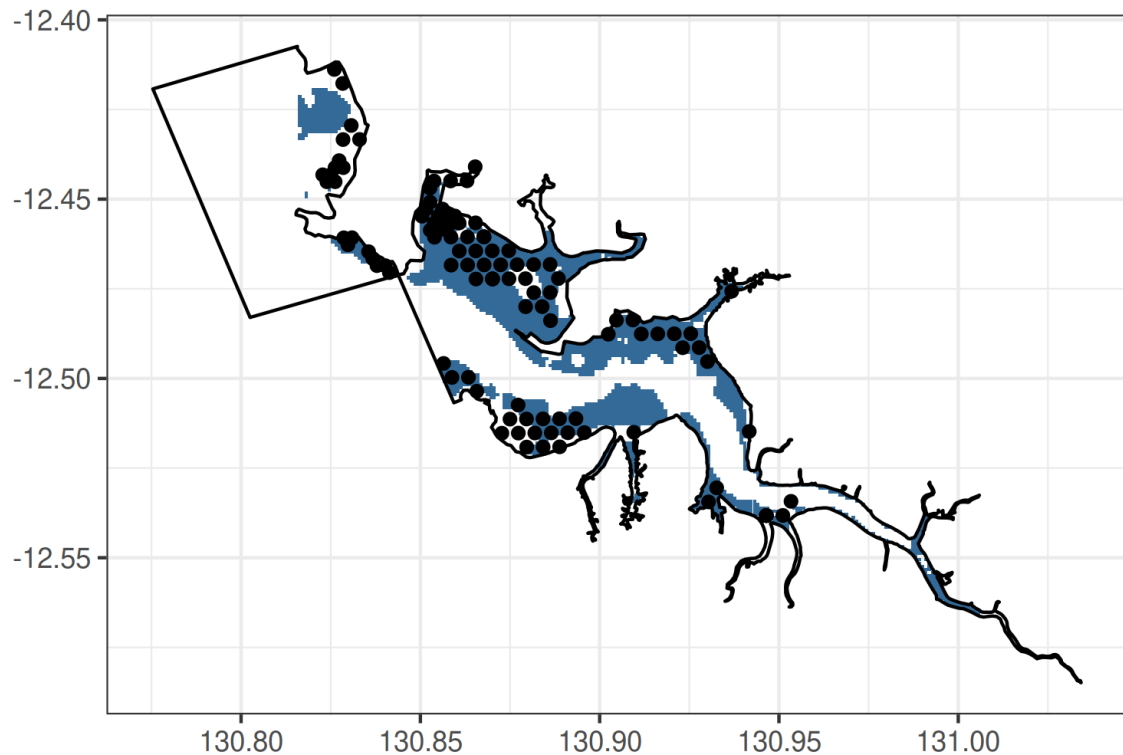


Figure 13: *East Arm mask derived from the combination of 50th percentile seabed shear stress and each of the wave derived seabed shear stresses. The blue areas indicate areas of predicted relatively low erosion and transport potential and thus good candidate areas for sample site allocation. The black dots illustrate the position of Munksgaard 2012 sediment sampling sites.*

2.6. Outer Harbour sampling domain

Figure 14 illustrates the distribution of percentage abundance of a range of particle sizes class categories from the Offsets Outer Harbour sampling program. The majority of particles were classified as sand. Based on Figures 7 and 8, it is likely that the majority of the sediment particles were between 0.1mm and 1mm and that this corresponds to critical deposition values of approximately 1 m/s to 5 m/s and 0.2-0.3 seabed shear stress.

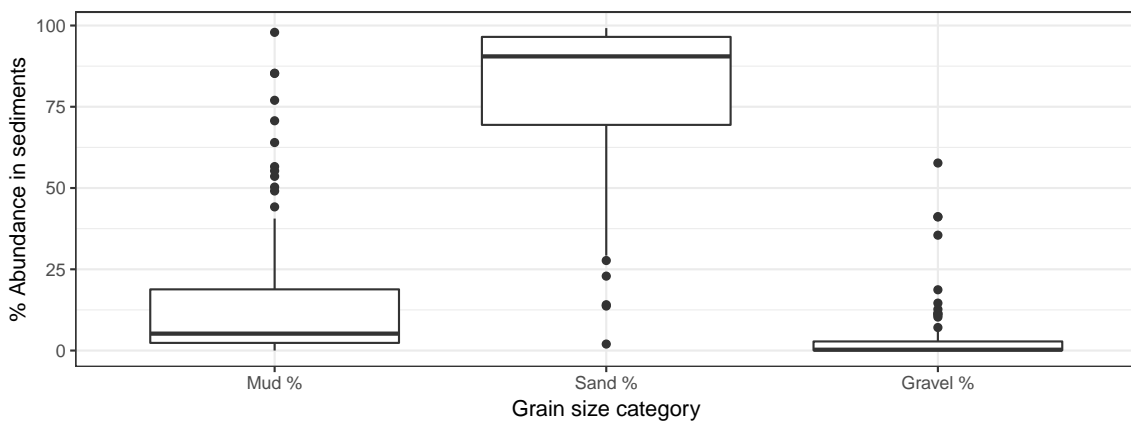


Figure 14: *The percentage abundance of different sediment grain sizes observed across the Offsets Outer Harbour sediment sampling program.*

The distribution of hydrodynamic seabed shear stress and velocity (Figure 15) had an initial valley at 0.3. The distribution of wave derived seabed shear stress and velocity is illustrated in Figure 16, however, and suggests that the majority of the Outer Harbour was un-affected by high erosive wave shear forces.

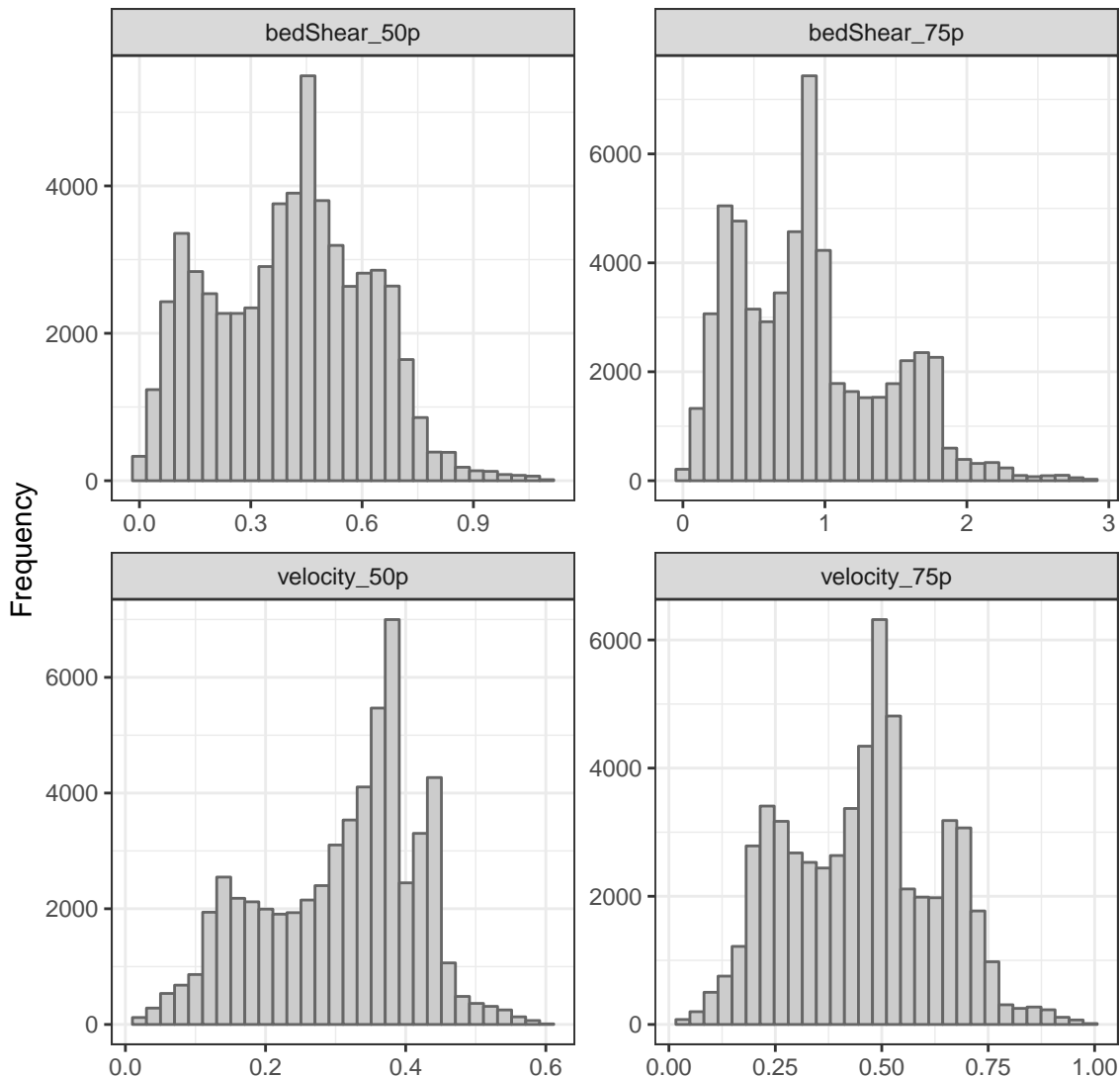


Figure 15: Frequency distributions of hydrodynamic products in the Outer Harbour area.

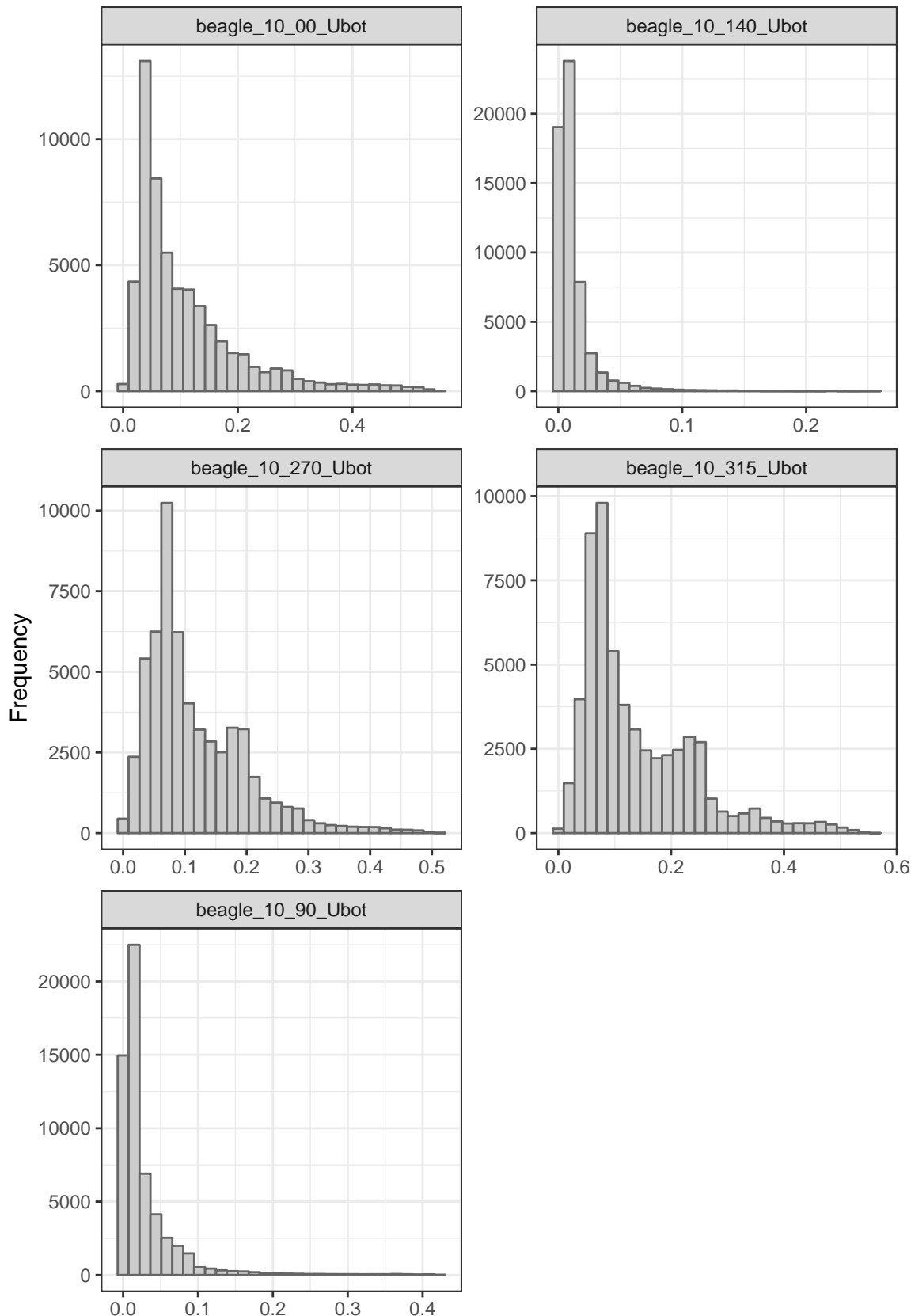


Figure 16: Frequency distributions of wave modelling seabed shear stress products in the Outer Harbour area.

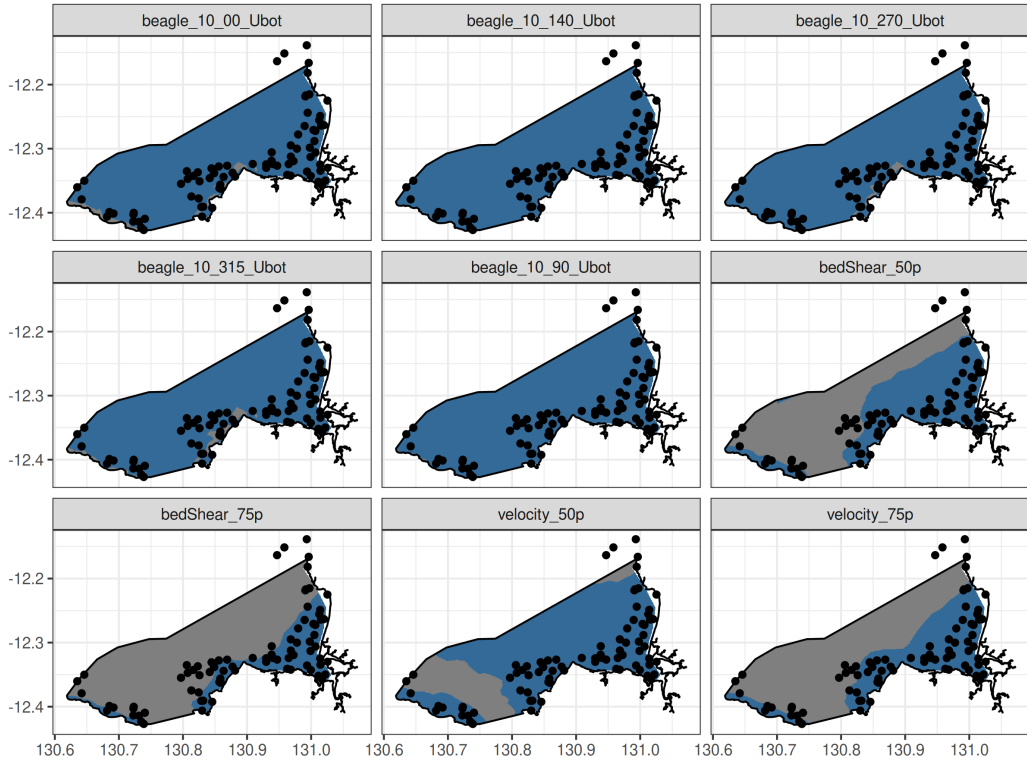


Figure 17: Individual Outer Harbour masks from various hydrodynamic (bedShear_) and wave (beagle_) models categorised using a threshold values of 0.2 for all other than the 75th percentile products with use a threshold of 0.3 m/s. The blue areas indicate areas of predicted relatively low erosion and transport potential and thus good candidate areas for sample site allocation. The black dots illustrate the position of Munksgaard 2012 sediment sampling sites.

A single combined mask, incorporating the 50th percentile seabed shear stress and each of the wave derived seabed shear stresses is illustrated in Figure 18 for Outer Harbour.

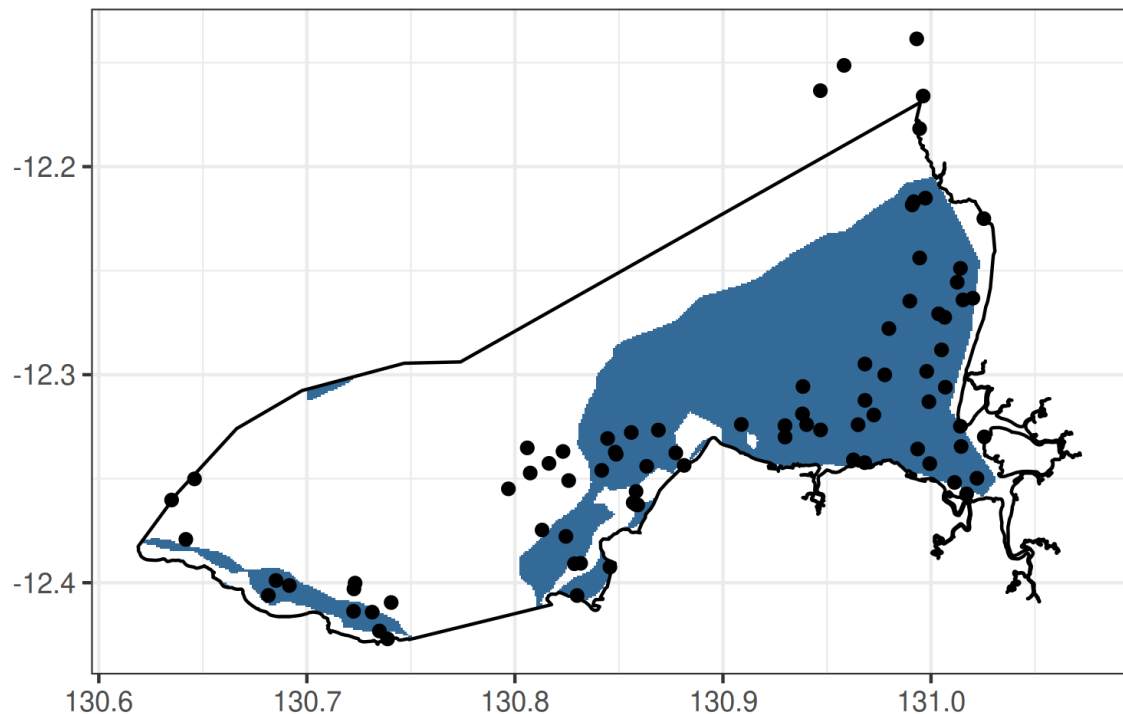


Figure 18: *Outer Harbour mask derived from the combination of 50th percentile seabed shear stress and each of the wave derived seabed shear stresses. The blue areas indicate areas of predicted relatively low erosion and transport potential and thus good candidate areas for sample site allocation. The black dots illustrate the position of Munksgaard 2012 sediment sampling sites.*

2.7. Exclusion zone masks

In addition to using hydrodynamic modelling masks to exclude areas that might be considered unsuitable for sediment monitoring, there are areas throughout Darwin Harbour that are not practical or appropriate for monitoring. These include the areas of a high probability of hard seabed (Siwabessy 2019), shipping channel and port exclusion zones as well as other exclusions zones associated with major infrastructure or military bases. Hence additional masks were developed from spatial layers provided by Lynda Radke.

Figures 19 and 20 illustrate the sampling masks associated with East Arm and Outer Harbour respectively.

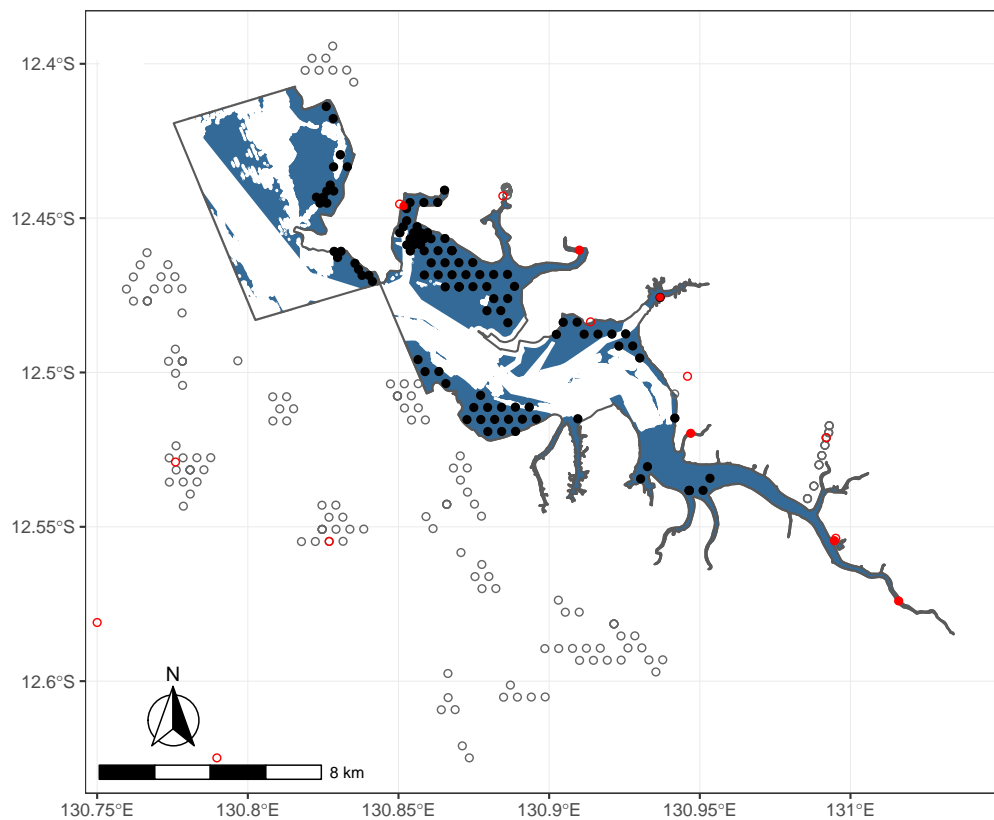


Figure 19: *East Arm mask derived from numerous exclusion zone shapefiles. The blue areas represent the spatial domain available for sampling. The black dots illustrate the position of Munksgaard 2012 sediment sampling sites. Red dots represent the designated sites. Open black and red circles represent samples that are outside of the East Arm area.*

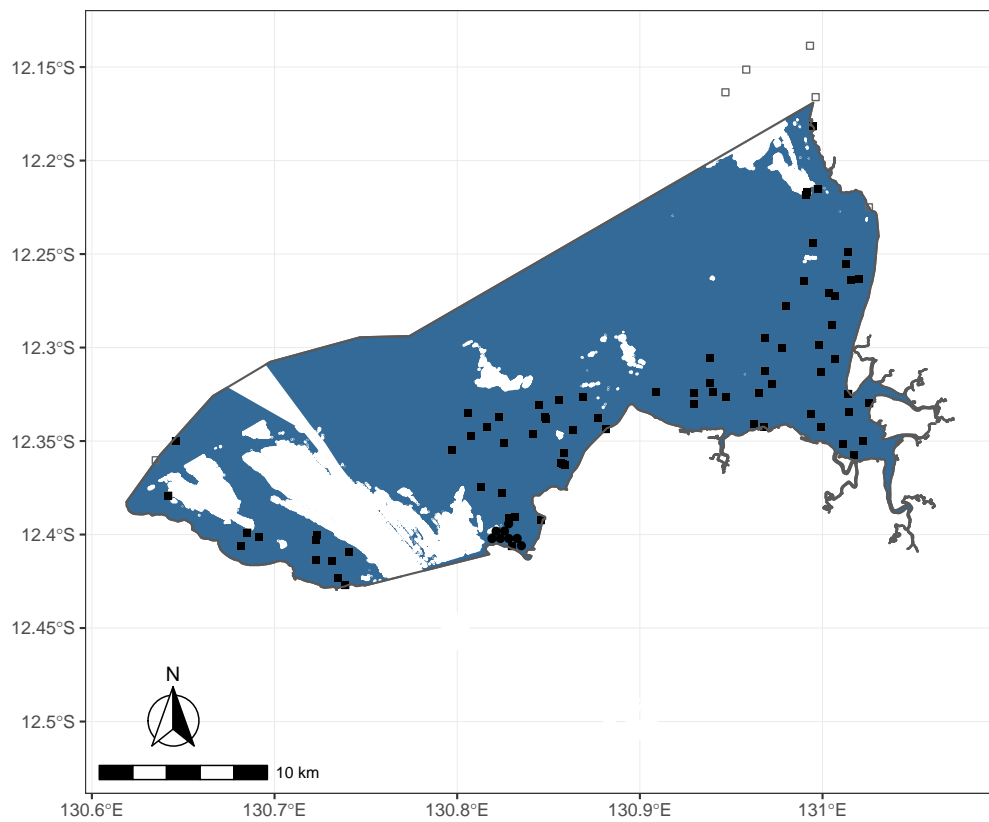


Figure 20: *Outer Harbour mask derived from numerous exclusion zone shapefiles. The blue areas represent the spatial domain available for sampling. The black dots illustrate the position of Outer Harbour sediment sampling sites. Open black circles represent samples that are outside of the Outer Harbour area.*

3. Spatial Model fitting

A target or set of targets is required against which the effectiveness and accuracy of candidate sampling designs can be tuned or gauged. This target should represent the full underlying conditions and in essence represent a saturated sampling design - a sampling design in which all possible locations/sites are sampled. Whilst this is logically not possible, given an adequate set of baseline data, statistical spatial models can be generated to estimate the underlying patterns. The resulting predicted layers can be used to represent the targets.

Spatial models are complex statistical models that attempt to recreate the full feature space from which a limited set of samples were collected. In so doing, they attempt to incorporate two-dimensional patterns and correlations to allow prediction to areas in between samples.

In the simplest cases, simple surfaces can be derived by linear interpolation between all the sampling points. However, when samples are distributed unevenly, there are strong spatial dependencies and/or the bounding domain is not a simple rectangle, more complex methodologies are required.

Ecological and environmental processes are often correlated through space. To account for these spatial dependencies within a spatial model it is useful to incorporate a Gaussian Random Field (GRF) which specifies a spatially dependent covariance structure in which locations that are closer to one another in space will in general be more highly correlated to one another than locations that are further apart.

Large or complex spatial models soon become intractable using a traditional frequentist modelling framework. By contrast, equivalent Bayesian models are typically very computationally expensive. Integrated Nested Laplace Approximation (INLA: Rue, Martino, and Chopin 2009) is a Bayesian approximation framework that offers the philosophical advantages of a full Bayesian approach, yet with the computational efficiency of frequentist approaches.

We can consider a GRF to be stationary if the degree of correlation between two points is dependent only on the distance between the points, or non-stationary if we allow the correlation function to vary over the landscape. An extreme form of non-stationary model occurs when there are physical barriers that disrupt or block the flow of contagious processes. In such cases, just because two locations are in close proximity, does not necessarily mean that they will be highly correlated. Consider a simple example of the diffusion of a dye in water throughout a tank. The dye will spread out from the source and gradually disperse throughout the tank. Consequently, the correlation between the concentration of dye at any two locations during dispersion will be dependent on the distance between the two locations. If however, the tank had a partial barrier that restricted the flow of dye molecules, then two locations either side of the barrier might have very different dye concentrations despite being in close proximity. Barrier models are able to account for these obstructions.

$$\begin{aligned}
 y_i &\sim \Gamma(\mu_i, \alpha) \\
 \log(\mu_i) &= \beta_0 + u(s_i) + \varepsilon_i \\
 \beta_0 &\sim N(0, 1000) \\
 u(s_i) &\sim GRF(r, \sigma_u) \\
 \varepsilon_i &\sim N(0, \sigma^2) \\
 \pi(\sigma_e) &\sim \lambda_e e^{-\lambda_e \sigma_e} \\
 \pi(\sigma_u) &\sim \lambda_0 e^{-\lambda_0 \sigma_u} \\
 \pi\left(\frac{1}{r}\right) &\sim \lambda_1 e^{-\lambda_1 \frac{1}{r}}
 \end{aligned}$$

where y_i is the i th observation of the target chemical variable, ε_i is the independent and individually variable random effect used to model the very short range erratic dependencies and $u(s_i)$ is the Gaussian Random Field and is used to model the long-range structural (autocorrelation) dependencies. A diffuse prior is applied to the intercept (β_0) and ε_i a vector of independent Gaussians. The Matern family spatial random

effect ($u(s_i)$) and its covariance is defined by two parameters: the range (r : represents the length scale of the spatial dependencies) and standard deviation (σ_u : representing the ratio of spatial to independent noise). The smaller the range, the lower the correlation between two proximal locations.

In a boundary model, two different range parameters (r) are applied. One of the range parameters is applied to the boundary area (in this case land) and the other to the focal area (in this case Harbour). By setting the boundary range smaller (and close to zero) than the focal area range, the dependency structure across boundaries is disrupted and approach zero.

Hyper-parameter priors for the random effects (σ_e , σ_u) as well as r are defined in terms of a λ parameter which is determined by the scale of the response (on the log scale in this case). Both λ_e and λ_0 were set to the median value of the target response (on a log scale). and the focal area r was set to half the width of the spatial domain after (Bakka et al. 2016).

The random field was approximated via a Constrained Refined Delaunay Triangulation (CRDT) mesh. The mesh comprised of an inner region that surrounded all the Munksgaard sediment monitoring sites as well as an outer mesh provides a buffer to help ensure estimates close to the inner mesh boundary are robust. In doing so, the maximum permissible triangle edge length for the inner and outer mesh regions was set to 0.01 and 0.04 (units of latlong projection) respectively. The smaller the values, the finer the mesh. This mesh was then projected onto the location of the observed sample location.

The above models were fit for each of the sediment chemical recorded in the Munksgaard 2012 sediment sampling program. Figure 49 provides an example of the major elements of one of the chemical (Zinc) spatial models. Equivalent figures for the other chemicals are presented in Appendix A.

Figure 49a depicts the random field mesh with the Munksgaard 2012 sampling sites and Harbour boundary overlayed. Figure 49b illustrates the boundary used for the barrier in the spatial model and Figure 49c illustrates the final predicted spatial layer (with original sample data overlayed) for Zinc within the East Arm area. For comparison, both predicted (model output) and observed (Munksgaard samples) are presented on the same colour scale. Figure 49c illustrates the final predicted spatial layer for Zinc within the East Arm area and where the colour scale is based purely on the range of predicted values.

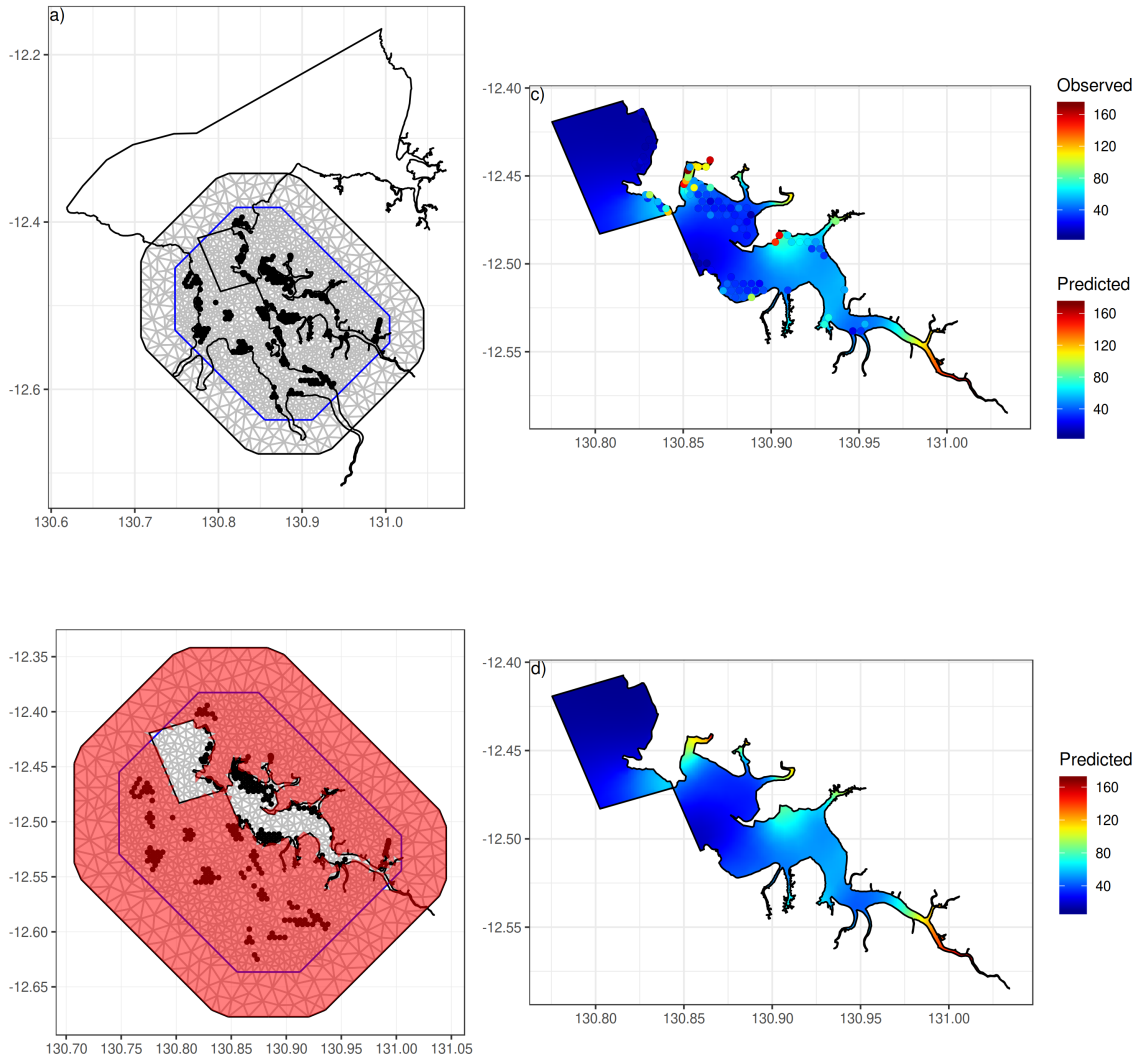


Figure 21: *Integrated Nested Laplace Approximation (INLA) barrier spatial modelling of Zinc.* The diagram illustrates a) the mesh, b) the barrier mask, c) the resulting predicted 2D surface (and observed training data as points) and d) the resulting predicted 2D surface scaled to the range of predictions.

Although the shrinkage in models is a little high (there is a tendency for the magnitude of change over space to be dampened), generally the models do a very good job of depicting the relative patterns of change in space. For this application, the absolute scale of the changes in patterns are not important (only the relative patterns), since in order to gauge the accuracy of any candidate sampling designs, it is necessary to standardize the patterns anyway. Hence it is more important that the model depict the general patterns in the observed data than the exact values of the observed data.

4. Sampling

Ideally, a good sampling design should comprise a configuration of sites that collectively represent the broader area as efficiently as possible. In this context, efficiency is a compromise between complete representation (resulting from saturating the spatial domain with sites) and minimizing sampling effort.

There are numerous approaches for generating candidate sampling configurations. Irrespective of the approach, there must be a metric by which the suitability of the configuration can be gauged. If we assume that full saturation must provide maximum representation, then all other configurations can be gauged relative to the full saturation. Hence a measure of how well a configuration is likely to represent the full spatial domain is the difference between some empirical property calculated from the candidate configuration and full saturation. For example, we could calculate the difference between the estimated mean Magnesium from a candidate configuration and the equivalent mean calculated from the full saturation. The magnitude of this difference is thus a measure of the inaccuracy and thus suitability of the candidate configuration.

In the current application, there are numerous sediment chemicals that can be used to describe the underlying conditions within the spatial domain. Consequently, the metric needs to incorporate the differences across each of the chemicals. The following metric will be adopted.

$$\text{MeanError} = \frac{1}{n} \sum_{i=1:n} \frac{\text{abs}(\bar{e}_i - \bar{s}_i)}{r_i}$$

$$\text{MaxError} = \max_{i=1:n} \frac{\text{abs}(\bar{e}_i - \bar{s}_i)}{r_i}$$

$$\text{MinError} = \min_{i=1:n} \frac{\text{abs}(\bar{e}_i - \bar{s}_i)}{r_i}$$

where \bar{e}_i and \bar{s}_i are the estimated domain means of the i^{th} chemical (out of n) from the candidate and full saturation configurations respectively and the normalizing constant (r_i) is the difference between maximum and minimum predicted values for the i^{th} chemical. There are three metrics presented so capture three broad characteristics of the 'accuracy' of the candidate sampling designs:

- MeanError - this is a measure of the average deviation between the estimated zone mean (from the candidate model) and target mean from across all chemical species.
- MaxError - this is a measure of the maximum deviation between the estimated zone mean (from the candidate model) and the target mean from across all chemical species.
As a maximum, it can be used to compare the worst performing aspects of each candidate and thus acts as a worst case scenario.
- MinError - this is a measure of the minimum deviation between the estimated zone mean (from the candidate model) and the target mean from across all chemical species. As a minimum, it can be used to compare the best performing aspects of each candidate and thus acts as a best case scenario.

Random sampling

The simplest approach to generating a spatial sampling design is to repeatedly simulate sampling from the spatial domain with a range of sample sizes and use the above metric to help determine the optimum sampling size and configuration. Given a sufficiently large sample size, random sampling should provide an unbiased and representative sampling design. However, it is highly likely that at low sample sizes this approach will not yield highly representative samples (high *Error*). Yet increasing the sample size should result (on average) in lower *Error* (= greater accuracy). To counter the natural stochasticity associated with simulation, we repeat each sample size five times.

Sampling on a regular grid

In the simple random sampling approach above, each simulated random draw was independent of all other draws. As a result, all configurations are possible - even those in which multiple samples are aggregated together in close proximity. In the absence of any prior knowledge about the underlying environmental conditions and heterogeneity, an even and regular spread of samples can ensure that the sampling design does offer general representativeness. Grids of increasing sample size offer progressively finer granularity and thus the ability to detect smaller scale perturbations in space.

Conditioned Latin Hypercube Sampling

In drawing both random samples and regular grid samples, the process is completely naive to the underlying environmental conditions. Consequently, they were only likely to be representative once a large number of samples were been collected. Conditional Latin Hypercube Sampling (cLHS) is a robust and efficient statistical sampling procedure that generates samples based on the variability within a multidimensional covariate feature space (Minasny and McBratney 2006a). Since the sampling process is supervised by the underlying conditions (or proxies thereof), for a given sample size, the resulting candidate sampling configurations are more likely to yield samples that are representative of the complex underlying conditions.

In introducing the procedure, Minasny and McBratney (2006a) provided a real world example of a soil mapping project in which relatively small samples sizes generated by cLHS closely represented the original distribution of a set of environmental covariates. Furthermore, Minasny and McBratney (2006b) found cLHS superior (in terms of accuracy) to a range of alternative sampling procedures including random and stratified random sampling.

Spatially balanced design

Whilst regular grid sampling designs do space samples out throughout the spatial domain, they do have the potential to introduce biases due to any underlying systematic processes that might align with the design (albeit unintentionally) and do not necessarily provide good representation. On the other hand, random sampling designs offer some degree of protection from those biases. The shear nature of randomization means that it is possible that some sampling locations can be clustered in very close proximity. When this is the case, not only does it waste valuable sampling effort (as there is not need to provide multiple estimates of the same location), it introduces another bias. Any resulting estimates from the sampling design will be biased towards the clustered sample conditions as those conditioned are effectively weighted higher by virtue of the greater sampling effort.

The ideal design is to be able to have a random configuration that still prevents the clustering of samples. In affect, a way to generate random locations whose probability of selection is proportional to the distance from all already selected sites. This is the inspiration behind **Spatially balanced designs**.

There are numerous spatially balanced designed techniques. Some such as Generalized Random-Tessellation Stratified (GRTS), map the full two dimensional spatial domain into a single dimension (in a way that preserves the spatial ordering) before applying a systematic π_{ps} sampling technique to ensure a balanced distribution of samples throughout the spatial domain. Grafström, Lundström, and Schelin (2012) introduced an alternative technique in which unequal inclusion probabilities are generated via a pivotal method.

A further (and perhaps alternative) ideal is to be able to have a balanced design not only based on spatial proximity, but also on the basis of dissimilarity of underlying conditions. Spatial areas that are homogeneous with respect to some underlying sampling conditions require fewer sampling locations to characterise the underlying patterns than areas that are relatively heterogeneous. The spatially balanced design via pivotal method allows any number of dimensions to determine the inclusion probabilities.

A key determinant in selecting which of the above techniques to adopt is based on an evaluation of the purpose of the sampling design. If for example, the purpose is to characterise the overall condition

mean, then a 2D spatially balanced design is arguably most appropriate as it should represent the general underlying conditions. If on the other hand, the purpose is to be able to model the underlying patterns and understand where any changes in these patterns occur, then arguably a design that has been optimised around the underlying conditions (such as a n-dimensional spatially balanced design or conditioned latin hypercube sampling technique) is arguably more appropriate.

4.1. East Arm

For a range of sample sizes (5, 10, 20, 30, 40, 50, 60, 70, 80, 90, 100, 120, 200, 1000), for East Arm, each of the above sampling approaches was repeated five times. For each run, the *Error* metric was calculated. The results are presented in Figures 22 (mean error) and 23 (max error). As expected, as the sample sizes increase, the error declines. The simple random sampling design performs worst. The regular grid sampling is better than the random sampling. Whilst clusters of samples might be appropriate for representing conditions when the conditions cluster correspondingly, totally random samples are highly unlikely to resemble the correct cluster configuration. The non uniform distribution of cLHS on the other hand was directly due to the clustering patterns in the underlying conditions and thus it was not surprising that this technique had the least error.

Interestingly, the reduction in error after a sample size of 50 is relatively mild (notwithstanding that the figure is presented on a log-y scale). For each of sample sizes 50, 60, 70, 80 and 100, the best (based on lowest error) cLHS configuration is presented in Figure. Comma delimited text files are also available with the Latitude and Longitudes of these coordinates.

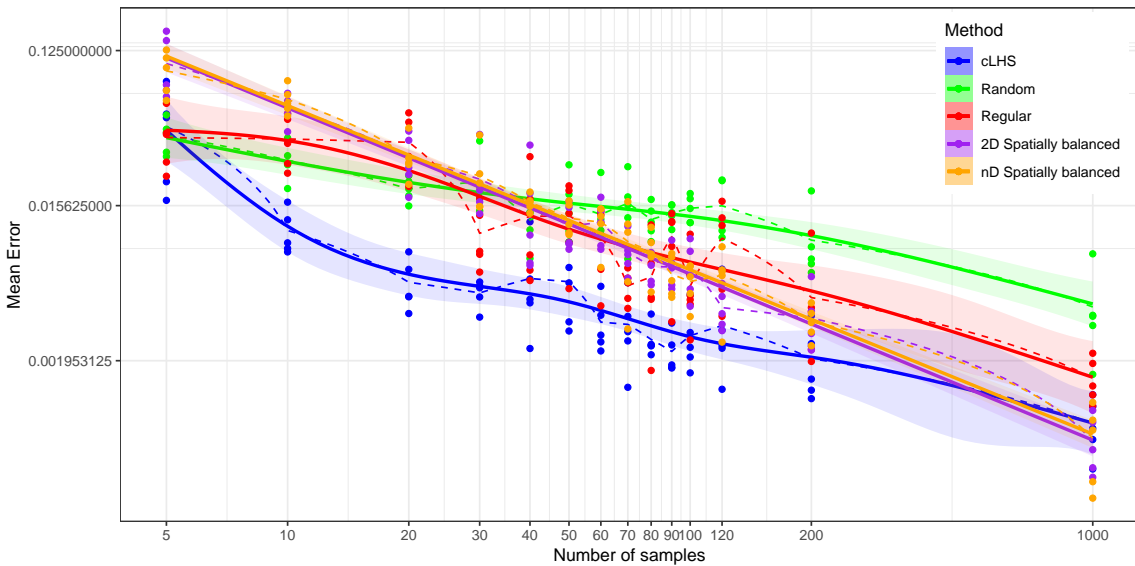


Figure 22: Comparison of the mean *Error* conditional on sample size and sampling method for the East Arm

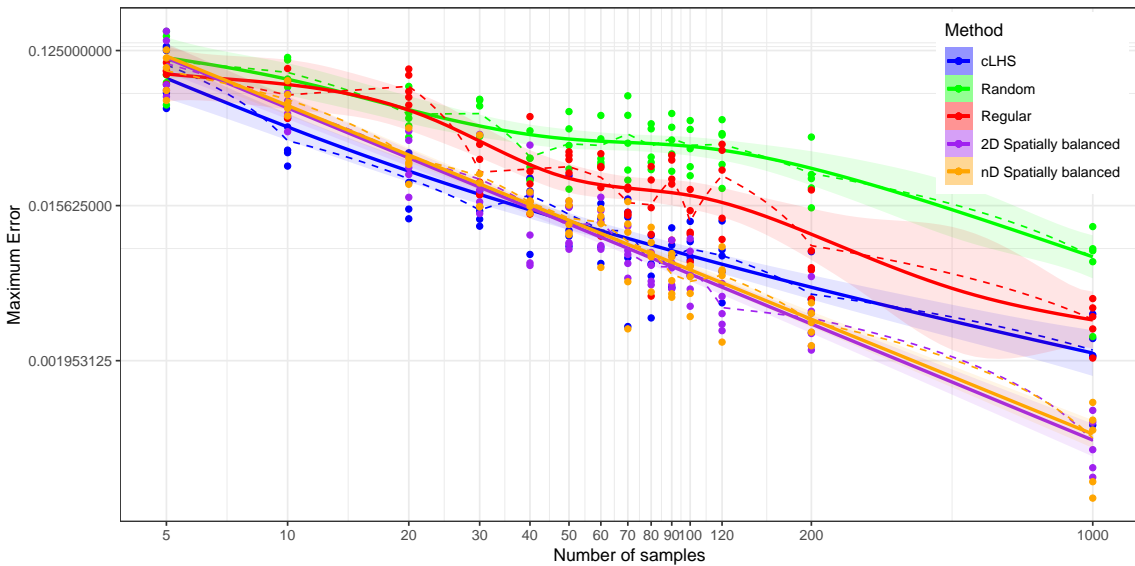


Figure 23: Comparison of the maximum Error conditional on sample size and sampling method for the East Arm

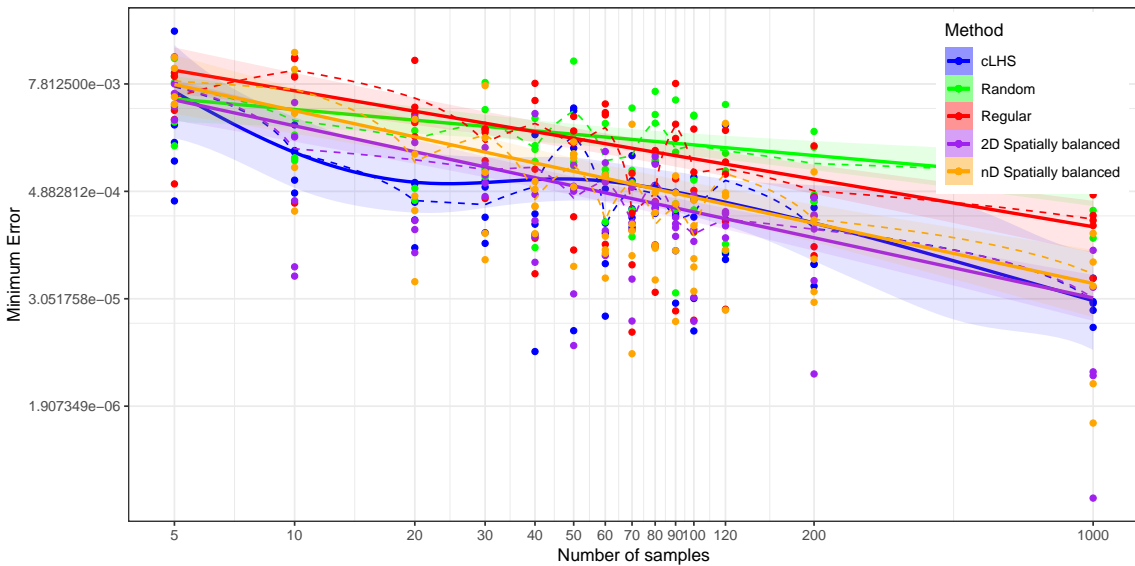


Figure 24: Comparison of the minimum Error conditional on sample size and sampling method for the East Arm

On the basis of Figures 22, 23 and 24 we could conclude that a sample size of 100 within East Arm is a sound choice, although it is likely that as few as 50 could still potentially yield similar overall patterns. The sample size of 100 also accommodates a buffer against sample loss. Nevertheless, this entire simulation process is contingent on a number of unverifiable assumptions:

1. that the Munksgaard 2012 sediment sampling data are representative of the typical conditions and spatial patterns.
2. all Munksgaard 2012 sediment chemicals are equally useful and informative.
3. the INLA models are able to fully represent the true underlying conditions.
4. the costs and logistics of sampling are equal irrespective of location.

The conditioned latin hypercube sampling technique consistently outperforms the other techniques. Interestingly, there was very little difference between the 2D and nD Spatially balanced designs. This suggests that either the sediment chemicals were relatively homogeneous over space or else patterns in one chemical species was countered by patterns in another chemical species.

The conditioned latin hypercube sampling technique appeared to be able to tune its design on the underlying sediment chemical patterns better than the spatially balanced designs. Thus if the above assumptions are reasonable and the main intention of the sampling was to be able to describe the patterns in the sediment chemicals, then the sampling design derived from this technique seems most appropriate.

If however, the purpose of the sampling design was be provide an unbiased representative sample of the general conditions across the spatial domain, then it could be argued that the 2D spatially balanced design was most appropriate - particularly if there was any doubt in the above assumptions.

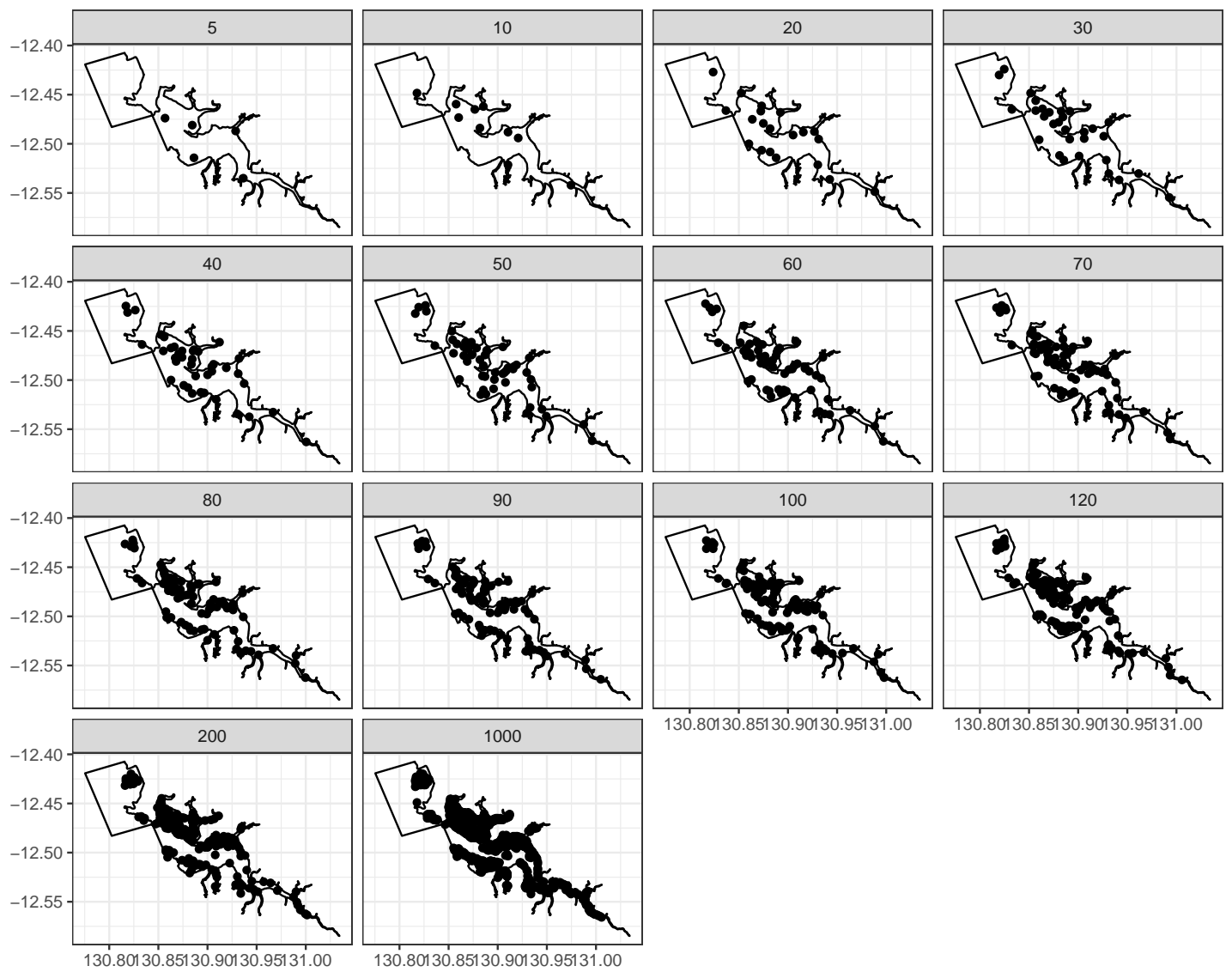


Figure 25: Sampling configurations associated with the lowest mean Error for each sample size for cLHS for the East Arm

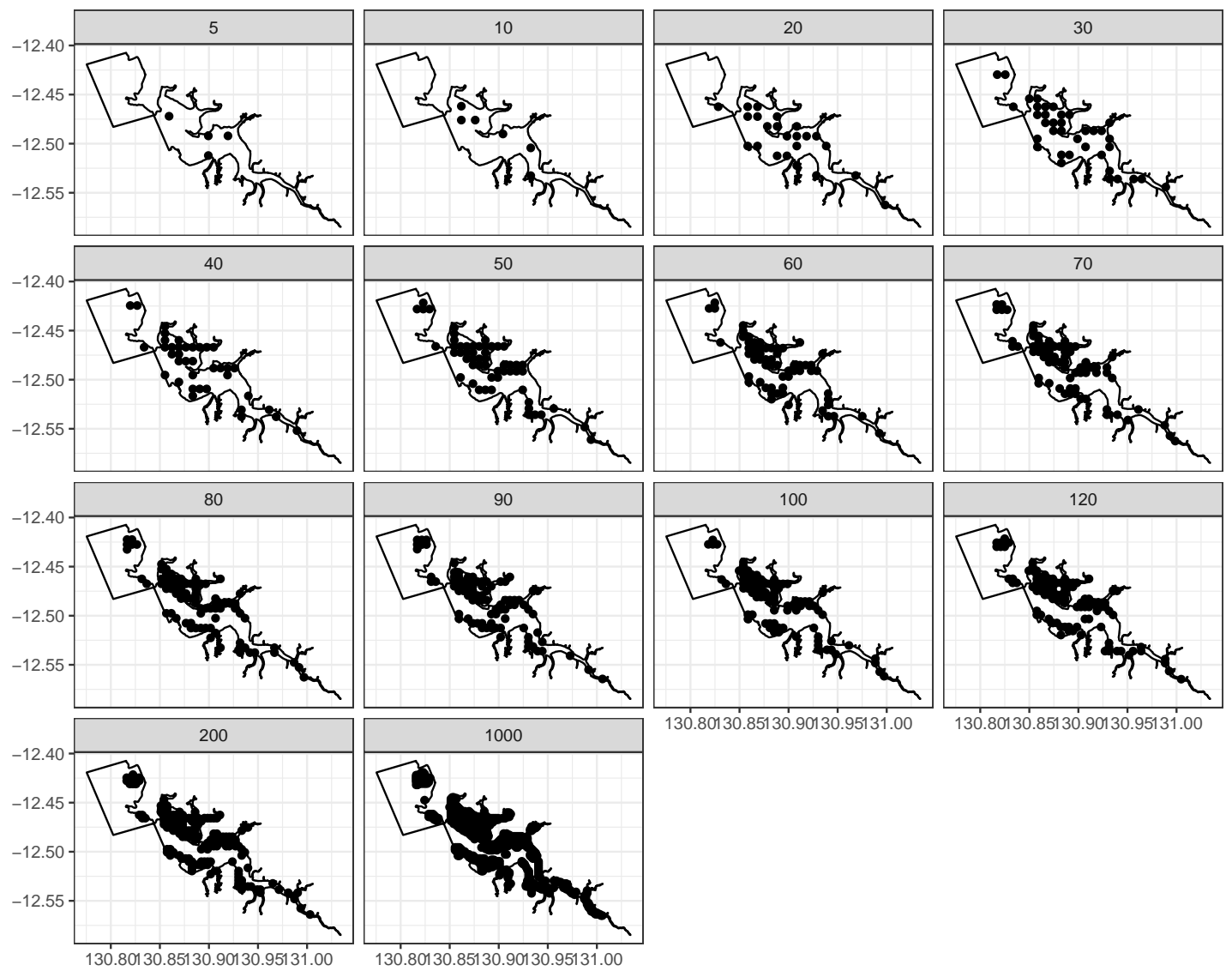


Figure 26: Sampling configurations associated with the lowest mean Error for each sample size for Regular grid sampling for the East Arm

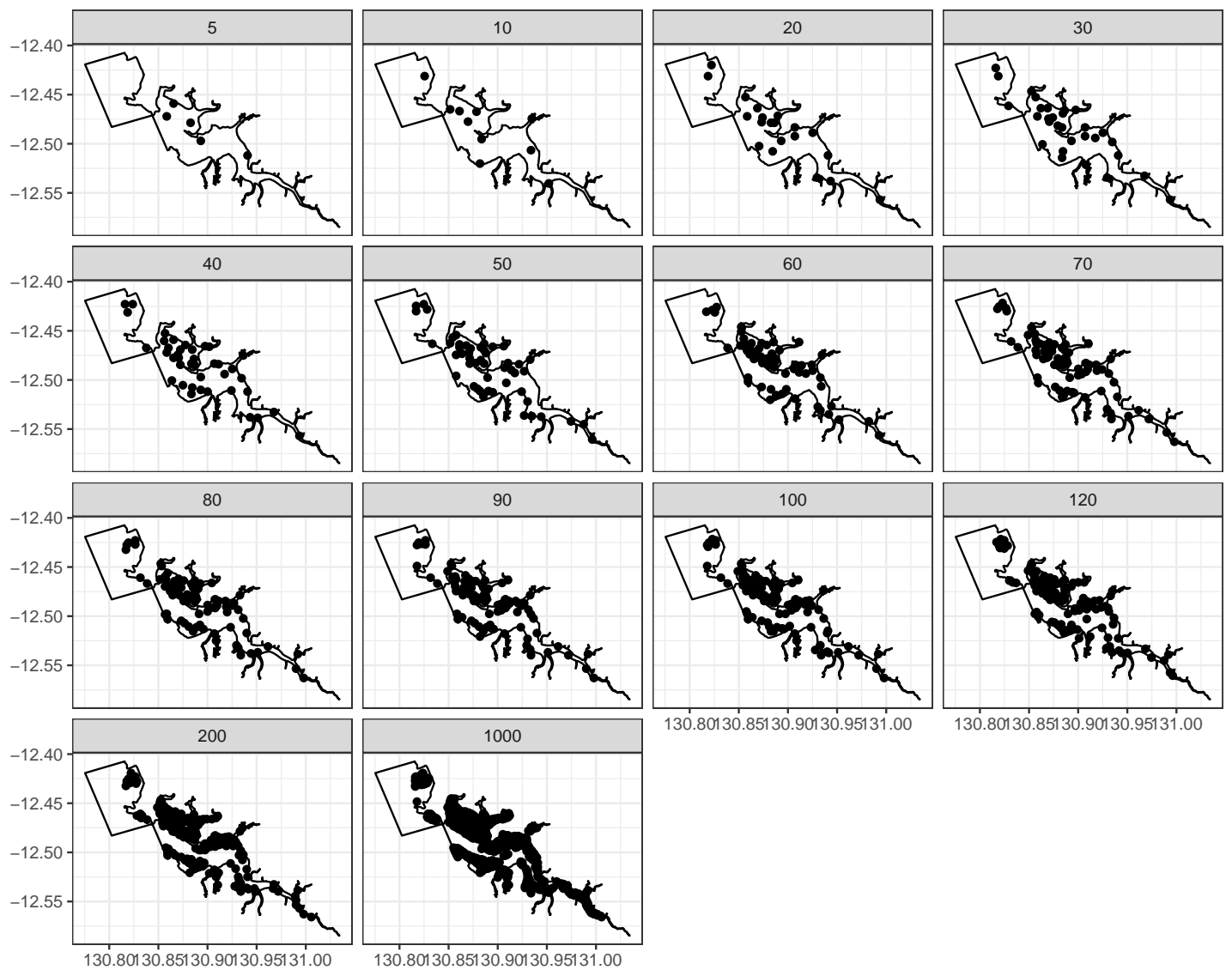


Figure 27: Sampling configurations associated with the lowest mean Error for each sample size for nD Spatially balanced sampling for the East Arm

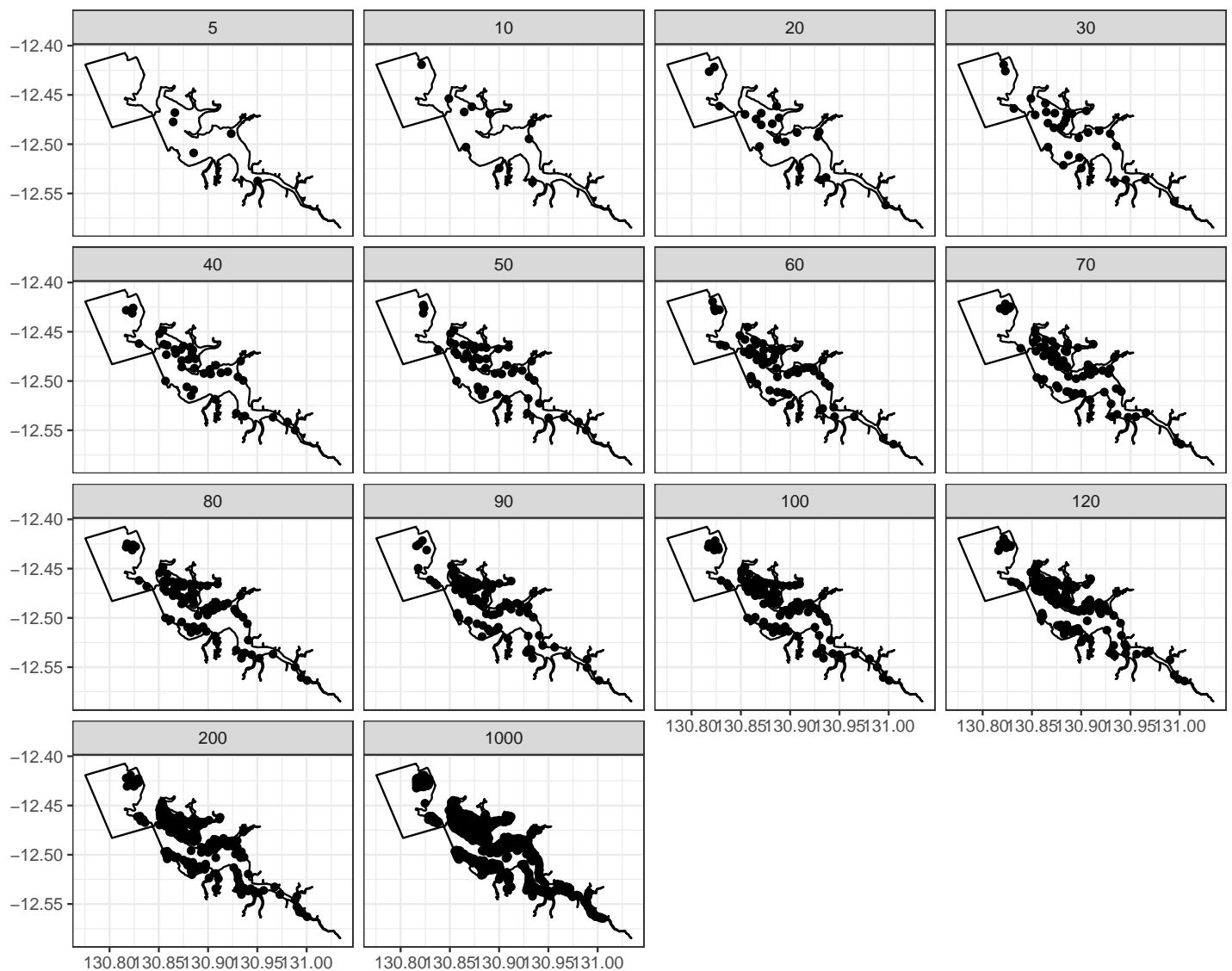


Figure 28: Sampling configurations associated with the lowest mean Error for each sample size for 2D Spatially balanced sampling for the East Arm

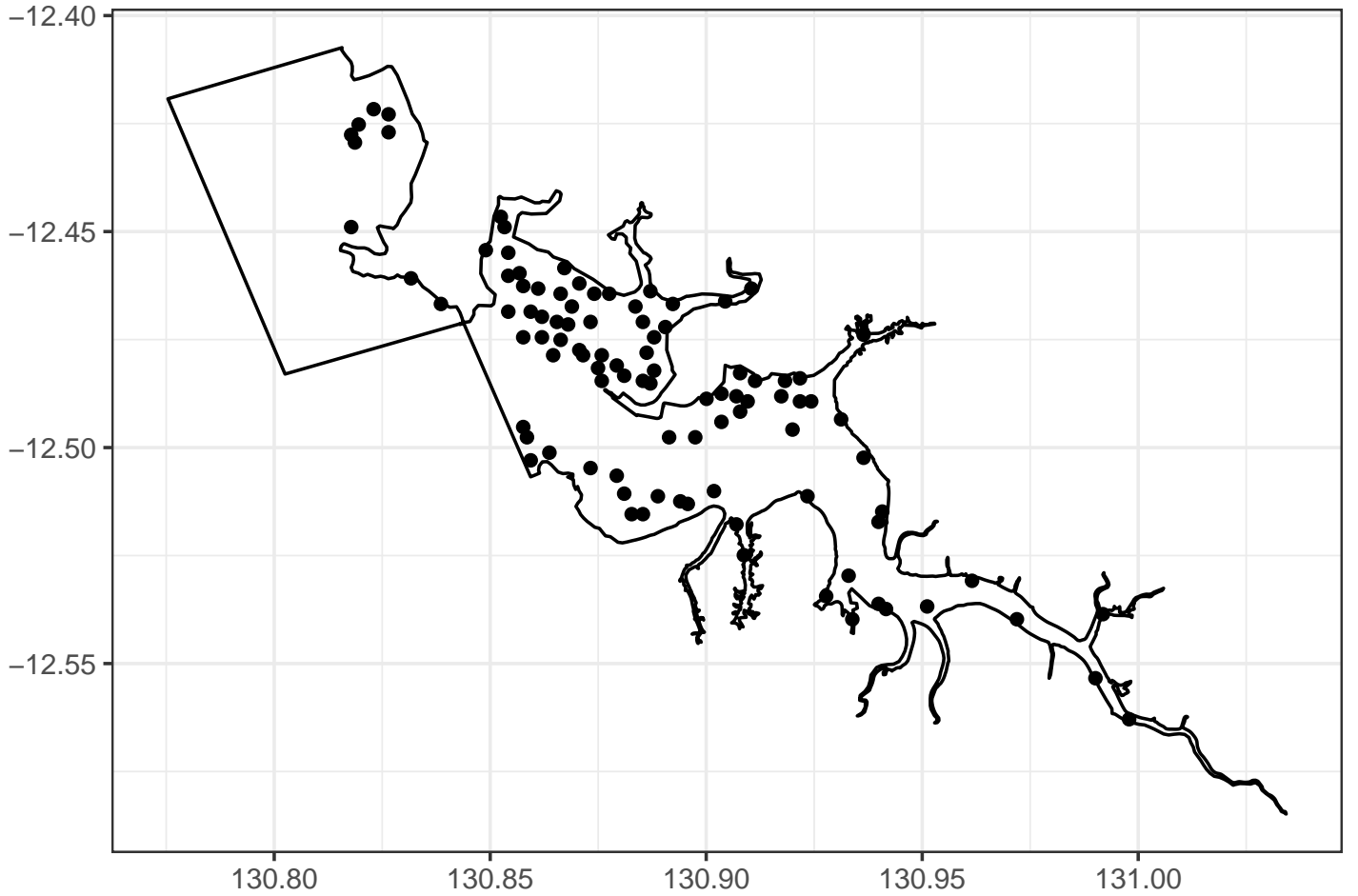


Figure 29: Two dimensional spatially balanced sampling configuration for the East Arm (100 samples)

4.2. Outer Harbour

For a range of sample sizes (5, 10, 20, 30, 40, 50, 60, 70, 80, 90, 100, 120, 200, 1000), for Outer Harbour, each of the above sampling approaches was repeated five times. For each run, the *Error* metric was calculated. The results are presented in Figures 30 (mean error) and 31 (max error). As expected, as the sample sizes increase, the error declined. The simple random sampling design performs worst. The regular grid sampling was better than the random sampling. Whilst clusters of samples might be appropriate for representing conditions when the conditions cluster correspondingly, totally random samples are highly unlikely to resemble the correct cluster configuration. The non uniform distribution of cLHS on the other hand was directly due to the clustering patterns in the underlying conditions and thus it is not surprising that this technique had the least error.

Interestingly, the reduction in error after a sample size of 50 was relatively mild (notwithstanding that the figure is presented on a log-y scale). For each of sample sizes 50, 60, 70, 80 and 100, the best (based on lowest error) cLHS configuration is presented in Figure.. Comma delimited text files are also available

with the Latitude and Longitudes of these coordinates.

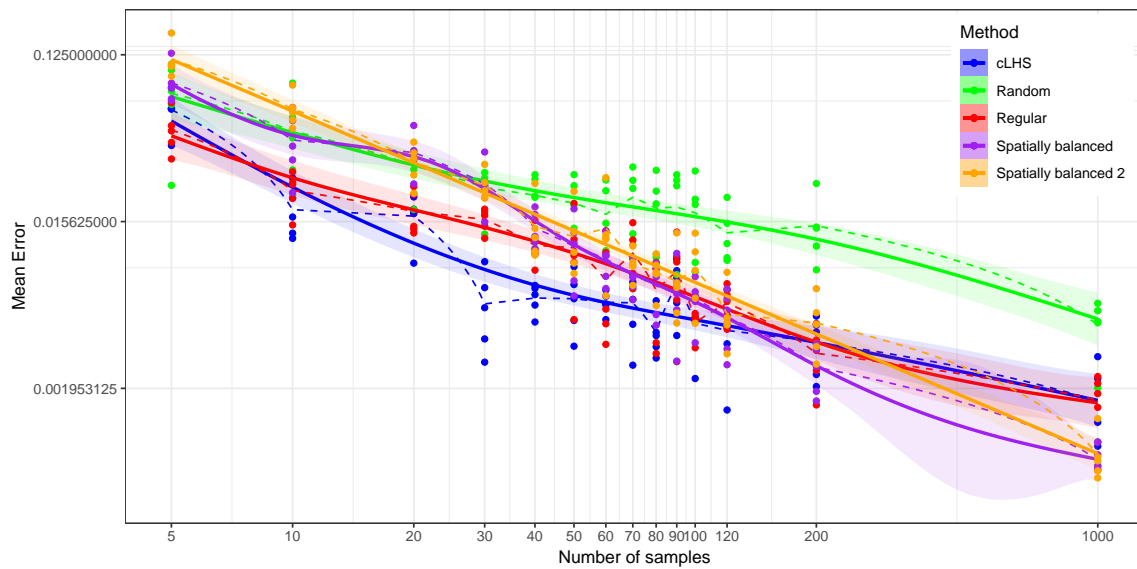


Figure 30: Comparison of the mean Error conditional on sample size and sampling method for the Outer Harbour

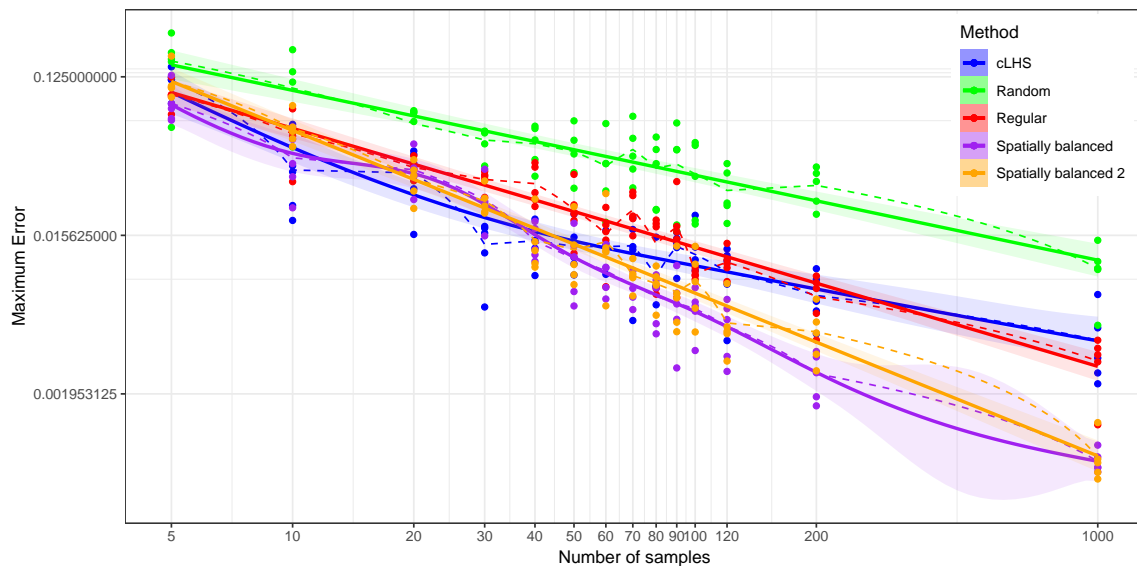


Figure 31: Comparison of the maximum Error conditional on sample size and sampling method for the Outer Harbour

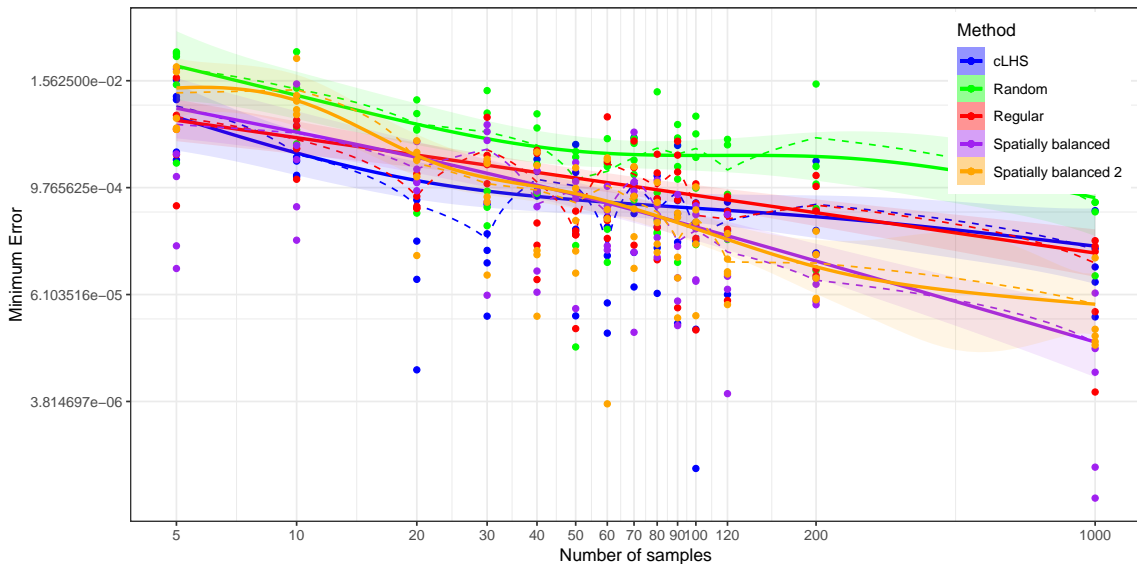


Figure 32: Comparison of the minimum Error conditional on sample size and sampling method for the Outer Harbour

On the basis of Figures 30, 31 and 32 we could conclude that a sample size of 100 within Outer Harbour was a sound choice, although it is likely that as few as 50 could still potentially yield similar overall patterns. The sample size of 100 also accommodates a buffer against sample loss. Nevertheless, this entire simulation process is contingent on a number of unverifiable assumptions:

1. that the Offset Outer Harbour sediment sampling data are representative of the typical conditions and spatial patterns.
2. all Offset Outer Harbour sediment chemicals are equally useful and informative.
3. the INLA models are able to fully represent the true underlying conditions.
4. the costs and logistics of sampling are equal irrespective of location.

Contrary to the situation for the East Arm area, the conditioned latin hypercube sampling technique only outperformed the other techniques at very low sample sizes. After a sample size of approximately 30, the 2D spatially balanced design had better Minimum and Maximum Error. Also of interest is the finding that the multidimensional spatially balanced design was consistently worse than both a regular grid and 2D spatially balanced design and on par with a totally random design. This might suggest that there were fewer distinct patterns in the underlying sediment chemical data as observed in the Offset Outer Harbour sampling program.

Again, if however the purpose of the sampling design was to provide an unbiased representative sample of the general conditions across the spatial domain, then it could be argued that the 2D spatially balanced design was most appropriate - particularly if there was any doubt in the above assumptions.

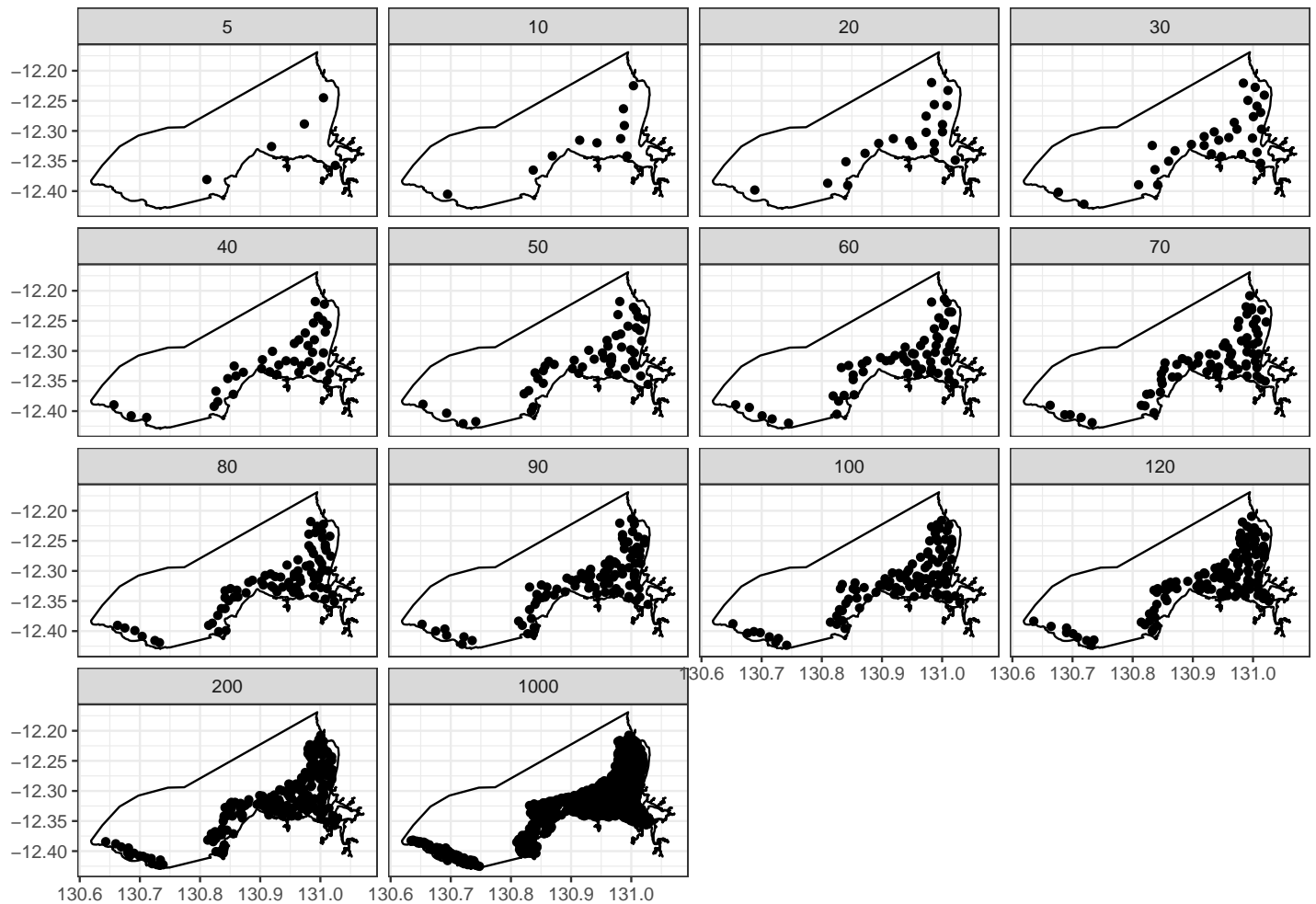


Figure 33: Sampling configurations associated with the lowest mean Error for each sample size for cLHS for the Outer Harbour

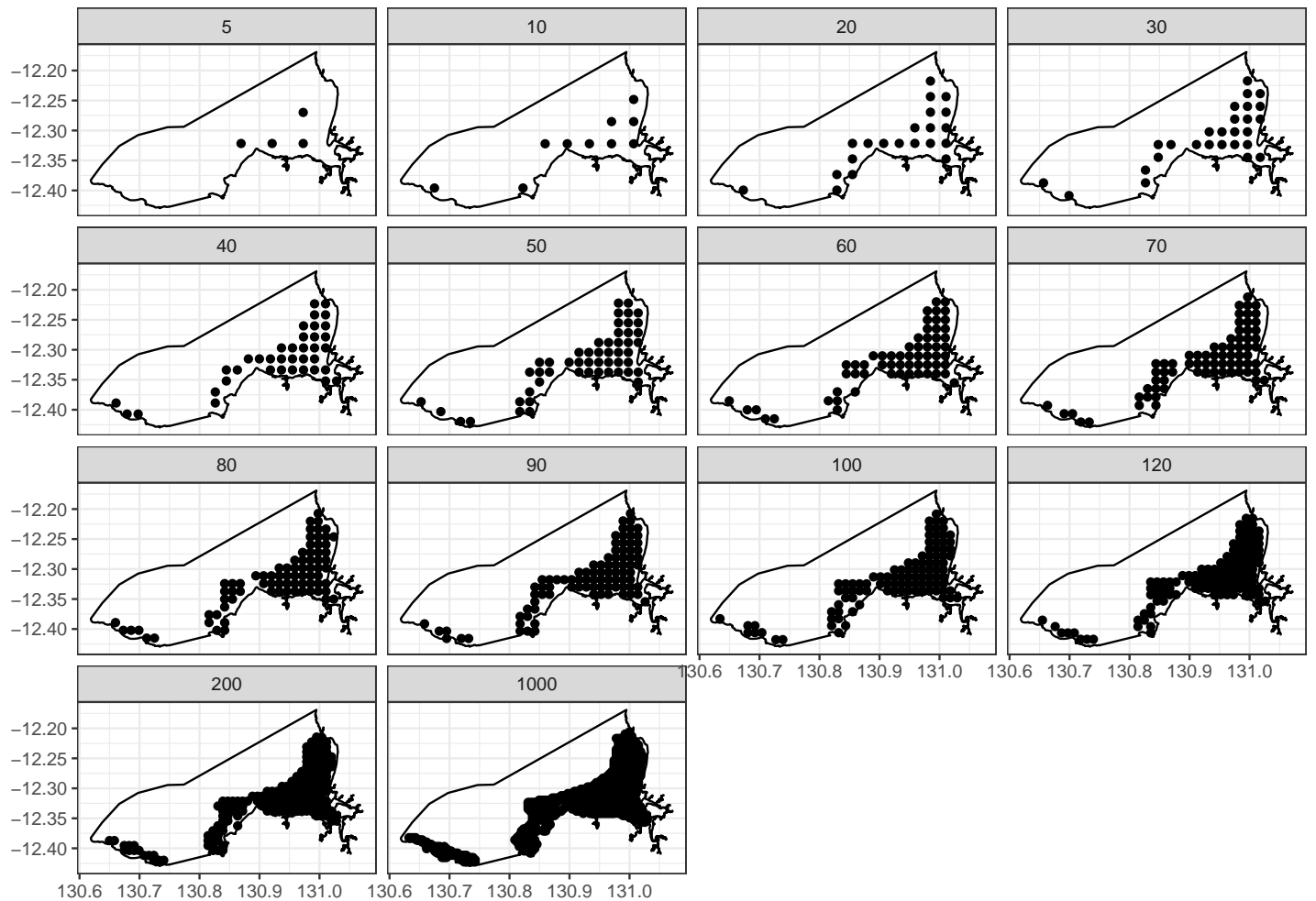


Figure 34: Sampling configurations associated with the lowest mean Error for each sample size for Regular grid sampling for the Outer Harbour

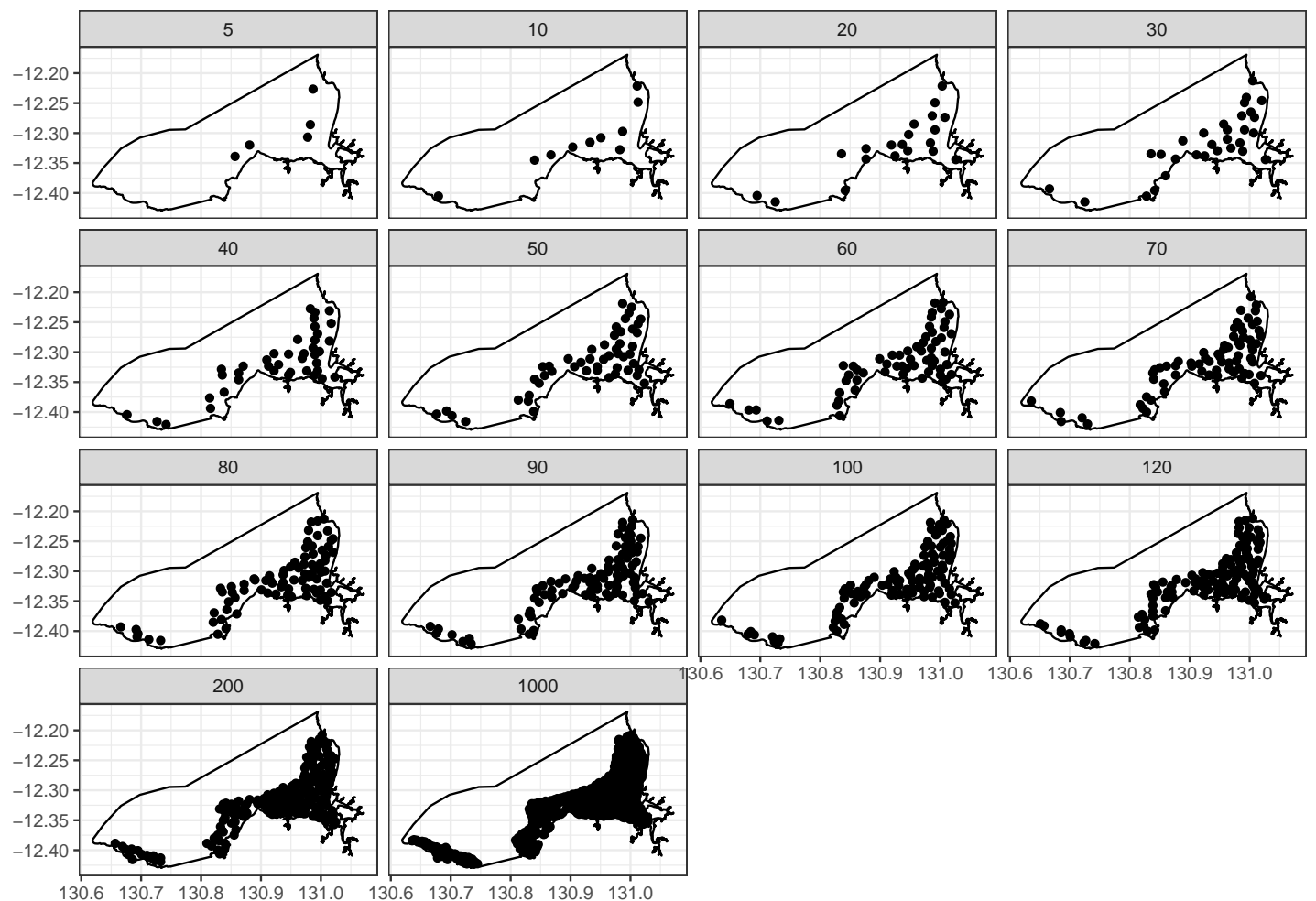


Figure 35: Sampling configurations associated with the lowest mean Error for each sample size for nD Spatially balanced sampling for the Outer Harbour

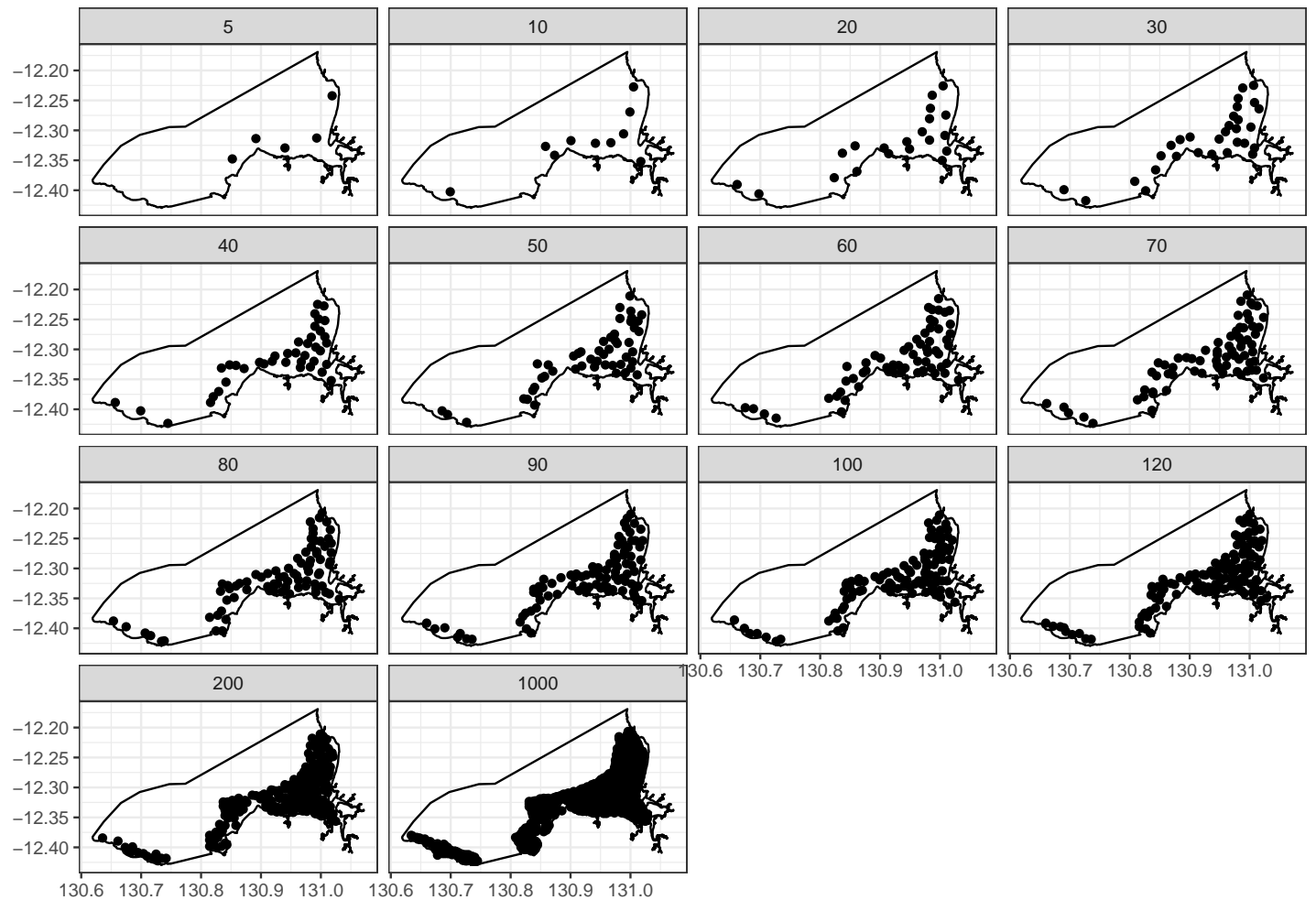


Figure 36: Sampling configurations associated with the lowest mean Error for each sample size for 2D Spatially balanced sampling for the Outer Harbour

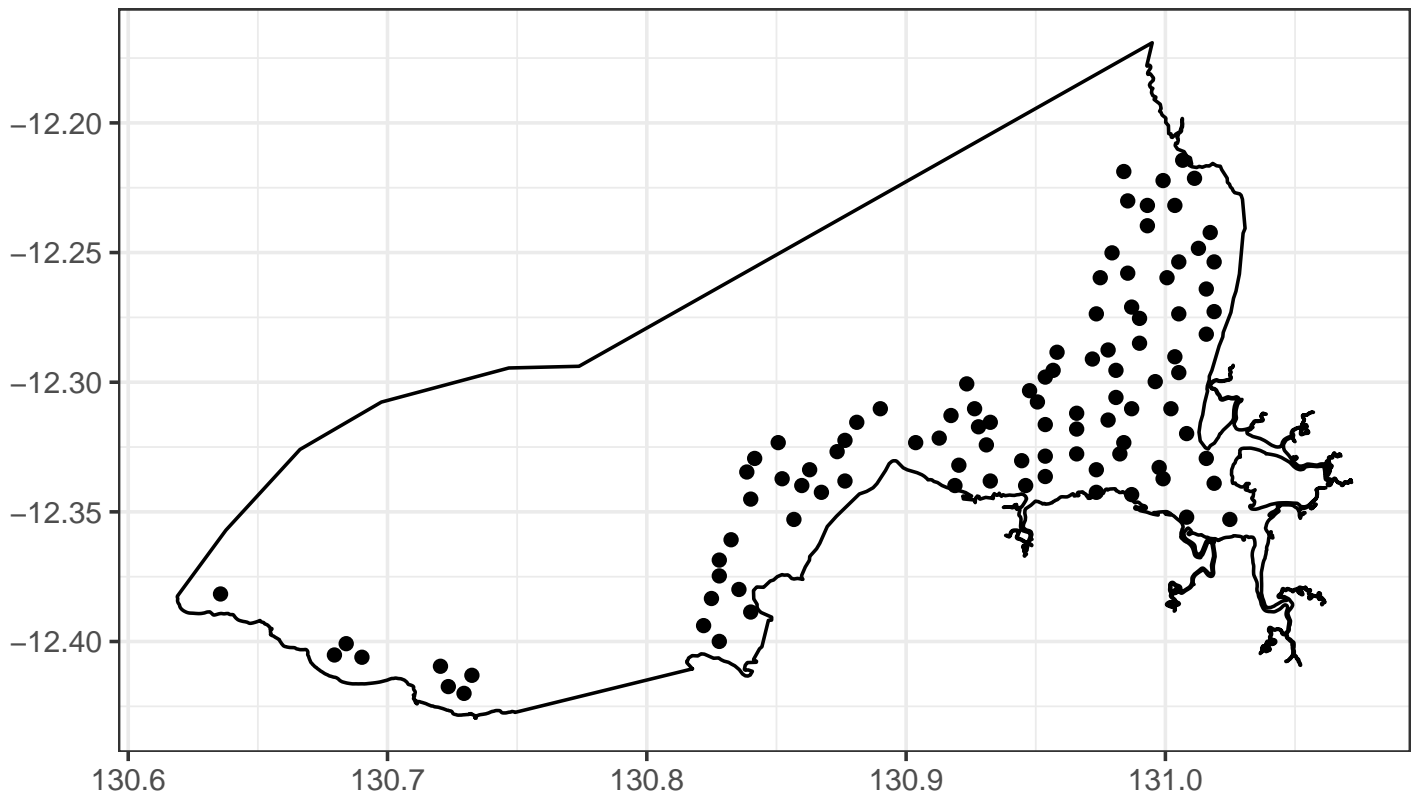


Figure 37: Two dimensional spatially balanced sampling configuration for the Outer Harbour (100 samples)

5. Conclusions

Overall, 2D spatially balanced sampling designs for both Outer Harbour and East Arm would seem most appropriate. These designs are immune to any uncertainty in previous data and spatial modelling and should yield well balanced spatial configurations. A total of 100 samples collected from both East Arm and Outer Harbour was likely to yield representative samples from which to construct a variety of spatio-temporal models into the future.

6. Appendix A

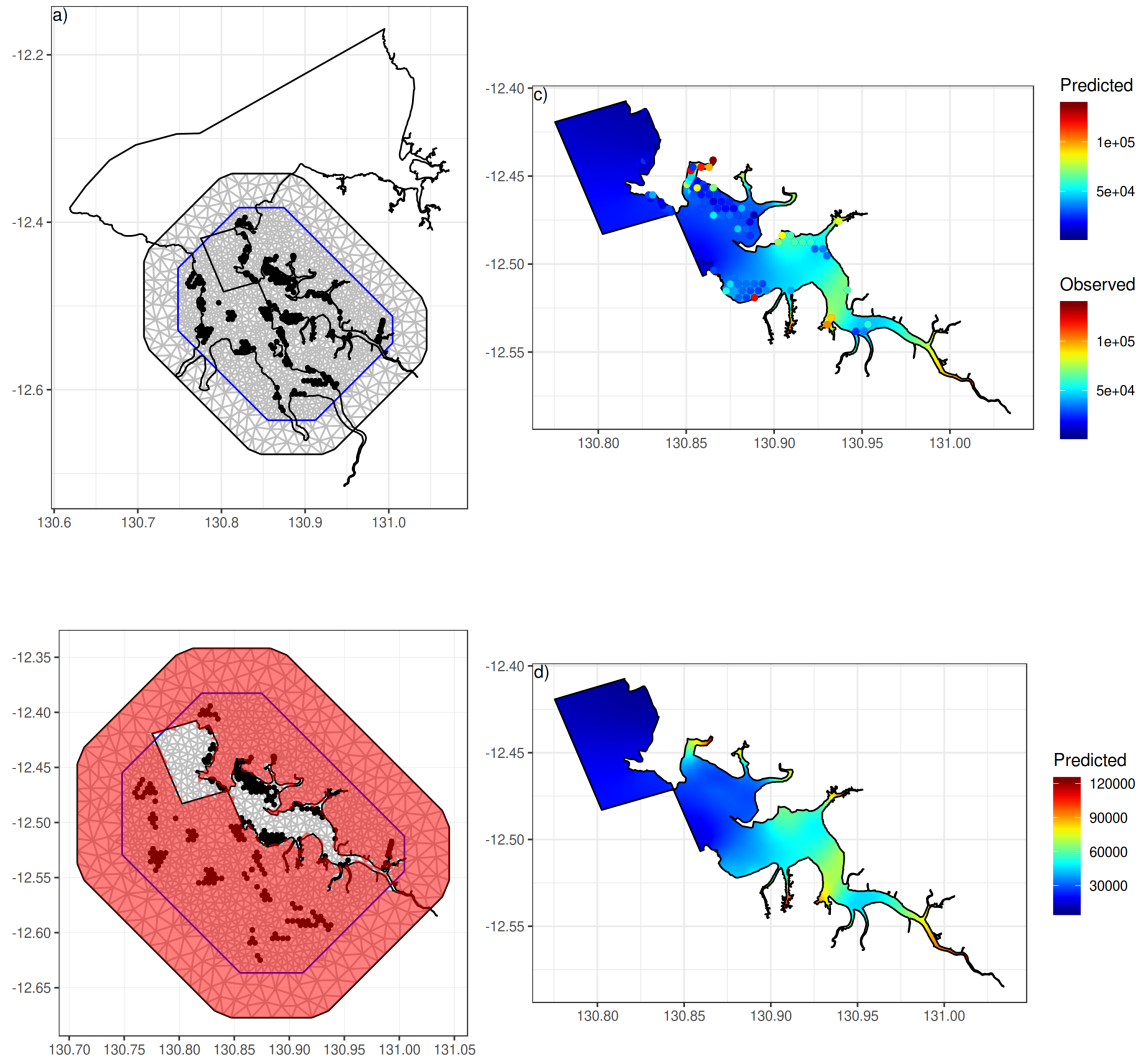


Figure 38: Integrated Nested Laplace Approximation (INLA) barrier spatial modelling of Aluminium. The diagram illustrates a) the mesh, b) the barrier mask, c) the resulting predicted 2D surface (and observed training data as points) and d) the resulting predicted 2D surface scaled to the range of predictions.

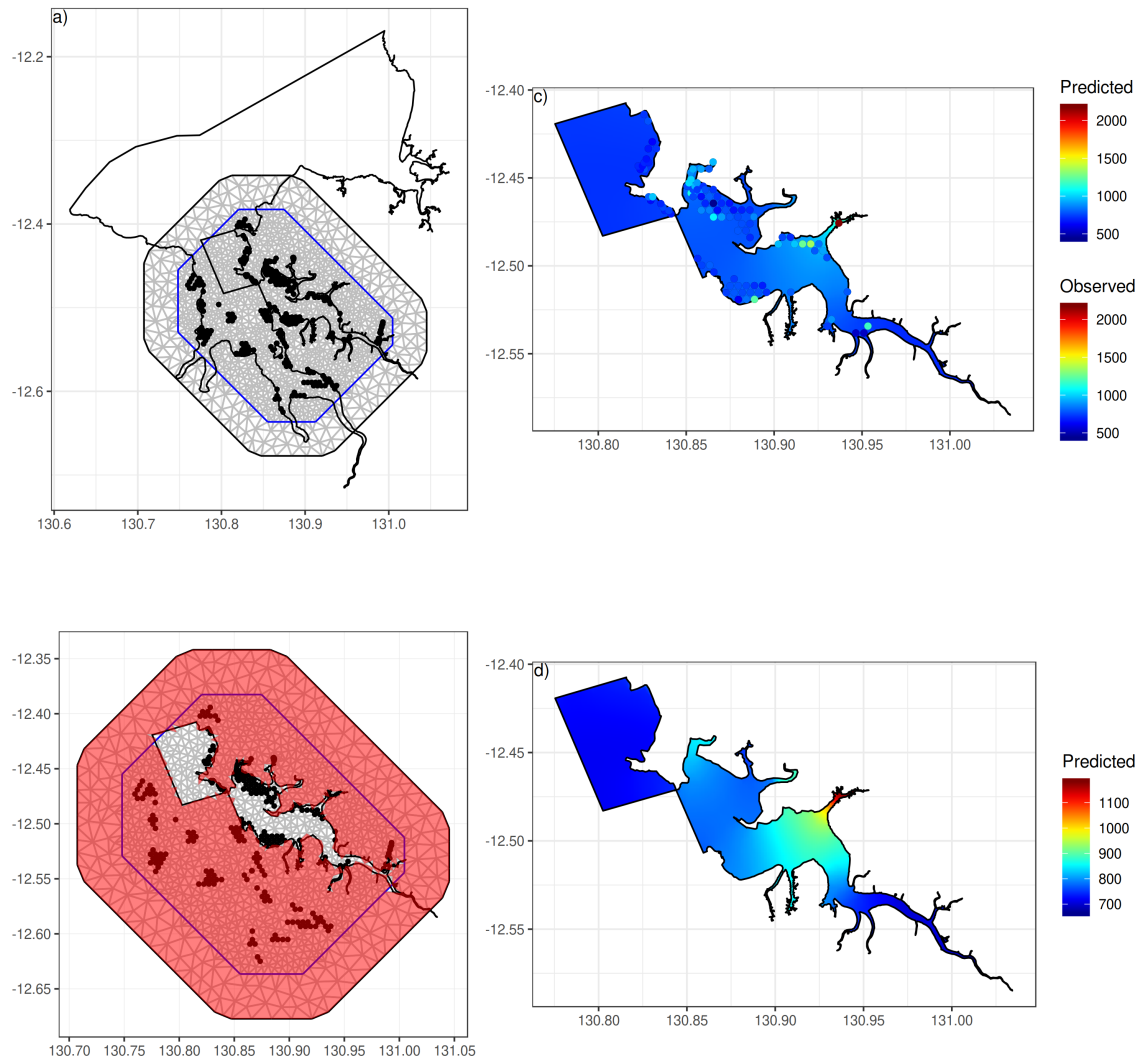


Figure 39: *Integrated Nested Laplace Approximation (INLA) barrier spatial modelling of Phosphorus.* The diagram illustrates a) the mesh, b) the barrier mask, c) the resulting predicted 2D surface (and observed training data as points) and d) the resulting predicted 2D surface scaled to the range of predictions.

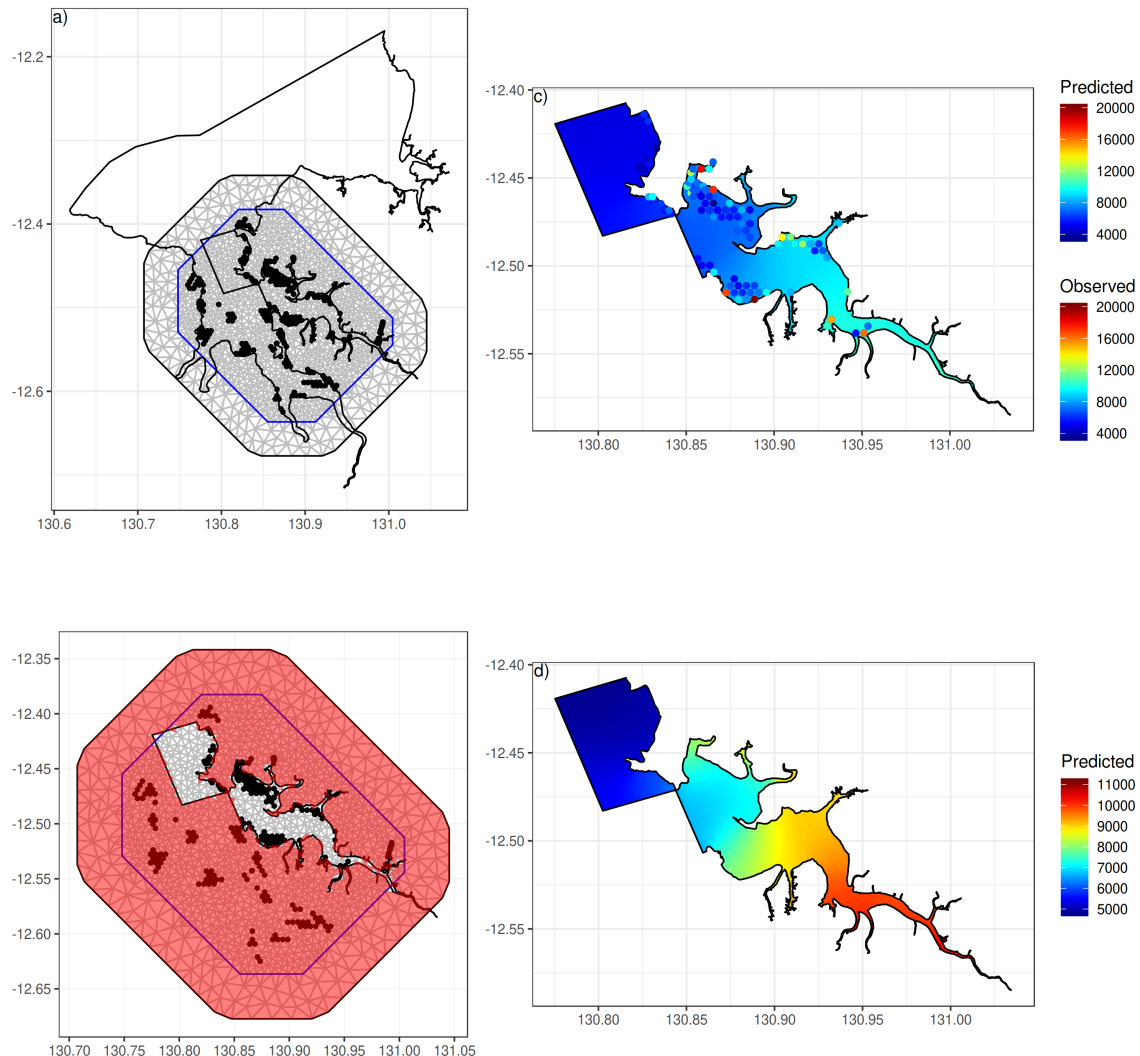


Figure 40: *Integrated Nested Laplace Approximation (INLA) barrier spatial modelling of Sulfur.* The diagram illustrates a) the mesh, b) the barrier mask, c) the resulting predicted 2D surface (and observed training data as points) and d) the resulting predicted 2D surface scaled to the range of predictions.

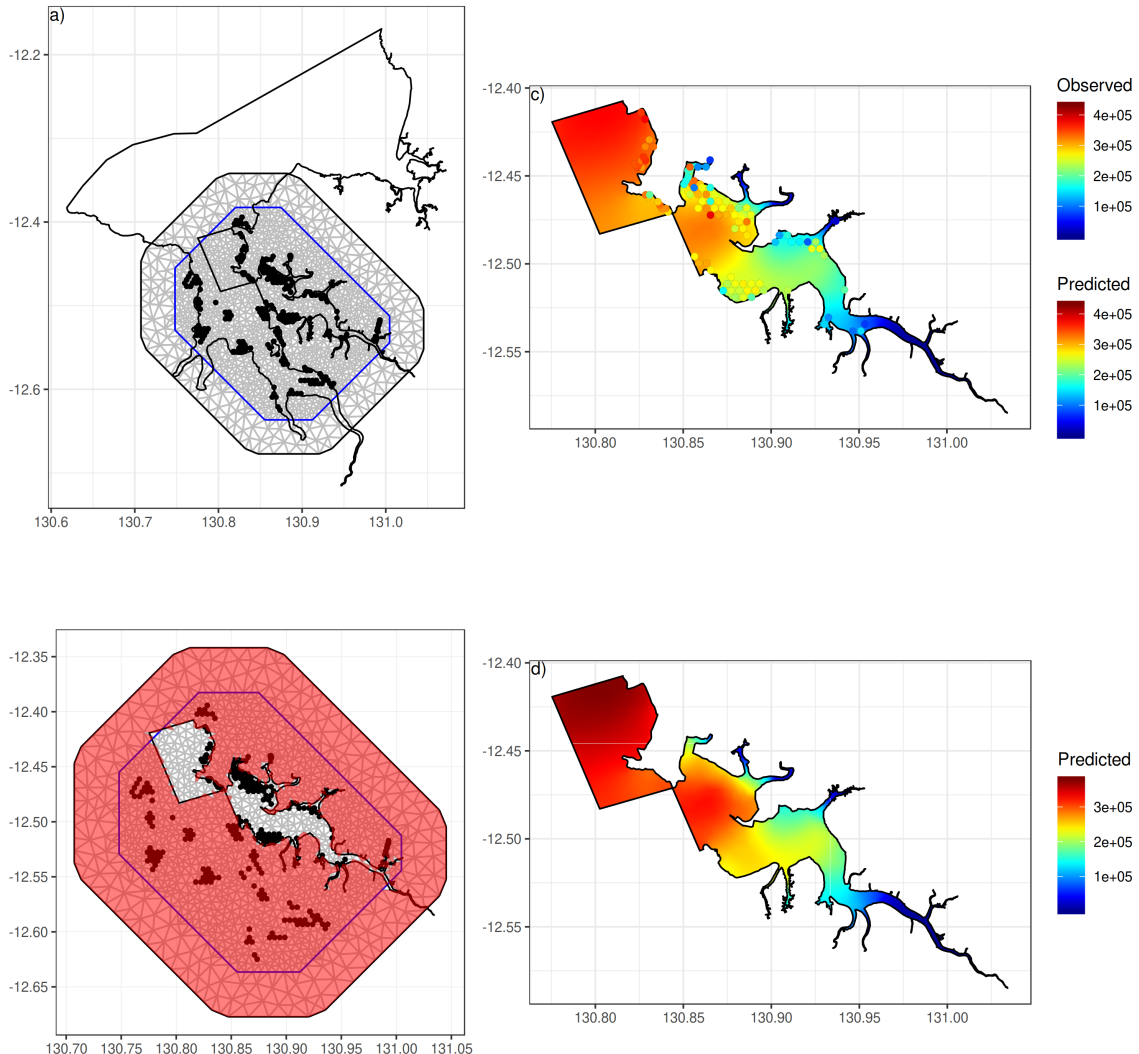


Figure 41: Integrated Nested Laplace Approximation (INLA) barrier spatial modelling of Calcium. The diagram illustrates a) the mesh, b) the barrier mask, c) the resulting predicted 2D surface (and observed training data as points) and d) the resulting predicted 2D surface scaled to the range of predictions.

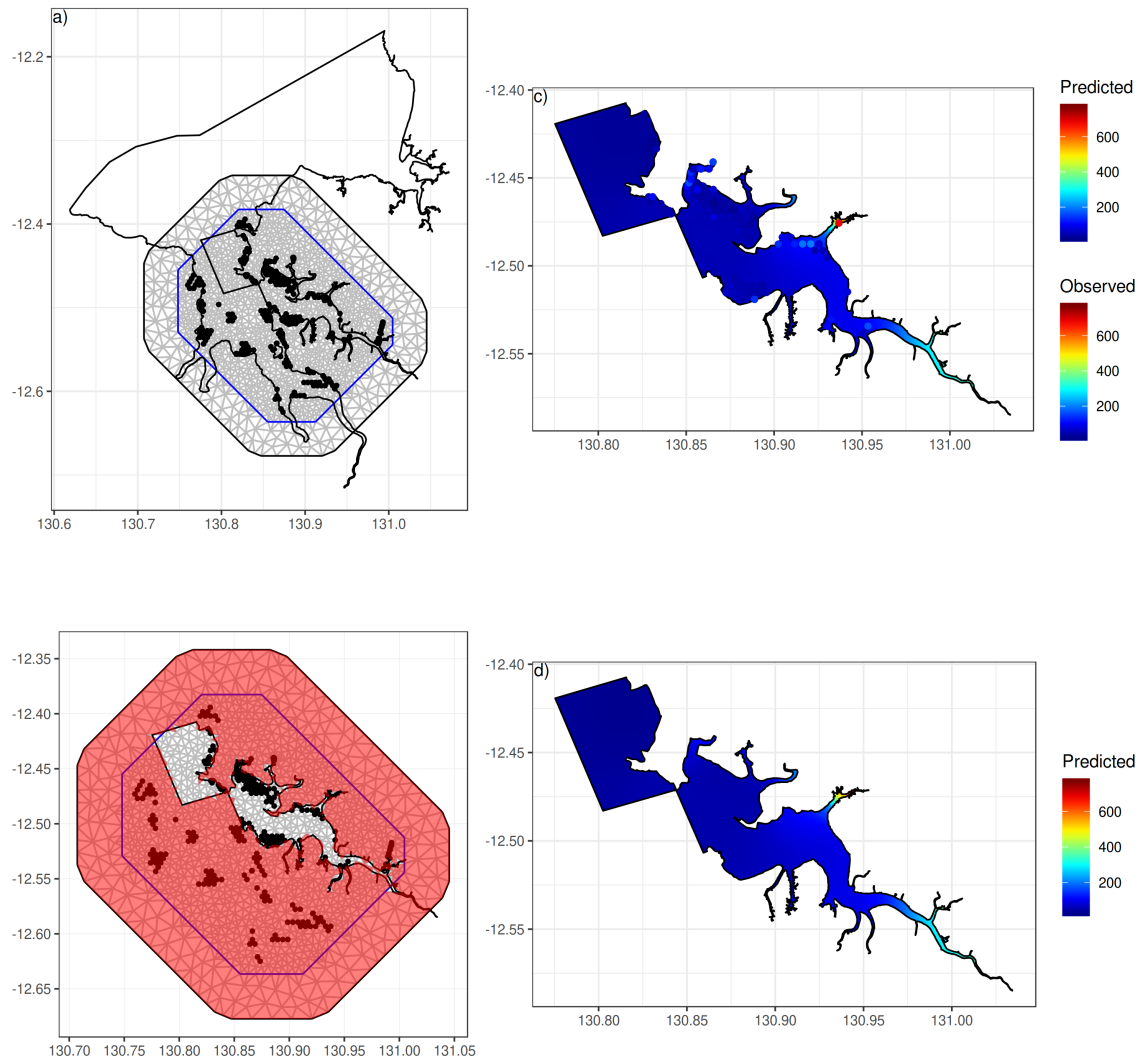


Figure 42: *Integrated Nested Laplace Approximation (INLA) barrier spatial modelling of Vanadium. The diagram illustrates a) the mesh, b) the barrier mask, c) the resulting predicted 2D surface (and observed training data as points) and d) the resulting predicted 2D surface scaled to the range of predictions.*

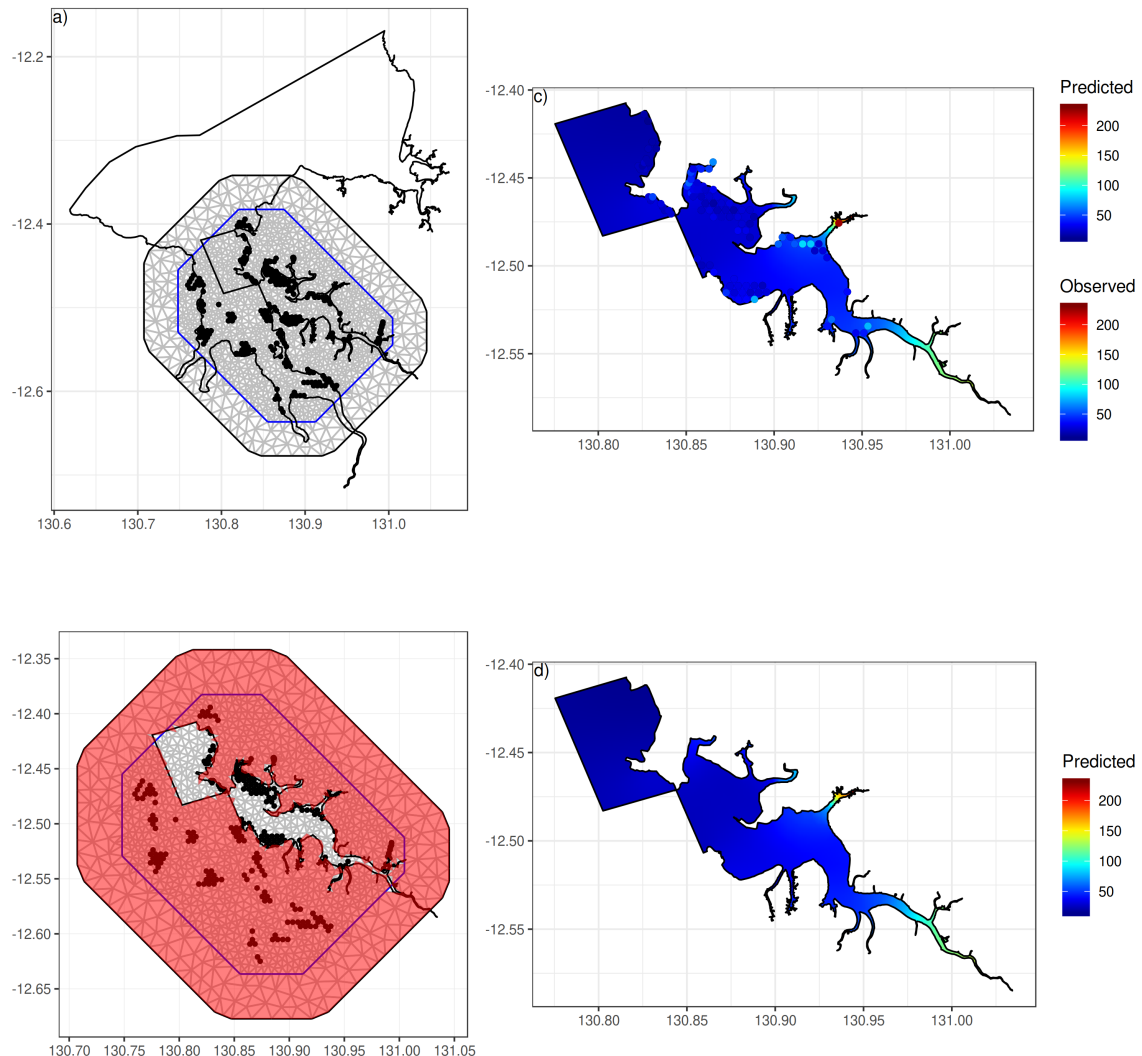


Figure 43: *Integrated Nested Laplace Approximation (INLA) barrier spatial modelling of Chromium. The diagram illustrates a) the mesh, b) the barrier mask, c) the resulting predicted 2D surface (and observed training data as points) and d) the resulting predicted 2D surface scaled to the range of predictions.*

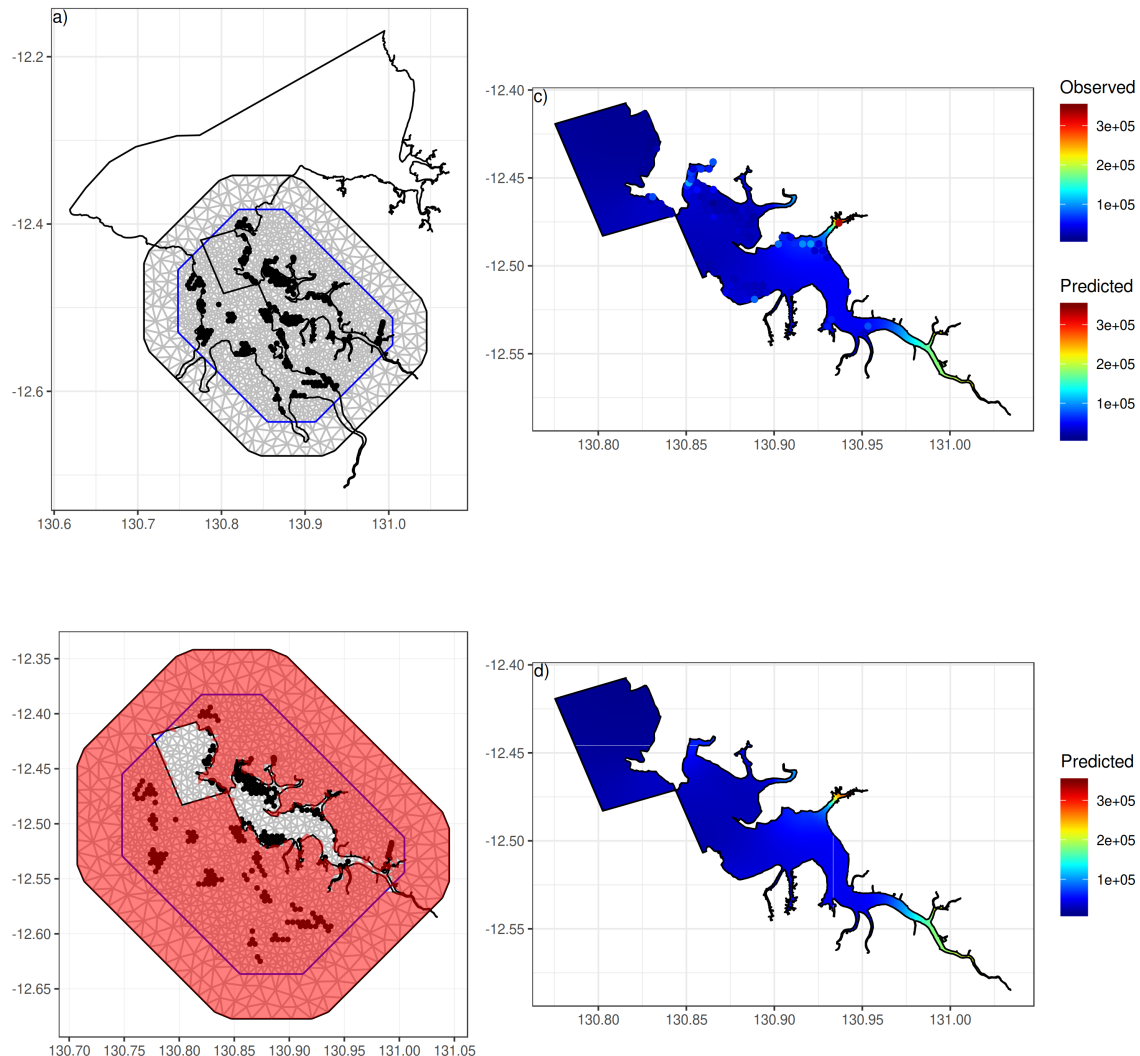


Figure 44: *Integrated Nested Laplace Approximation (INLA) barrier spatial modelling of Iron.* The diagram illustrates a) the mesh, b) the barrier mask, c) the resulting predicted 2D surface (and observed training data as points) and d) the resulting predicted 2D surface scaled to the range of predictions.

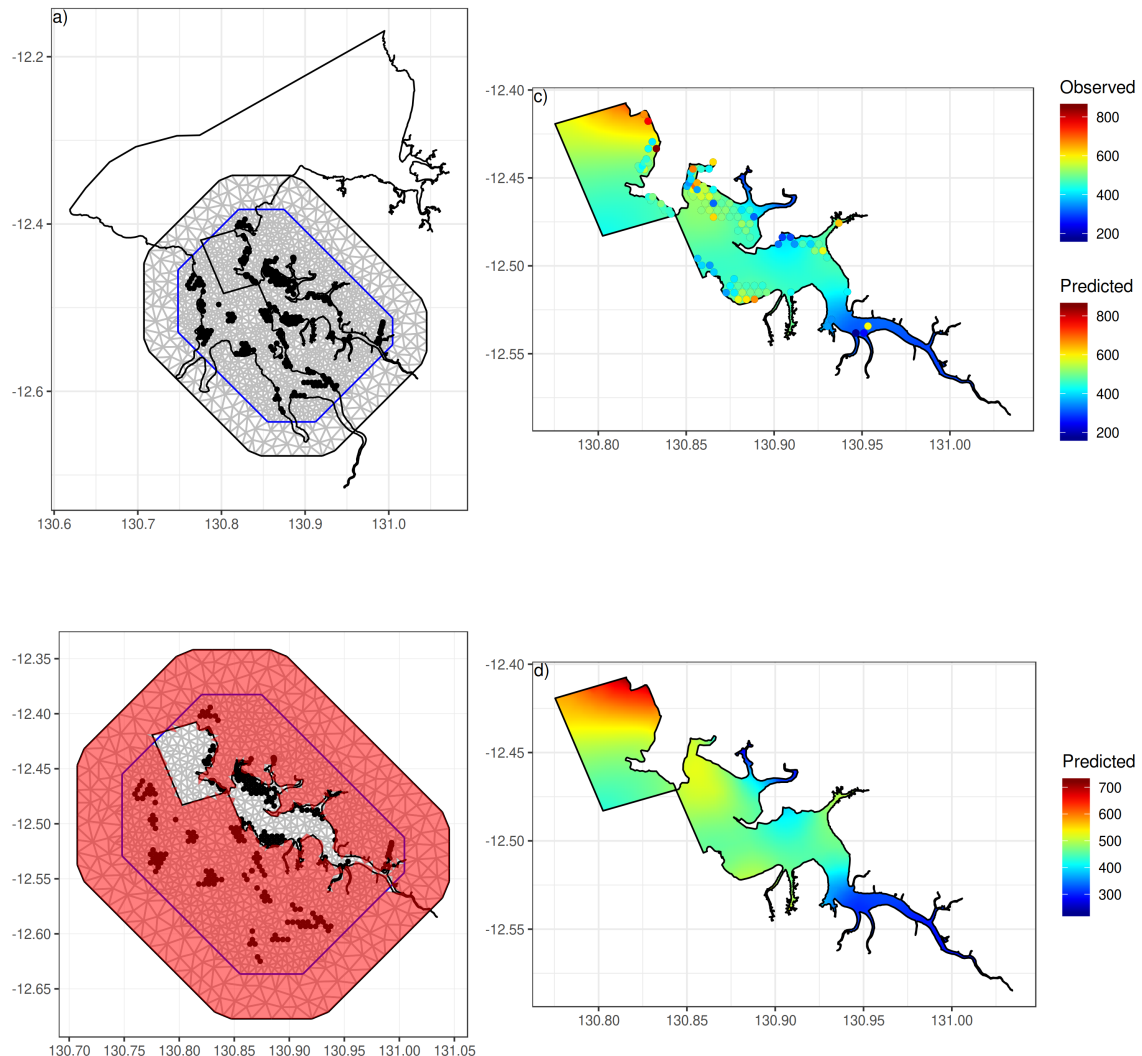


Figure 45: *Integrated Nested Laplace Approximation (INLA) barrier spatial modelling of Manganese. The diagram illustrates a) the mesh, b) the barrier mask, c) the resulting predicted 2D surface (and observed training data as points) and d) the resulting predicted 2D surface scaled to the range of predictions.*

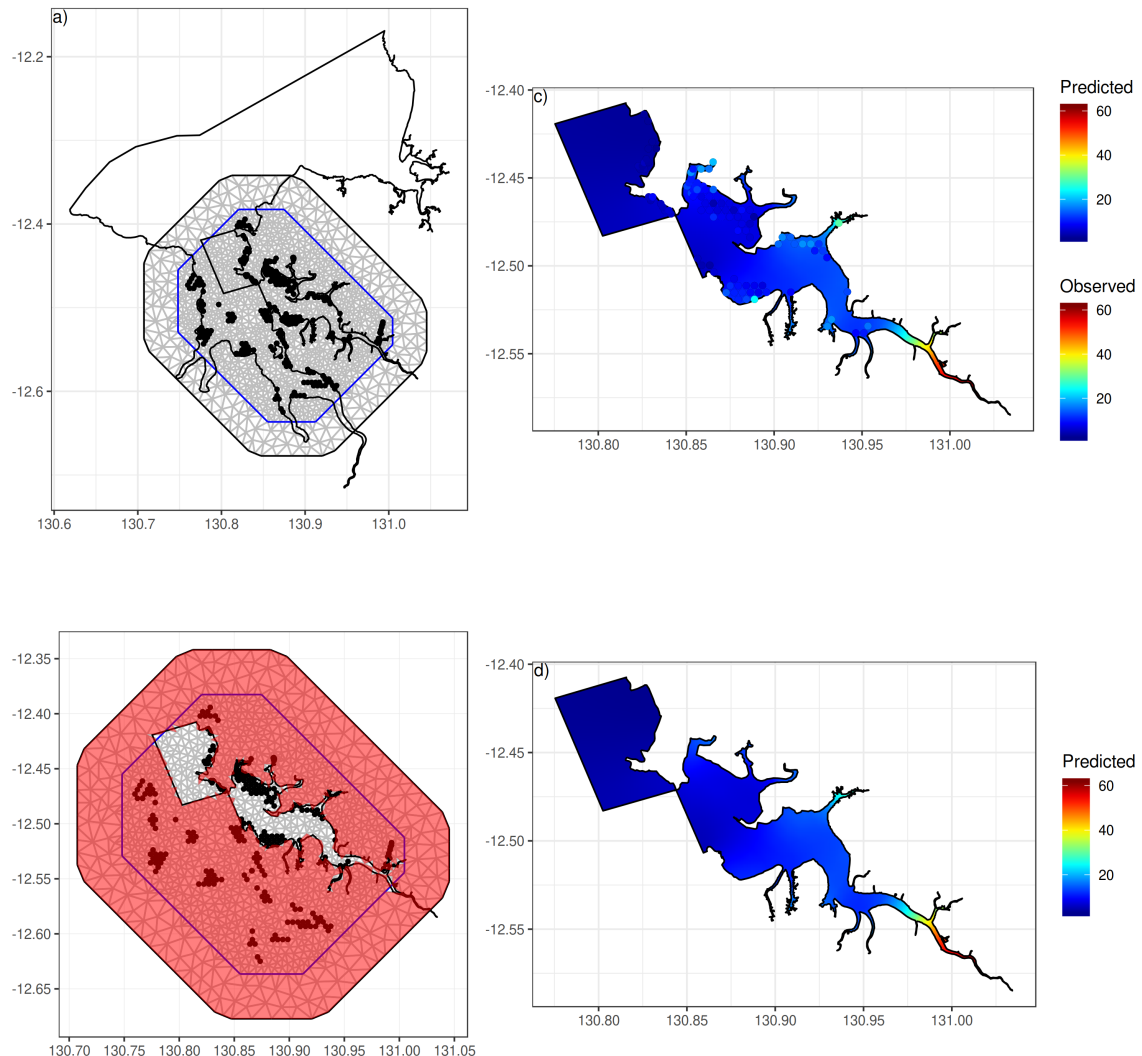


Figure 46: *Integrated Nested Laplace Approximation (INLA) barrier spatial modelling of Cobult. The diagram illustrates a) the mesh, b) the barrier mask, c) the resulting predicted 2D surface (and observed training data as points) and d) the resulting predicted 2D surface scaled to the range of predictions.*

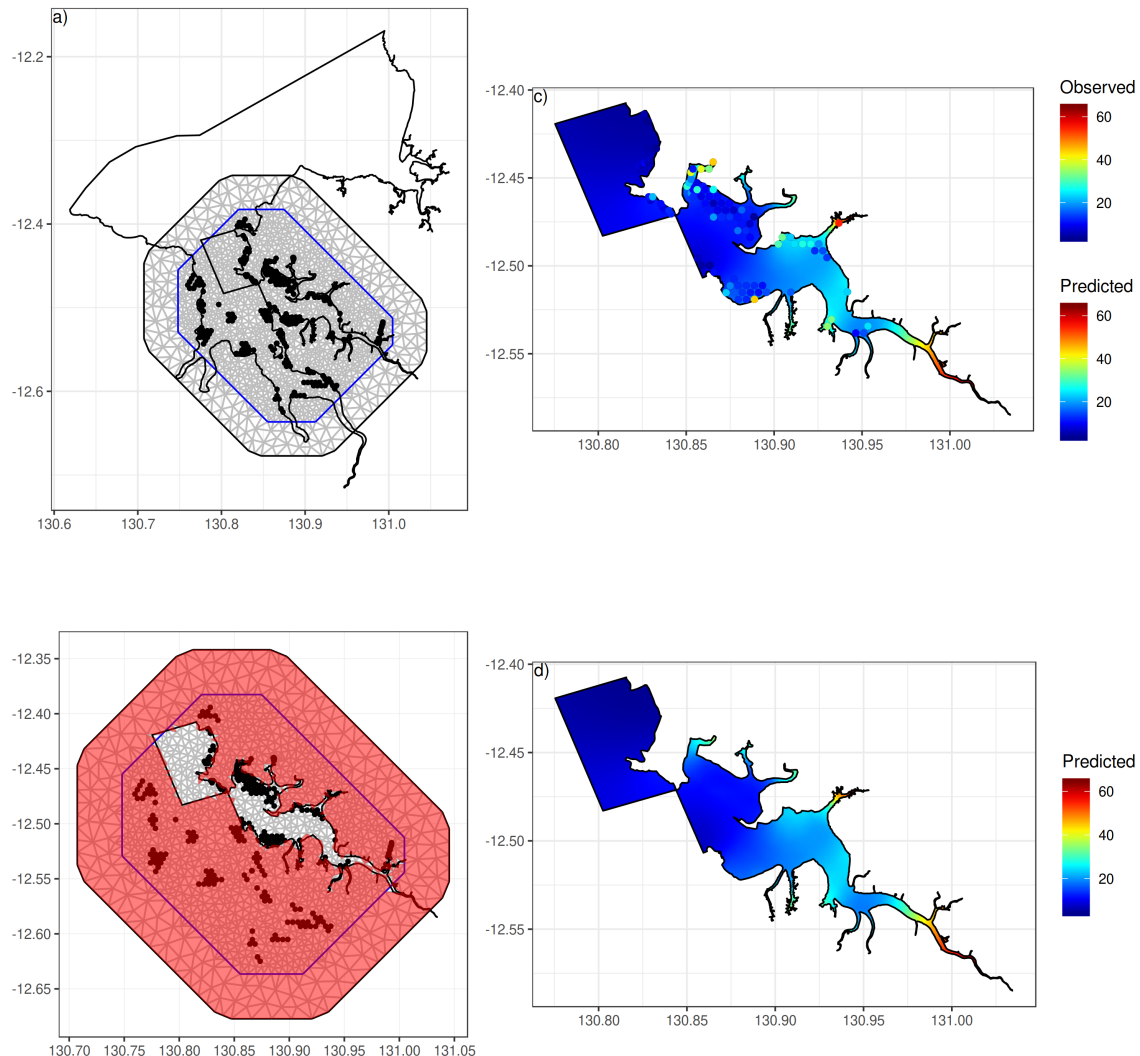


Figure 47: *Integrated Nested Laplace Approximation (INLA) barrier spatial modelling of Nickel. The diagram illustrates a) the mesh, b) the barrier mask, c) the resulting predicted 2D surface (and observed training data as points) and d) the resulting predicted 2D surface scaled to the range of predictions.*

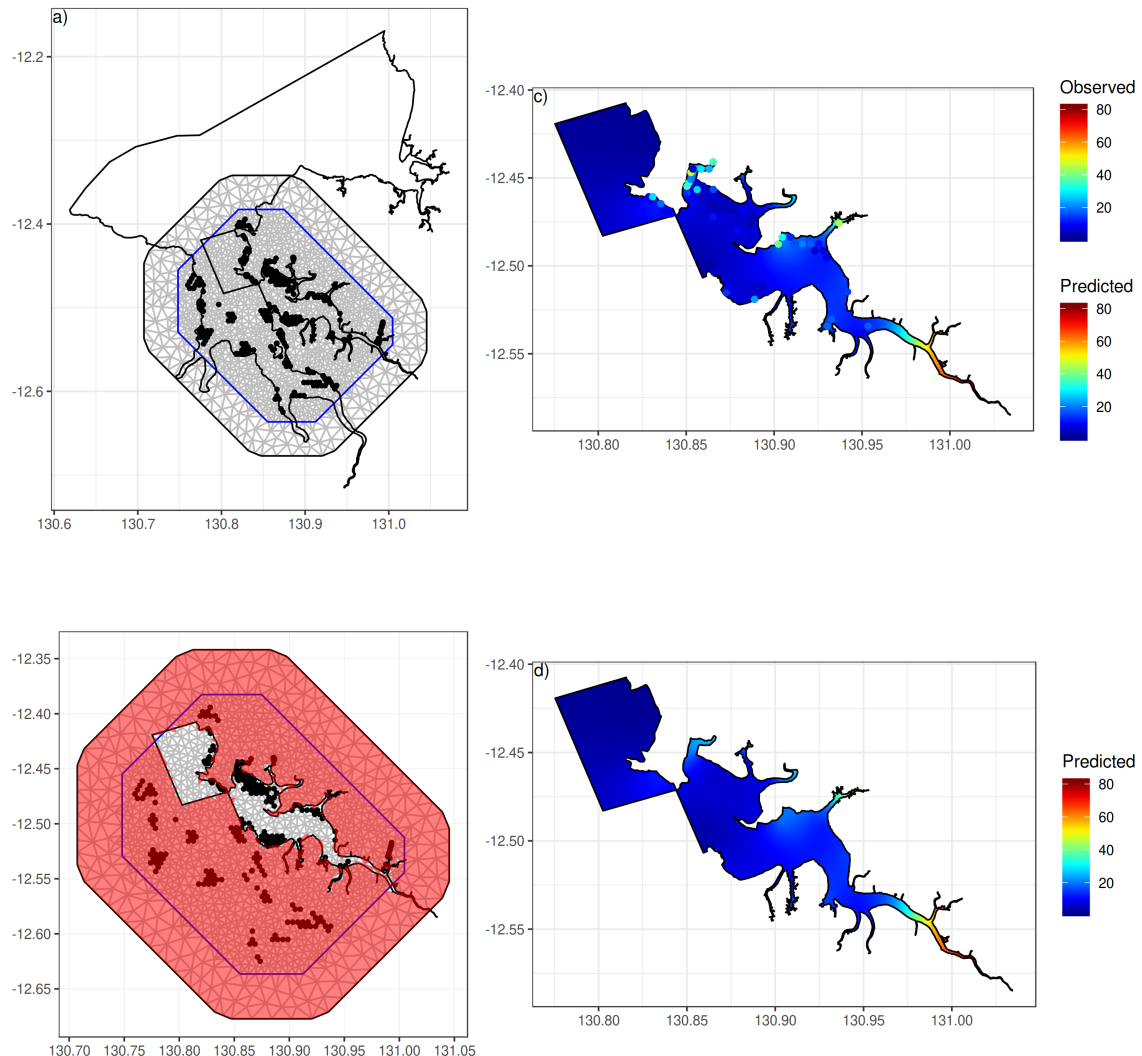


Figure 48: Integrated Nested Laplace Approximation (INLA) barrier spatial modelling of Copper. The diagram illustrates a) the mesh, b) the barrier mask, c) the resulting predicted 2D surface (and observed training data as points) and d) the resulting predicted 2D surface scaled to the range of predictions.

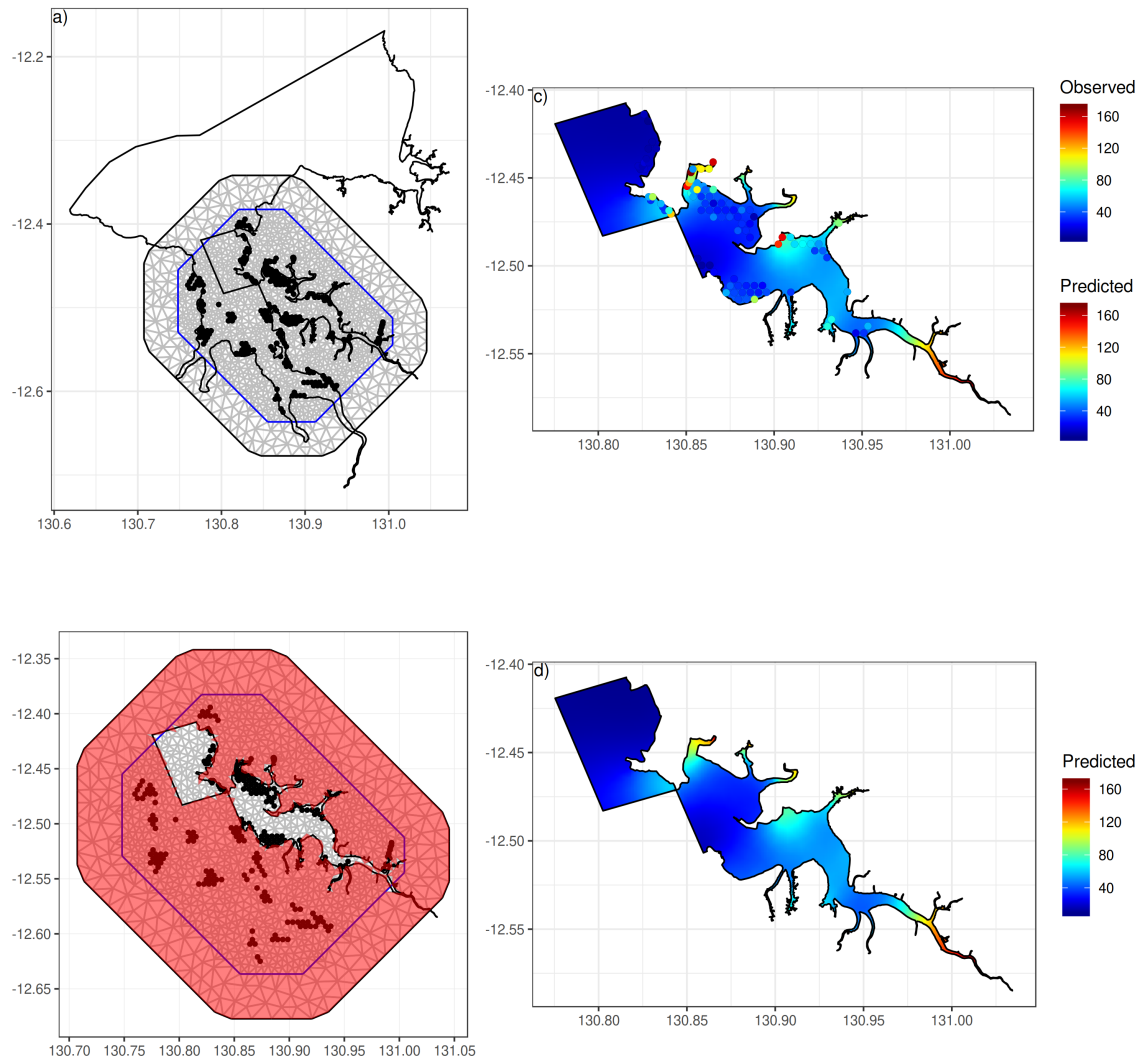


Figure 49: *Integrated Nested Laplace Approximation (INLA) barrier spatial modelling of Zinc. The diagram illustrates a) the mesh, b) the barrier mask, c) the resulting predicted 2D surface (and observed training data as points) and d) the resulting predicted 2D surface scaled to the range of predictions.*

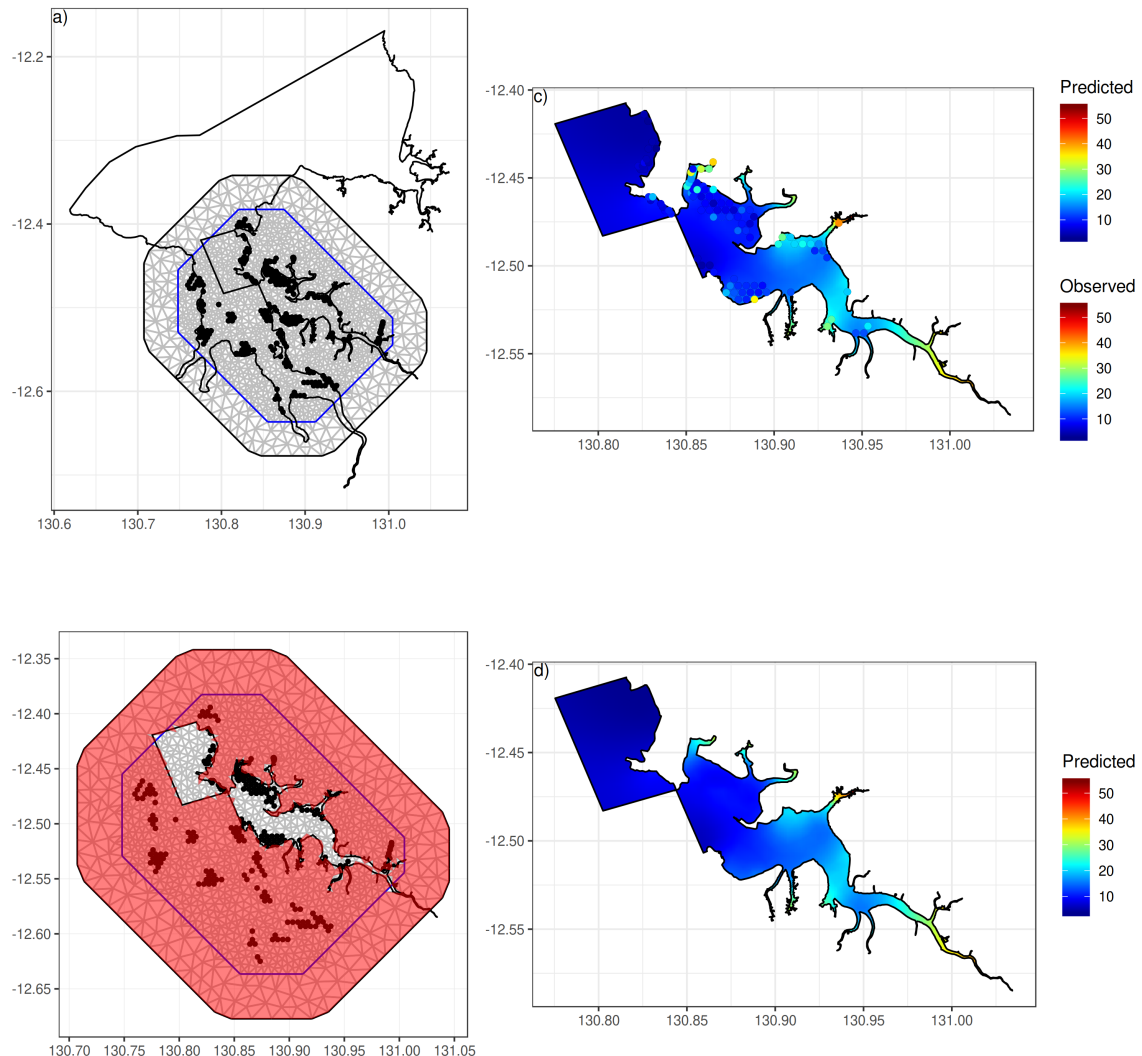


Figure 50: *Integrated Nested Laplace Approximation (INLA) barrier spatial modelling of Gallium.* The diagram illustrates a) the mesh, b) the barrier mask, c) the resulting predicted 2D surface (and observed training data as points) and d) the resulting predicted 2D surface scaled to the range of predictions.

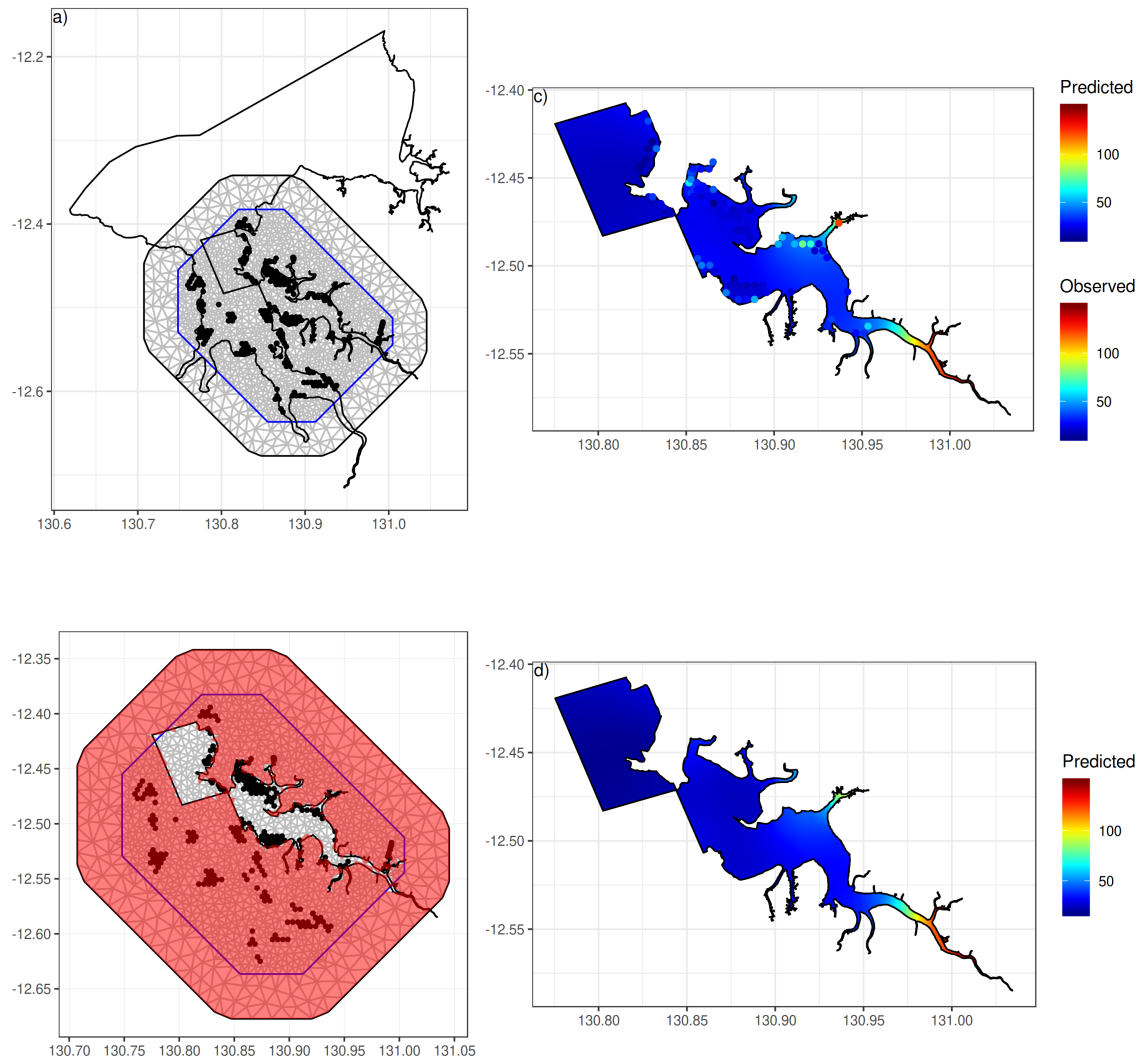


Figure 51: Integrated Nested Laplace Approximation (INLA) barrier spatial modelling of Arsenic. The diagram illustrates a) the mesh, b) the barrier mask, c) the resulting predicted 2D surface (and observed training data as points) and d) the resulting predicted 2D surface scaled to the range of predictions.

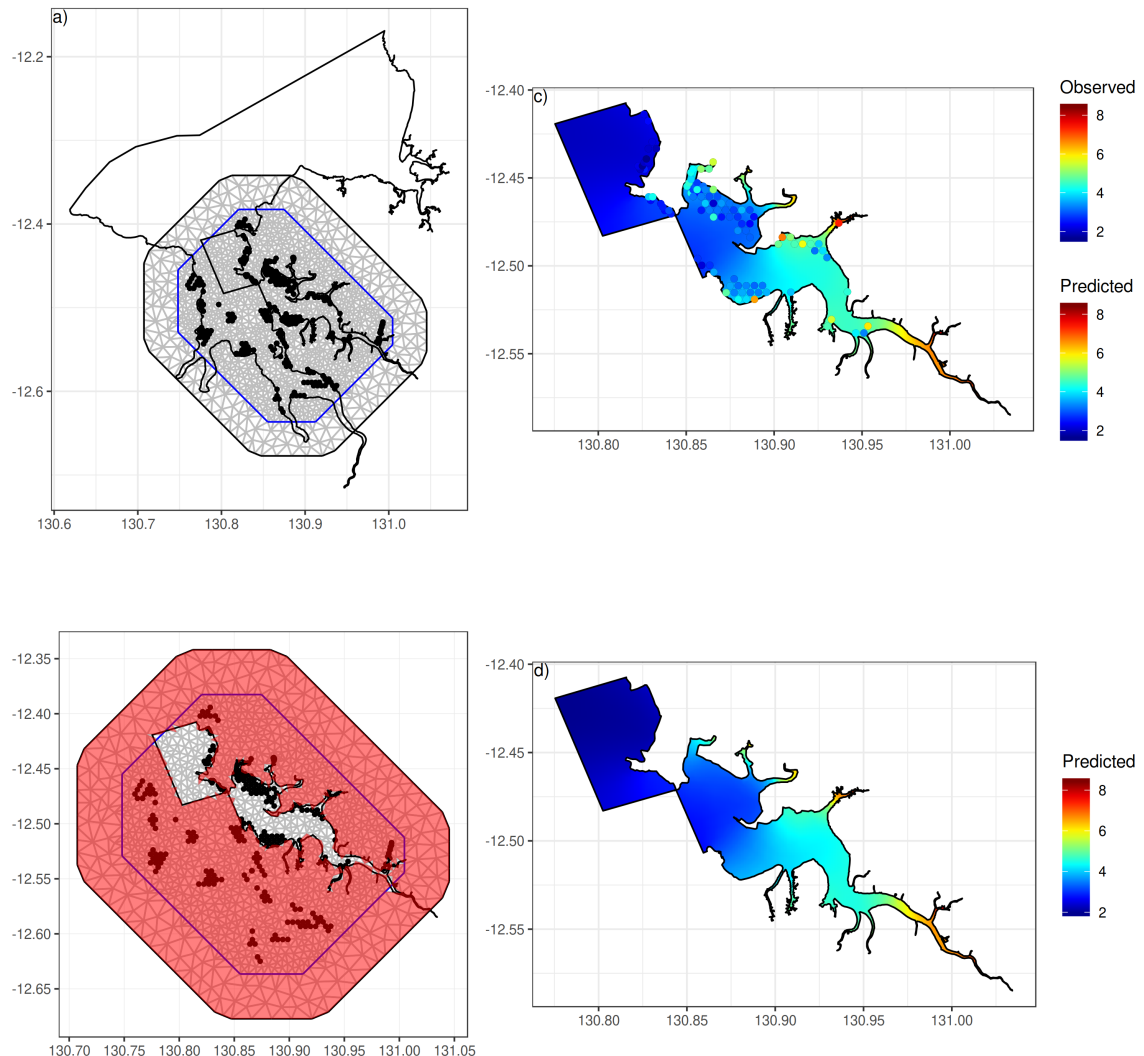


Figure 52: *Integrated Nested Laplace Approximation (INLA) barrier spatial modelling of Selenium. The diagram illustrates a) the mesh, b) the barrier mask, c) the resulting predicted 2D surface (and observed training data as points) and d) the resulting predicted 2D surface scaled to the range of predictions.*

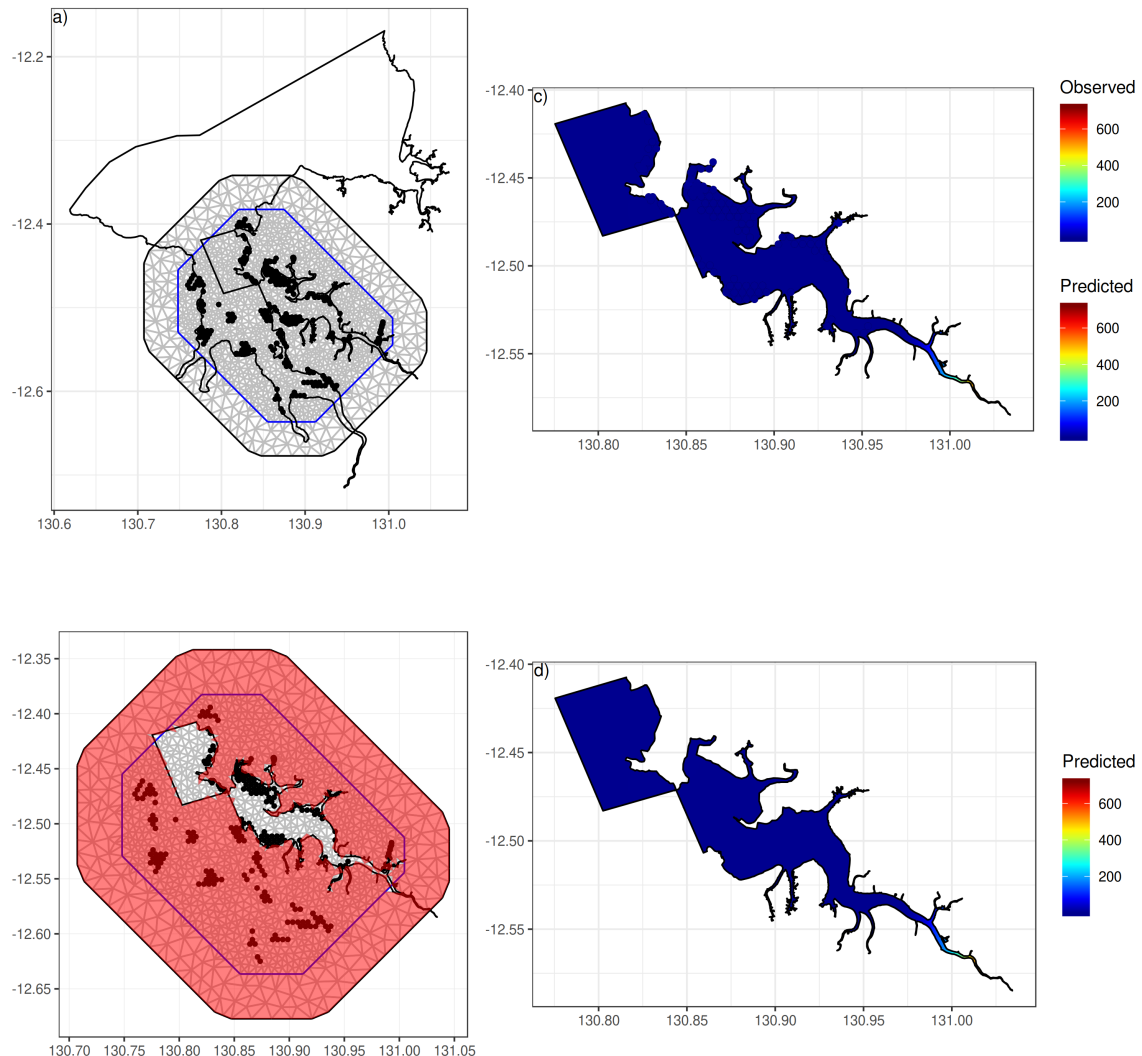


Figure 53: *Integrated Nested Laplace Approximation (INLA) barrier spatial modelling of Molybdenum.* The diagram illustrates a) the mesh, b) the barrier mask, c) the resulting predicted 2D surface (and observed training data as points) and d) the resulting predicted 2D surface scaled to the range of predictions.

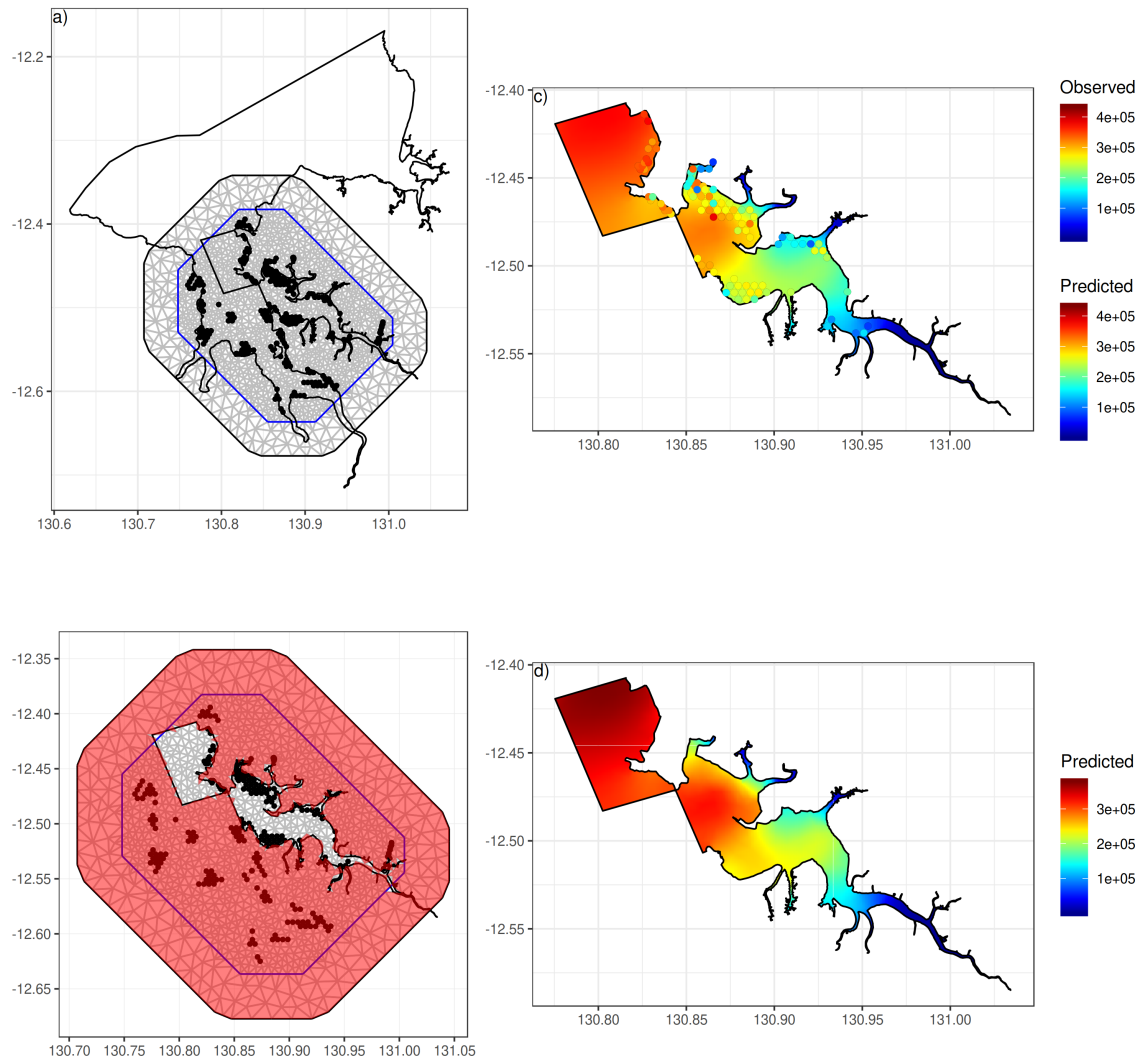


Figure 54: *Integrated Nested Laplace Approximation (INLA) barrier spatial modelling of Cadmium. The diagram illustrates a) the mesh, b) the barrier mask, c) the resulting predicted 2D surface (and observed training data as points) and d) the resulting predicted 2D surface scaled to the range of predictions.*

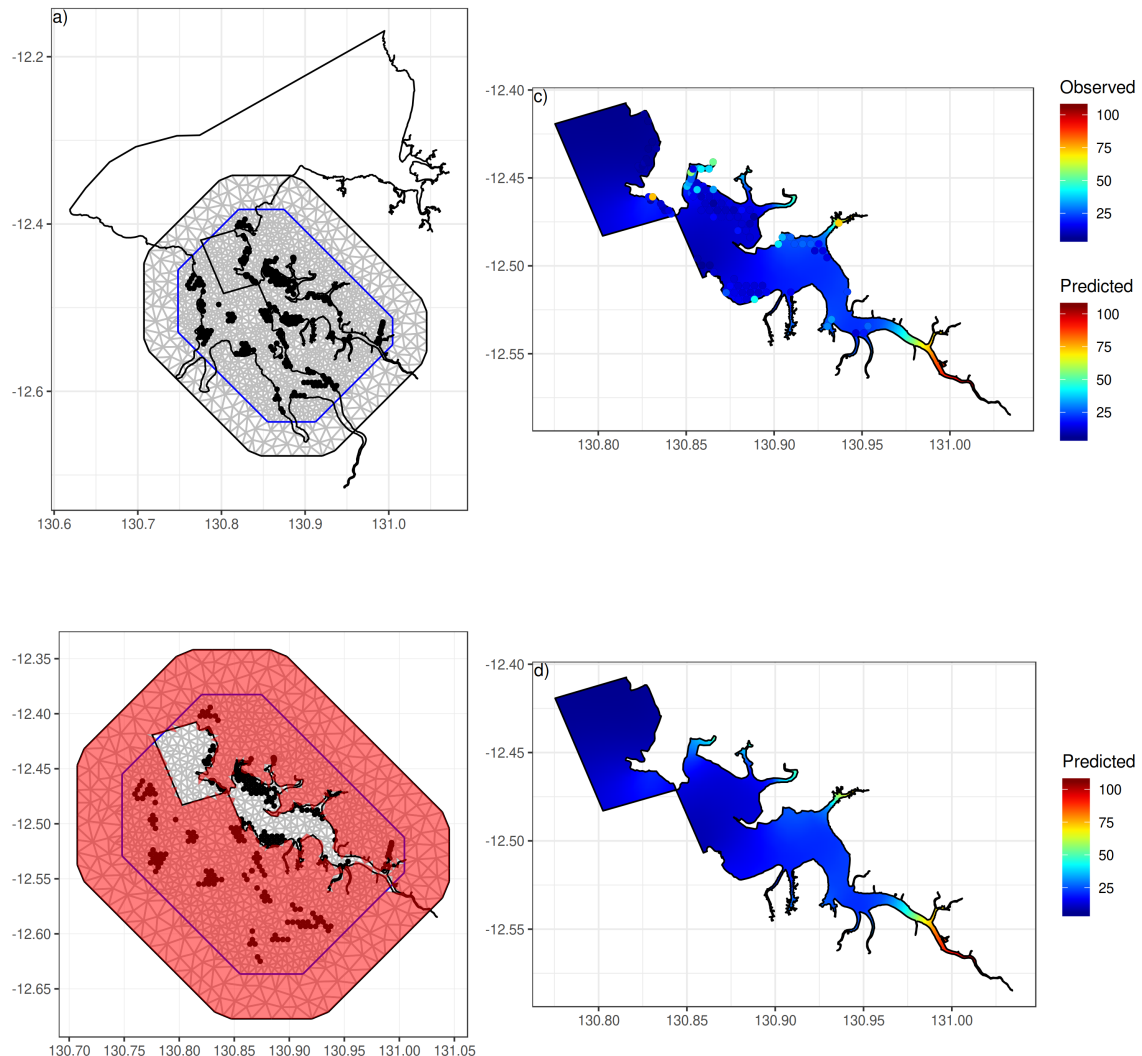


Figure 55: *Integrated Nested Laplace Approximation (INLA) barrier spatial modelling of Lead. The diagram illustrates a) the mesh, b) the barrier mask, c) the resulting predicted 2D surface (and observed training data as points) and d) the resulting predicted 2D surface scaled to the range of predictions.*

7. Appendix B

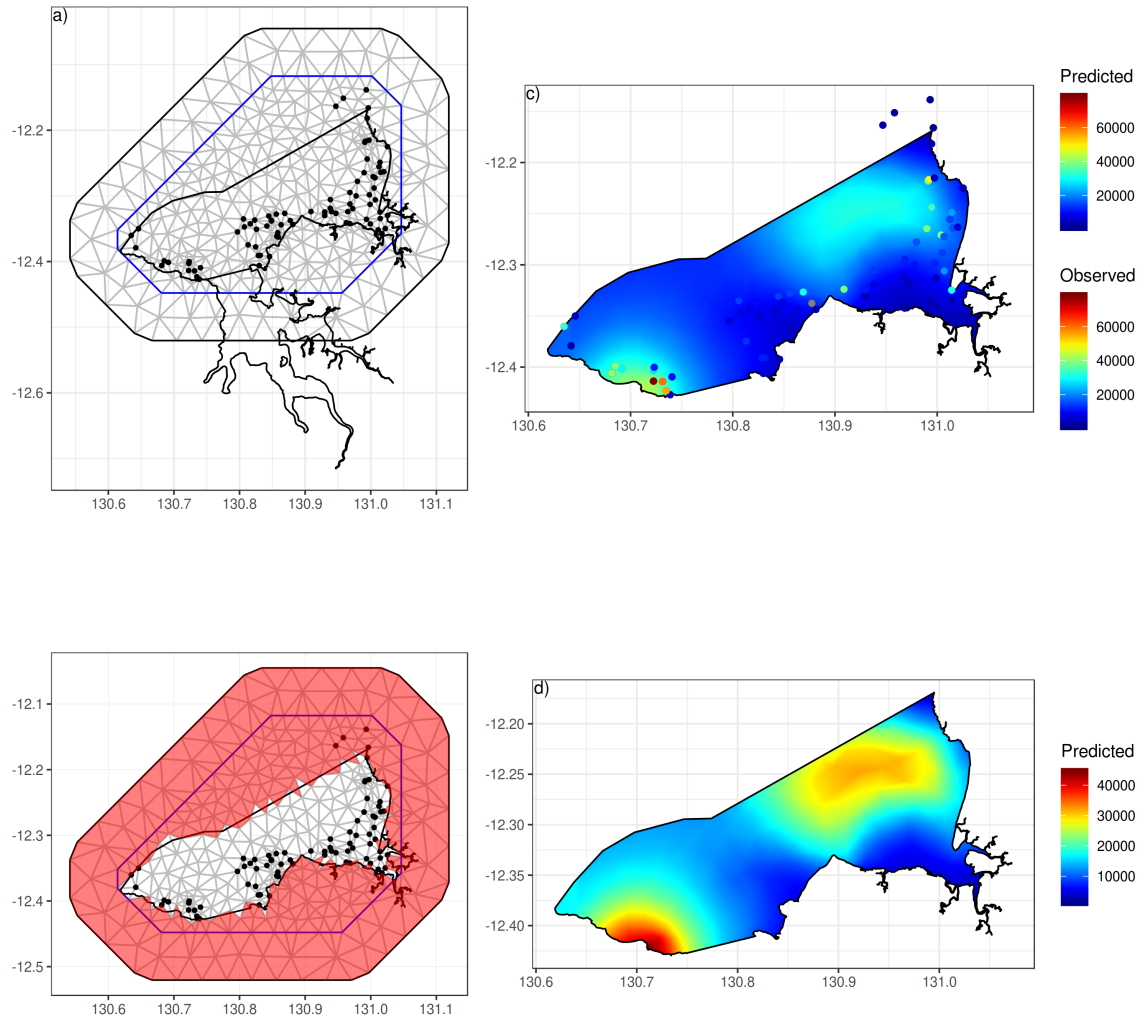


Figure 56: Integrated Nested Laplace Approximation (INLA) barrier spatial modelling of Aluminium. The diagram illustrates a) the mesh, b) the barrier mask, c) the resulting predicted 2D surface (and observed training data as points) and d) the resulting predicted 2D surface scaled to the range of predictions.

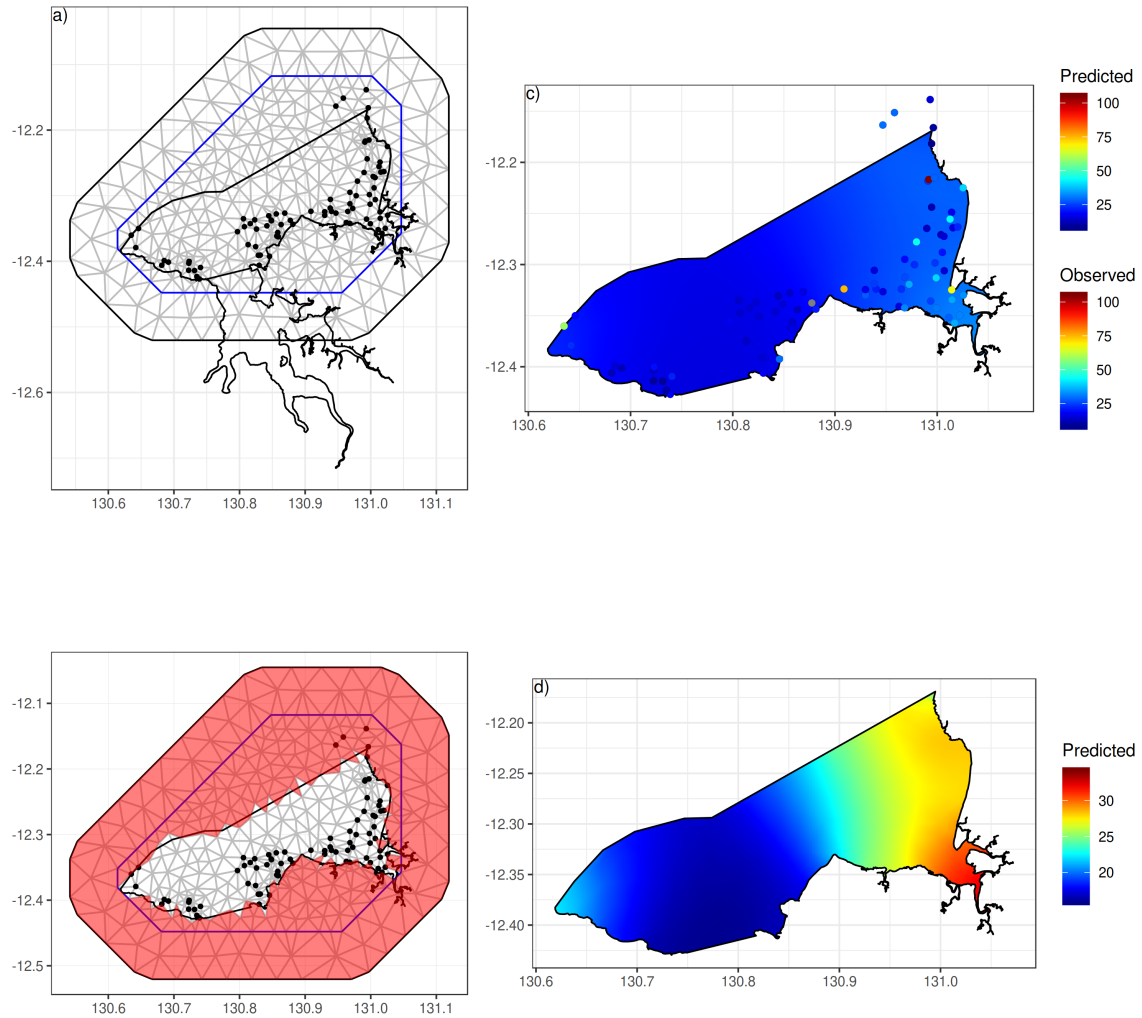


Figure 57: Integrated Nested Laplace Approximation (INLA) barrier spatial modelling of Arsenic. The diagram illustrates a) the mesh, b) the barrier mask, c) the resulting predicted 2D surface (and observed training data as points) and d) the resulting predicted 2D surface scaled to the range of predictions.

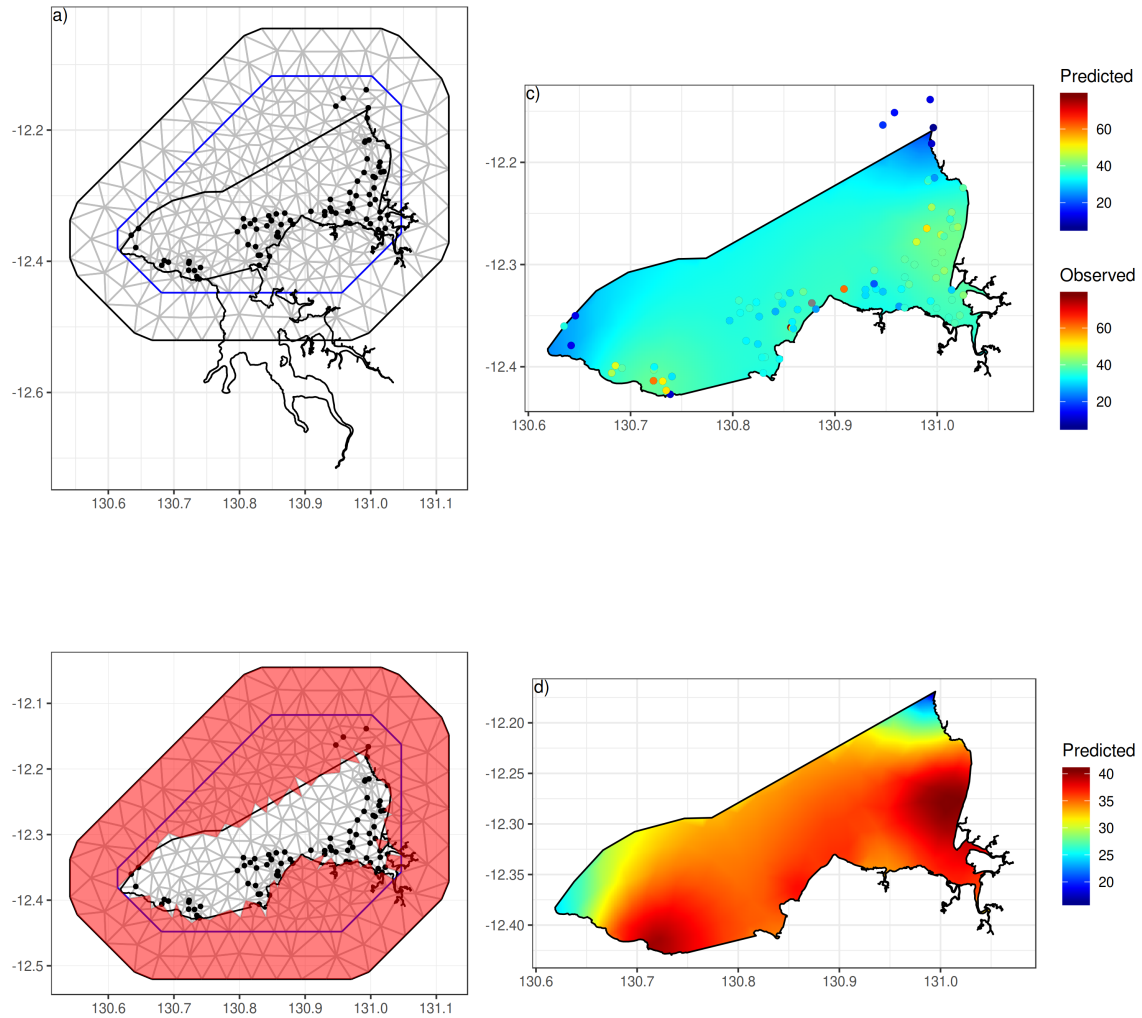


Figure 58: *Integrated Nested Laplace Approximation (INLA) barrier spatial modelling of Cerium. The diagram illustrates a) the mesh, b) the barrier mask, c) the resulting predicted 2D surface (and observed training data as points) and d) the resulting predicted 2D surface scaled to the range of predictions.*

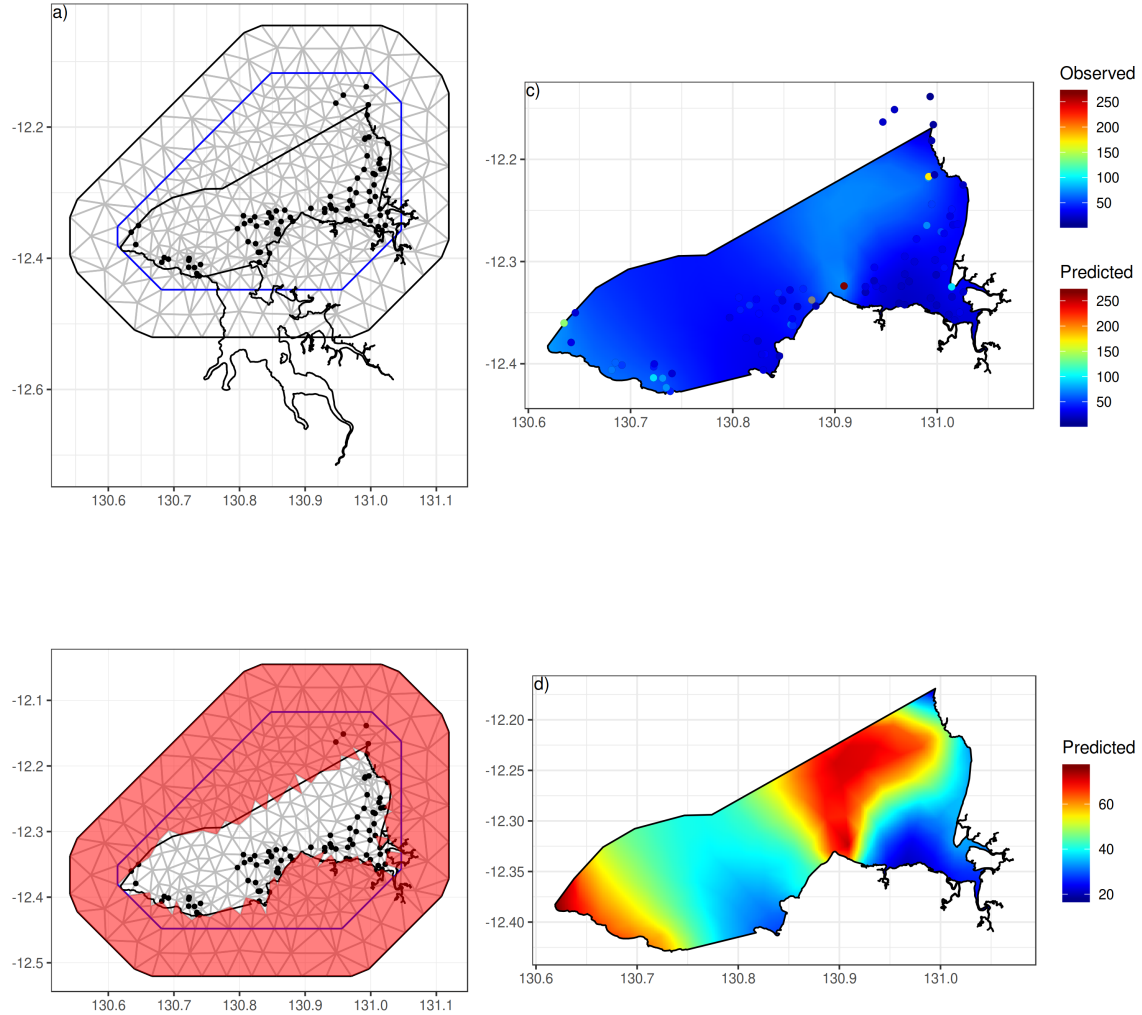


Figure 59: *Integrated Nested Laplace Approximation (INLA) barrier spatial modelling of Chromium. The diagram illustrates a) the mesh, b) the barrier mask, c) the resulting predicted 2D surface (and observed training data as points) and d) the resulting predicted 2D surface scaled to the range of predictions.*

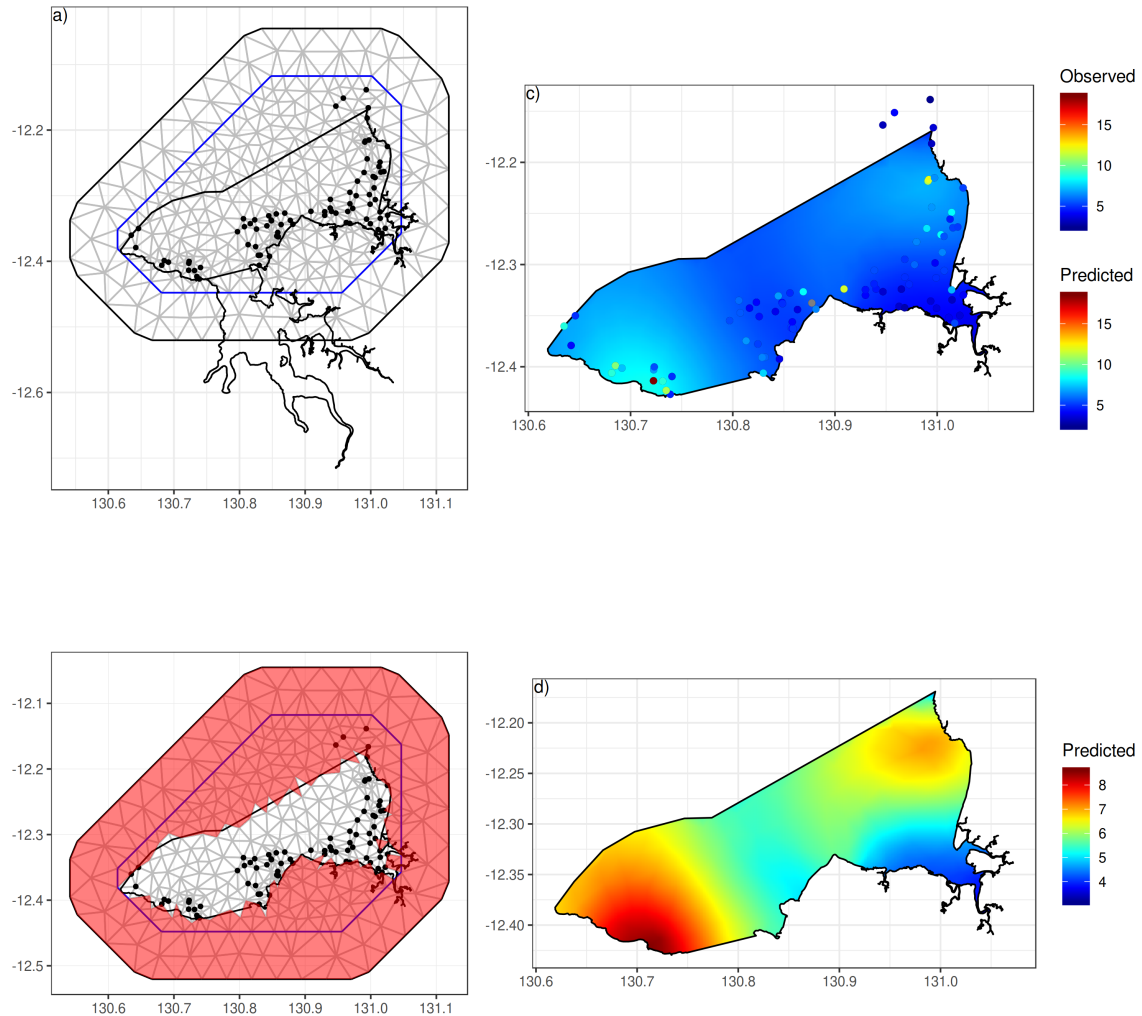


Figure 60: *Integrated Nested Laplace Approximation (INLA) barrier spatial modelling of Copper.* The diagram illustrates a) the mesh, b) the barrier mask, c) the resulting predicted 2D surface (and observed training data as points) and d) the resulting predicted 2D surface scaled to the range of predictions.

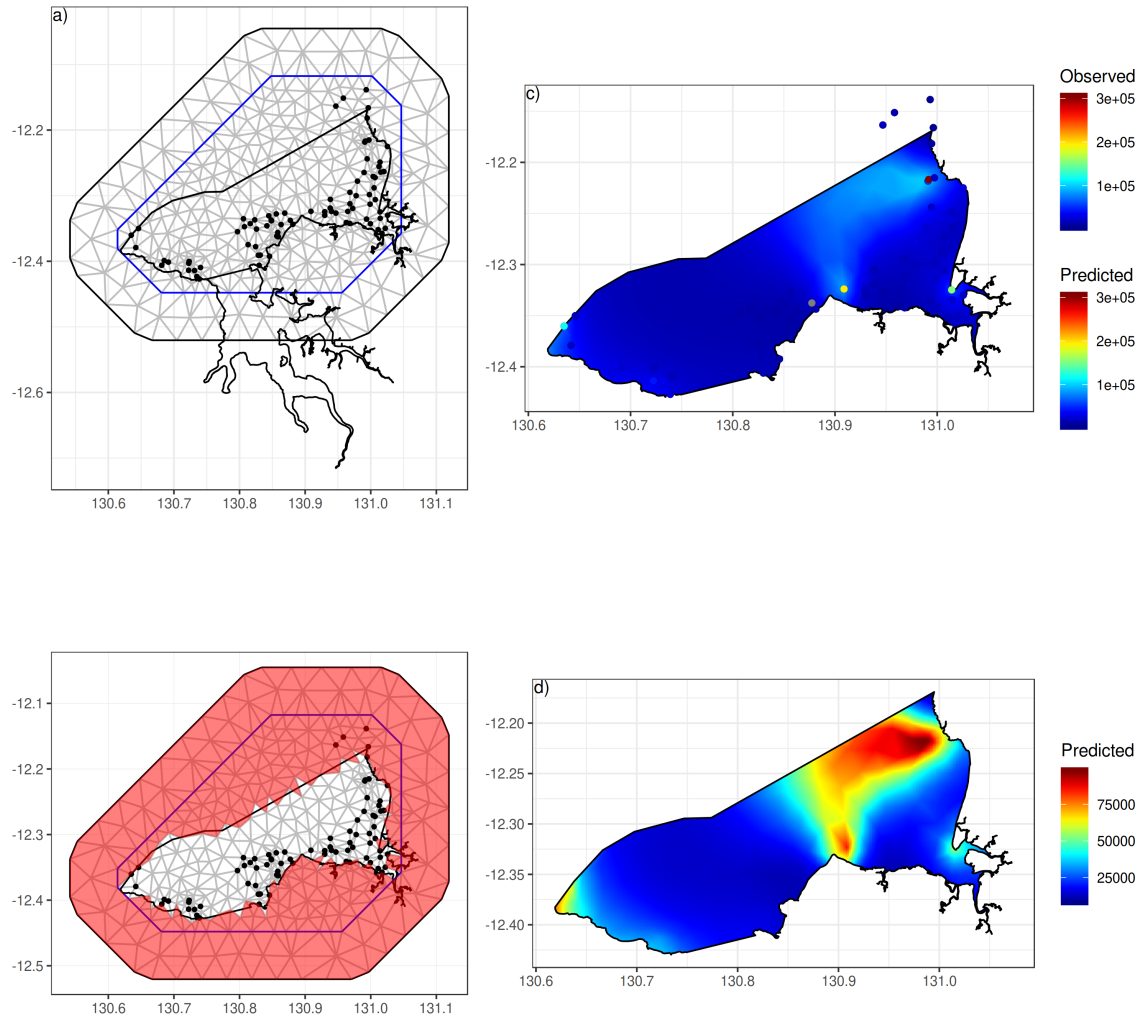


Figure 61: *Integrated Nested Laplace Approximation (INLA) barrier spatial modelling of Iron. The diagram illustrates a) the mesh, b) the barrier mask, c) the resulting predicted 2D surface (and observed training data as points) and d) the resulting predicted 2D surface scaled to the range of predictions.*

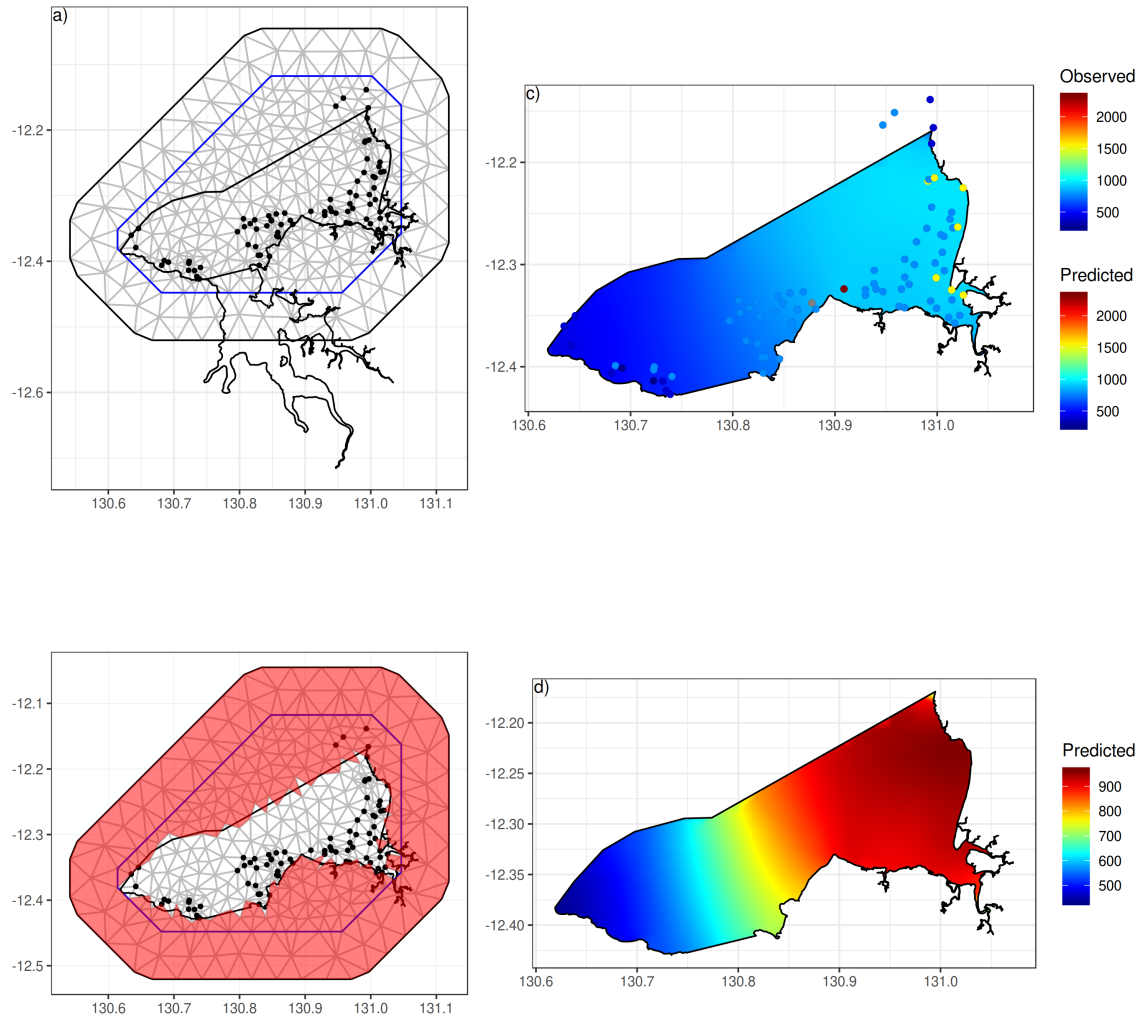


Figure 62: *Integrated Nested Laplace Approximation (INLA) barrier spatial modelling of Manganese.* The diagram illustrates a) the mesh, b) the barrier mask, c) the resulting predicted 2D surface (and observed training data as points) and d) the resulting predicted 2D surface scaled to the range of predictions.

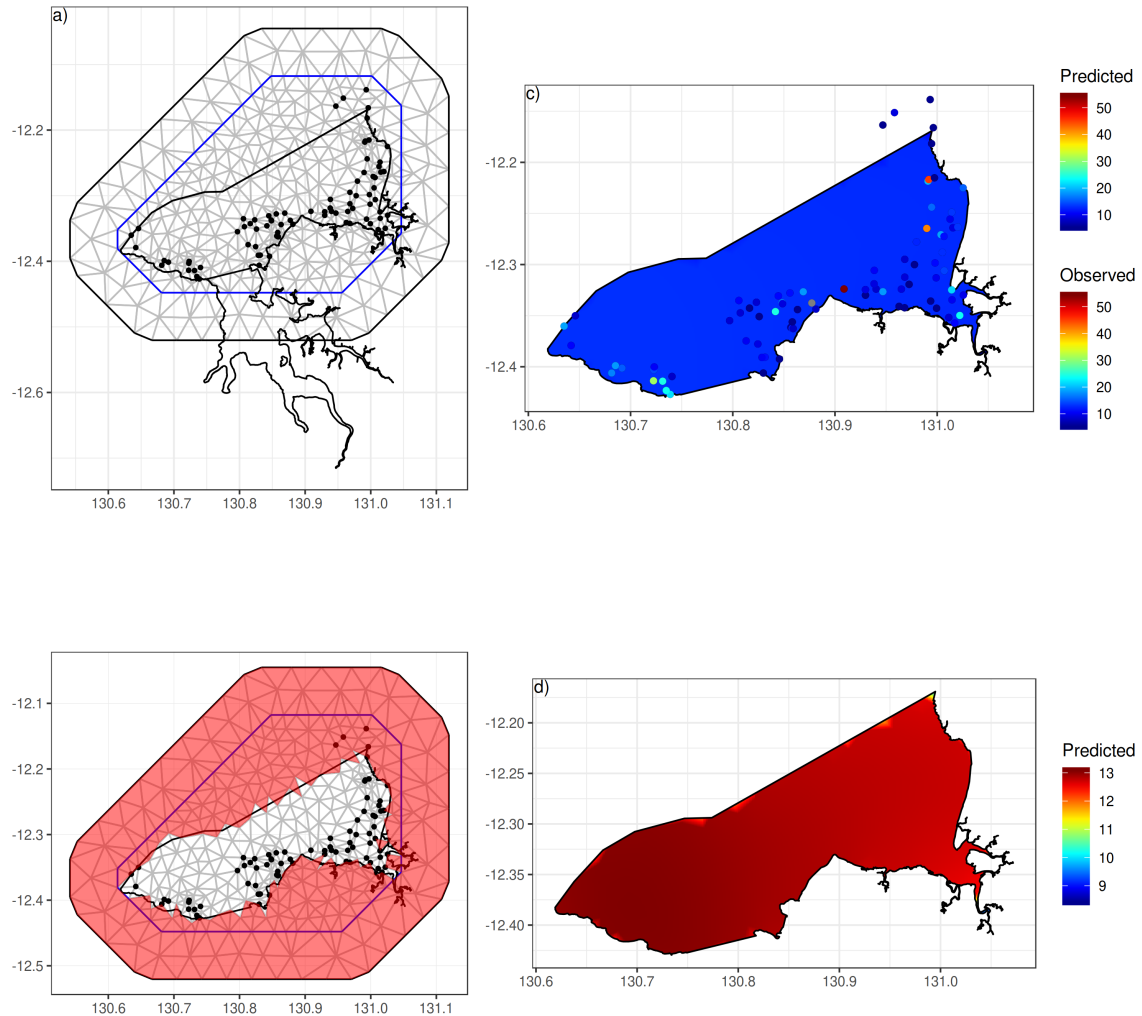


Figure 63: *Integrated Nested Laplace Approximation (INLA) barrier spatial modelling of Nickel. The diagram illustrates a) the mesh, b) the barrier mask, c) the resulting predicted 2D surface (and observed training data as points) and d) the resulting predicted 2D surface scaled to the range of predictions.*

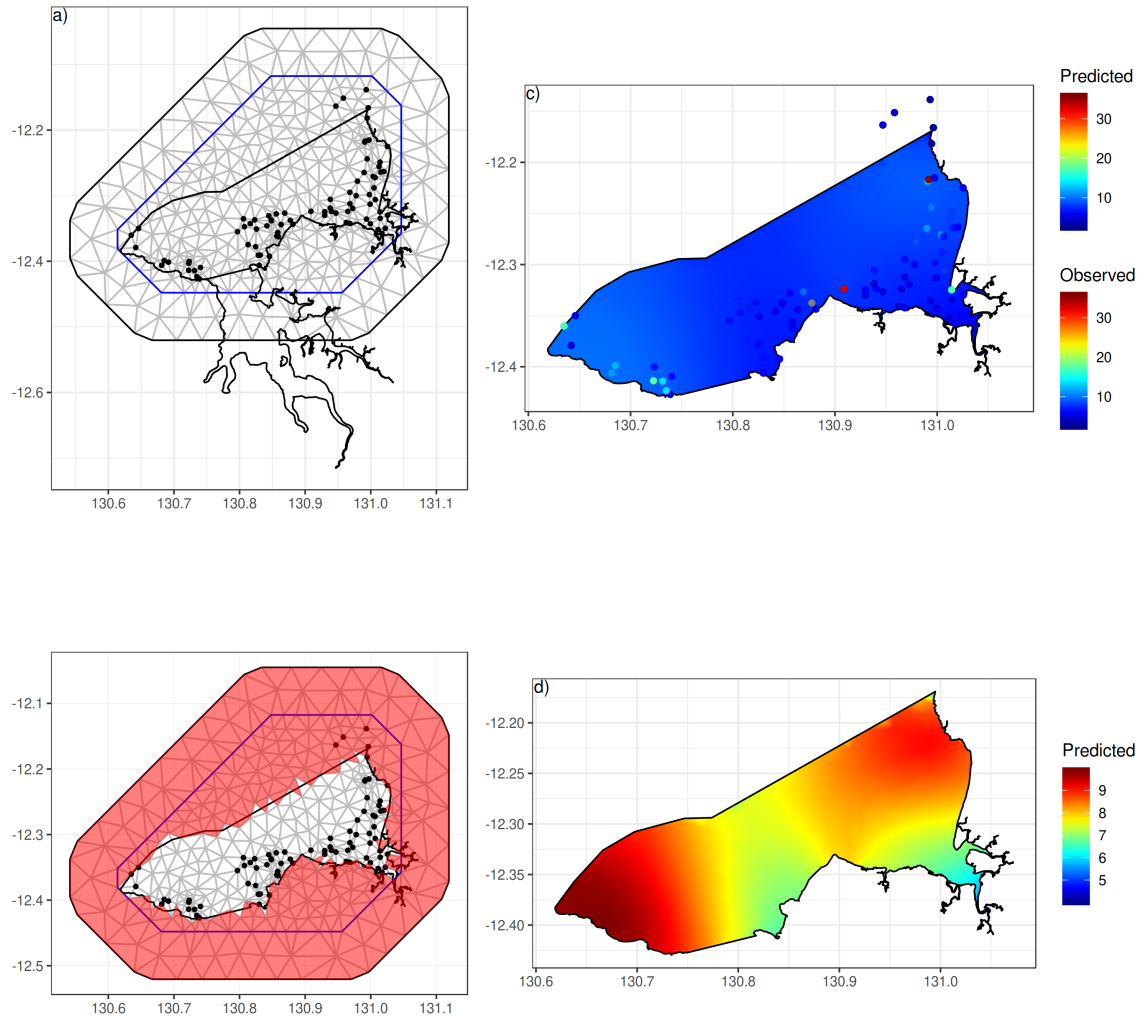


Figure 64: *Integrated Nested Laplace Approximation (INLA) barrier spatial modelling of Lead. The diagram illustrates a) the mesh, b) the barrier mask, c) the resulting predicted 2D surface (and observed training data as points) and d) the resulting predicted 2D surface scaled to the range of predictions.*

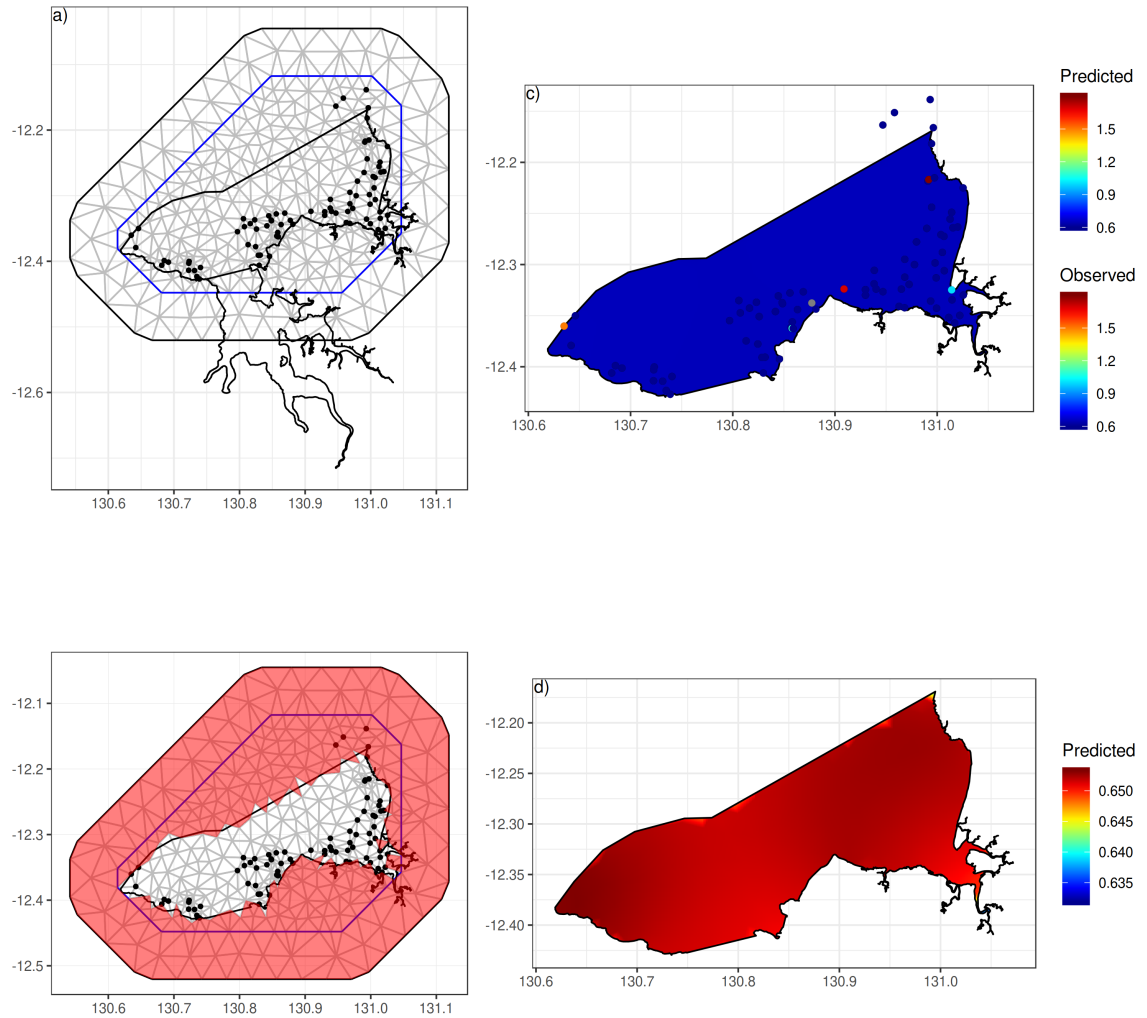


Figure 65: *Integrated Nested Laplace Approximation (INLA) barrier spatial modelling of Antonium. The diagram illustrates a) the mesh, b) the barrier mask, c) the resulting predicted 2D surface (and observed training data as points) and d) the resulting predicted 2D surface scaled to the range of predictions.*

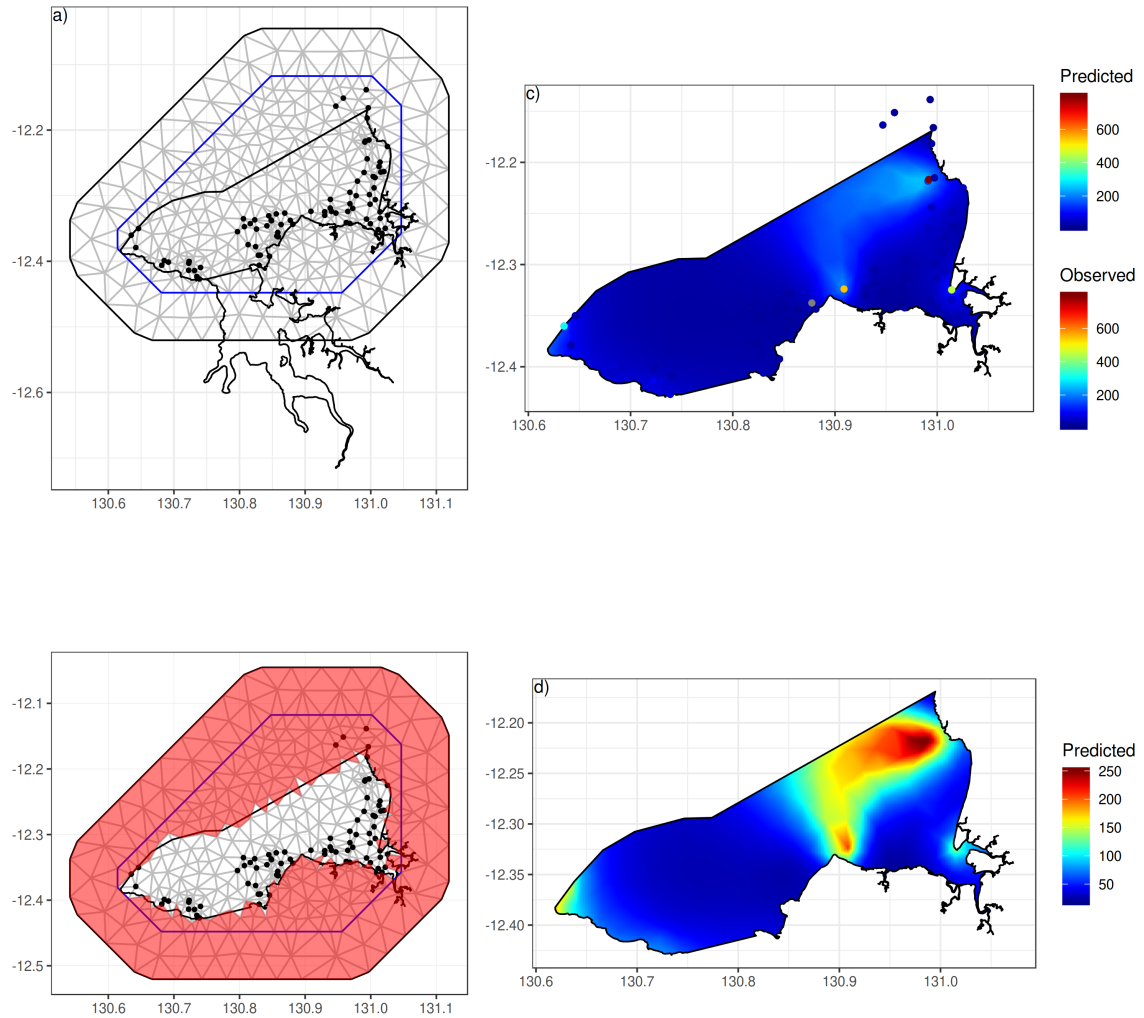


Figure 66: *Integrated Nested Laplace Approximation (INLA) barrier spatial modelling of Vanadium. The diagram illustrates a) the mesh, b) the barrier mask, c) the resulting predicted 2D surface (and observed training data as points) and d) the resulting predicted 2D surface scaled to the range of predictions.*

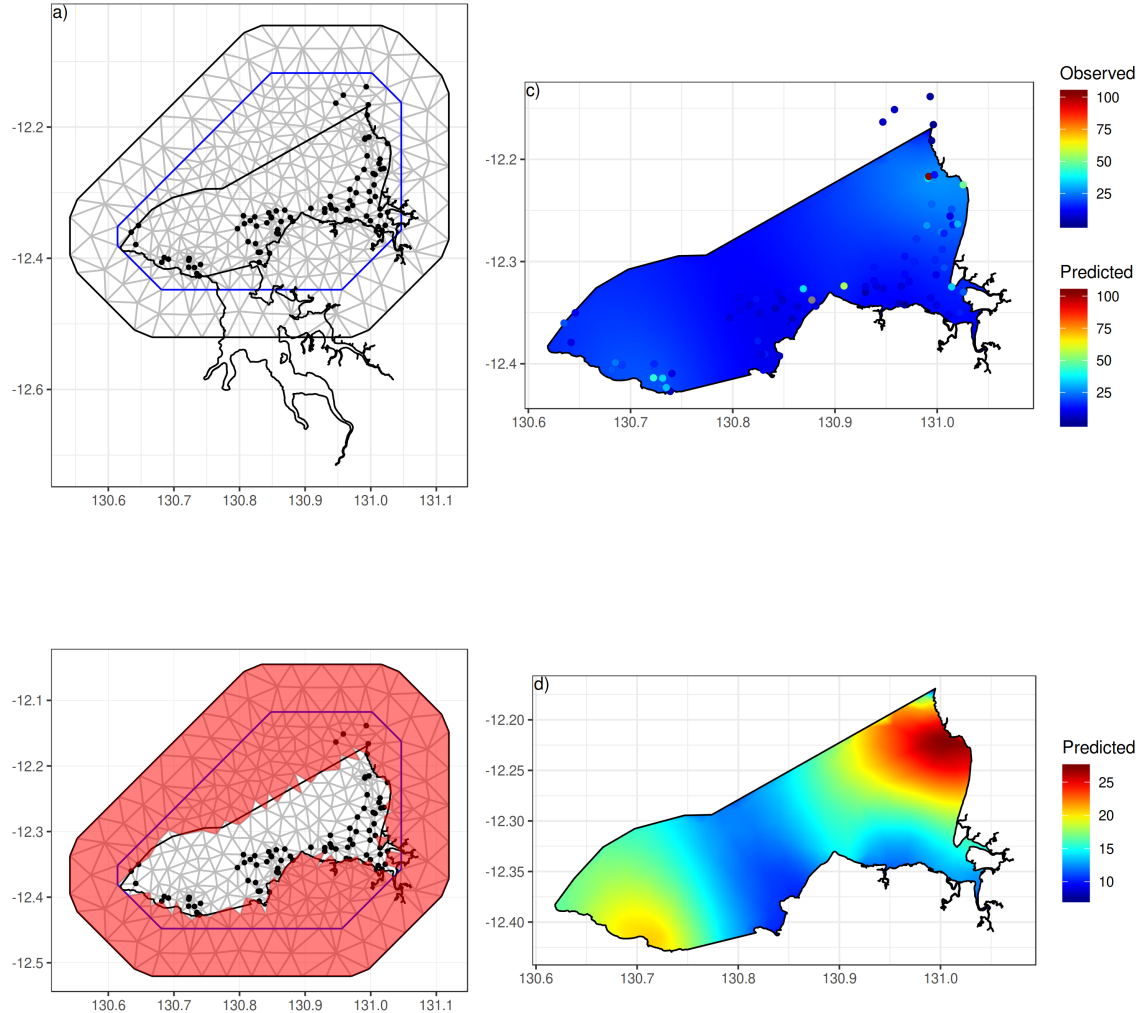


Figure 67: *Integrated Nested Laplace Approximation (INLA) barrier spatial modelling of Zn. The diagram illustrates a) the mesh, b) the barrier mask, c) the resulting predicted 2D surface (and observed training data as points) and d) the resulting predicted 2D surface scaled to the range of predictions.*

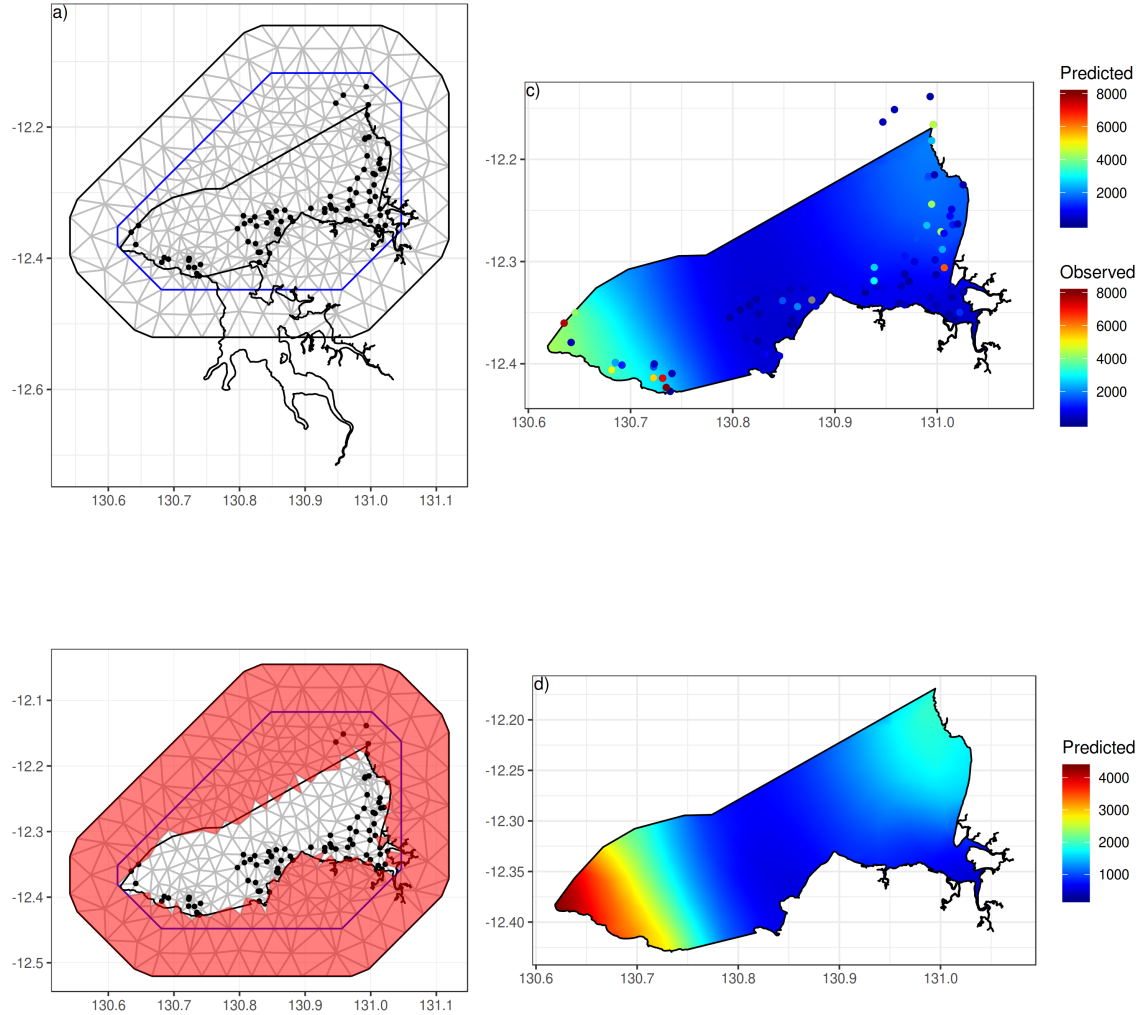


Figure 68: *Integrated Nested Laplace Approximation (INLA) barrier spatial modelling of Total organic Carbon. The diagram illustrates a) the mesh, b) the barrier mask, c) the resulting predicted 2D surface (and observed training data as points) and d) the resulting predicted 2D surface scaled to the range of predictions.*

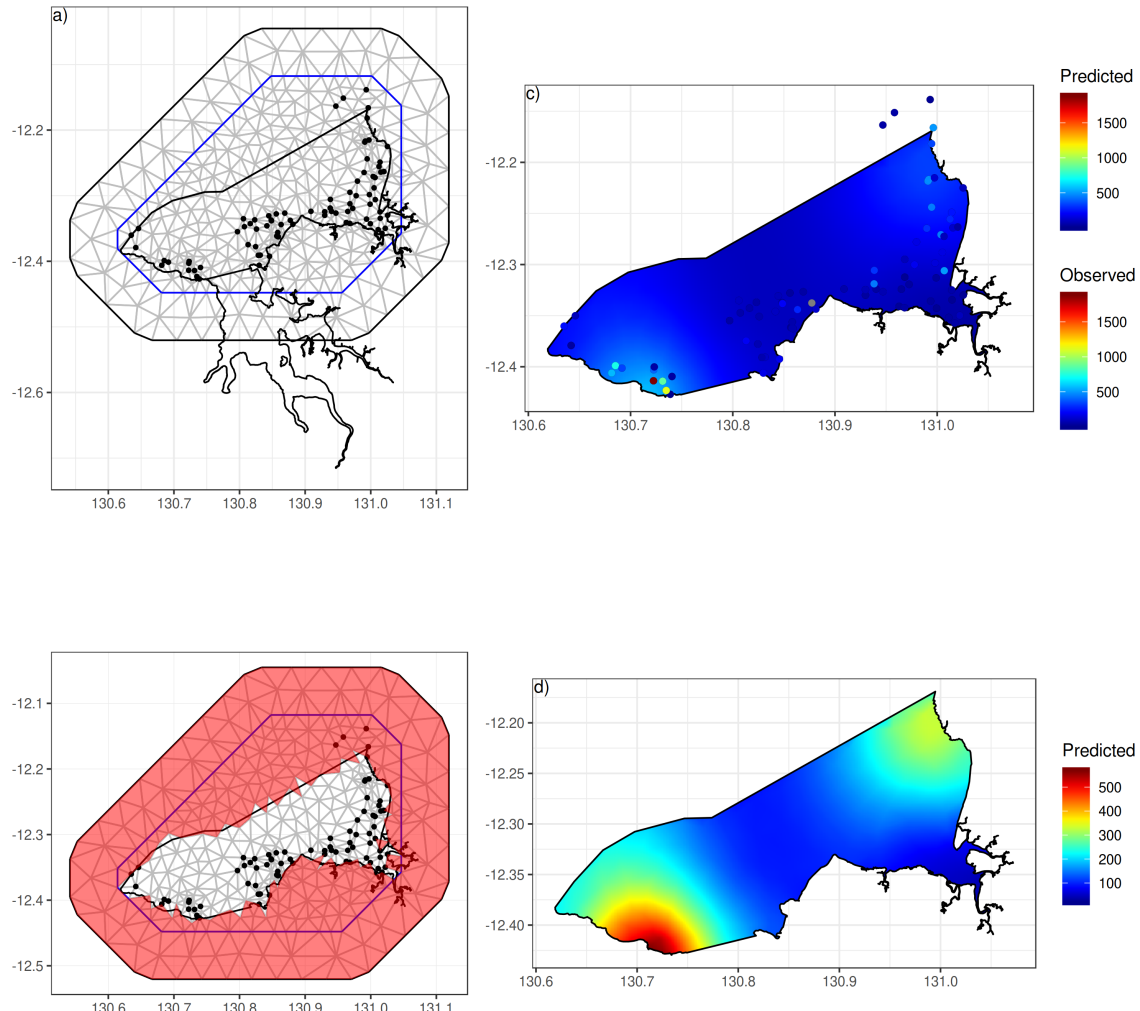


Figure 69: *Integrated Nested Laplace Approximation (INLA) barrier spatial modelling of Total Nitrogen. The diagram illustrates a) the mesh, b) the barrier mask, c) the resulting predicted 2D surface (and observed training data as points) and d) the resulting predicted 2D surface scaled to the range of predictions.*

This document was produced from markdown using knitr on R version 3.6.1 (2019-07-05) on a x86_64-pc-linux-gnu system.

```
> sessionInfo()
```

```
R version 3.6.1 (2019-07-05)
Platform: x86_64-pc-linux-gnu (64-bit)
Running under: Arch Linux

Matrix products: default
BLAS: /usr/lib/libopenblas-r0.3.7.so
LAPACK: /usr/lib/liblapack.so.3.8.0

locale:
[1] LC_CTYPE=en_AU.utf8          LC_NUMERIC=C                  LC_TIME=en_AU.UTF-8
```

```
[4] LC_COLLATE=en_AU.utf8      LC_MONETARY=en_AU.UTF-8    LC_MESSAGES=en_AU.utf8
[7] LC_PAPER=en_AU.UTF-8       LC_NAME=C                  LC_ADDRESS=C
[10] LC_TELEPHONE=C           LC_MEASUREMENT=en_AU.UTF-8 LC_IDENTIFICATION=C
```

attached base packages:

```
[1] stats      graphics   grDevices utils      datasets  methods   base
```

other attached packages:

```
[1] knitr_1.25
```

loaded via a namespace (and not attached):

```
[1] compiler_3.6.1 magrittr_1.5   tools_3.6.1     stringi_1.4.3  stringr_1.4.0  xfun_0.10
[7] evaluate_0.14
```

7. References

- Bakka, Haakon, Jarno Vanhatalo, Janine Illian, Daniel Simpson, and Håvard Rue. 2016. “Non-stationary Gaussian models with physical barriers.” *arXiv E-Prints*, August, arXiv:1608.03787. <http://arxiv.org/abs/1608.03787>.
- Grafström, Anton, Niklas L. P. Lundström, and Lina Schelin. 2012. “Spatially Balanced Sampling Through the Pivotal Method.” *Biometrics* 68 (2): 514–20. <https://doi.org/10.1111/j.1541-0420.2011.01699.x>.
- Minasny, B., and A. B. McBratney. 2006a. “A Conditioned Latin Hypercube Method for Sampling in the Presence of Ancillary Information.” *Computers & Geosciences* 32 (9): 1378–88. <https://doi.org/https://doi.org/10.1016/j.cageo.2005.12.009>.
- . 2006b. “Chapter 12 Latin Hypercube Sampling as a Tool for Digital Soil Mapping.” In *Digital Soil Mapping*, edited by P. Lagacherie, A. B. McBratney, and M. Voltz, 31:153–606. Developments in Soil Science. Elsevier. [https://doi.org/https://doi.org/10.1016/S0166-2481\(06\)31012-4](https://doi.org/https://doi.org/10.1016/S0166-2481(06)31012-4).
- Rue, H., S. Martino, and N. Chopin. 2009. “Approximate Bayesian Inference for Latent Gaussian Models Using Integrated Nested Laplace Approximations.” *Journal of the Royal Society of Statistics Series B - Statistical Methodology* 71 (2): 319–92.
- Siwabessy, P. J. W. 2019. “Seabed Mapping of Darwin Harbour Region (Including Bynoe Harbour): Hard Seabed Layer.” Geoscience Australia, Canberra, ACT, Australia.
- Thomsen, Laurenz. 2002. “The Benthic Boundary Layer.” In, 143–55. https://doi.org/10.1007/978-3-662-05127-6_9.